FEDERAL UNIVERSITY OF SANTA CATARINA (UFSC)
GRADUATE PROGRAM ON MATERIALS SCIENCE AND ENGINEERING (PGMAT)

Andre Luiz da Silva

Anatase-Rutile Phase Stability and Photocatalytic Activity of Nb_2O_5-doped TiO_2

Thesis presented to the Graduate Program in Materials Science and Engineering of the Federal University of Santa Catarina, as a requirement for obtaining the PhD degree in Materials Science and Engineering.

Advisor at UFSC
Dachamir Hotza

Supervisors abroad
Ricardo H. R. Castro/UC Davis, USA
Michele Dondi/ISTEC, Italy

Florianópolis

2016

Ficha de identificação da obra elaborada pelo autor,
através do Programa de Geração Automática da Biblioteca Universitária da UFSC.

Da Silva, Andre Luiz
Anatase-Rutile Phase Stability and Photocatalytic Activity of Nb2O5-doped TiO2 / Andre Luiz Da Silva ; orientador, Dachamir Hotza ; coorientador, Ricardo H.R. Castro, coorientador, Michele Dondi. - Florianópolis, SC, 2016.
163 p.

Tese (doutorado) - Universidade Federal de Santa Catarina, Centro Tecnológico. Programa de Pós-Graduação em Ciência e Engenharia de Materiais.

Inclui referências

1. Ciência e Engenharia de Materiais. 2. Titanium dioxide nanoparticles. 3. Niobium pentoxide doped titania. 4. Anatase-rutile phase stability . 5. Photocatalytic activity . I. Hotza, Dachamir . II. Castro, Ricardo H.R. . III. Universidade Federal de Santa Catarina. Programa de Pós-Graduação em Ciência e Engenharia de Materiais. IV. Título.

Andre Luiz da Silva

Anatase-Rutile Phase Stability and Photocatalytic Activity of Nb_2O_5-doped TiO_2

This thesis was presented to obtain the Title of PhD in Materials Science and Engineering and approved in its final version by the Graduate Program in Materials Science and Engineering (PGMAT) of the Federal University of Santa Catarina (UFSC).

Florianópolis, November 4, 2016.

_____
Prof. Guilherme Mariz de Oliveira Barra, Dr.
Coordinator

Examiners:

_____
Prof. Dr. Dachamir Hotza,
UFSC/Advisor

_____
Prof. Dr. João A. Labrincha,
Universidade de Aveiro/Portugal

_____
Prof. Dr. Douglas Gouvêa,
POLI/USP

_____
Prof. Dr. Adriano Bernardin,
UNESC

_____
Prof.ª Dr.ª Regina F. P. M. Moreira,
EQA/UFSC

_____
Prof. Dr. Fabiano Raupp Pereira,
PGMAT/UFSC

To my lovely wife Caroline Inacio Spilere!

Acknowledgements

First of all, I have to thank God for all blessings in my life, in special for these 4 last years of hard work during this journey to the conclusion of my PhD. Thanks for my health, thanks to give me the energy I needed to go through this incredible time of learning.

Special thanks to my wonderful lovely wife, Caroline, that made me see the world with different eyes. Thanks for being the one who pushed me up to start this journey and the one who supported me in the most difficult decisions. Thanks for being by my side all the time, sharing the experiences and supporting me when I needed.

I would like to thank Prof. Dachamir Hotza. I am so thankful to have known him. Nothing of this had happened the way it happened if he was not by me. Thanks for believing in me, in my capacity to overcome the challenges. Thanks for all knowledge and experiences shared with me, not just on science but also on culture.

I am very grateful to my supervisor at UC Davis, Prof. Ricardo Castro. I had a wonderful and remarkable experience in his Nanoceramics Thermochemistry Laboratory. Thanks for all support and knowledge shared with me. Thanks also for all people from his group, which for the 20 months that I had been there they became my friends and were always happy helping me even in new experiments or discussions. Dereck, John, Hasan, Sanchita, Ben, Longjia, Mingming, thank you guys. Thanks to Prof. Alexandra Navrotsky, for allowing the use of this unique laboratory at UC Davis.

Thanks to Prof. Michele Dondi and his group for hosting me in another great internship abroad at ISTEC, Italy.

This work was also possible thanks to the financial support from the Brazilian funding agencies CAPES and CNPq and to the Graduate Program on Materials Science and Engineering (PGMAT).

I also acknowledge all Professors that have taught me during my PhD.

Finally, I would like to thank my family, my parents Esmeraldina e José, my mother-in-law and father-in-law Marlete and Adair, which are proud of my achievements.

"The important thing is to not stop questioning. Curiosity has its own reason for existing."

(Albert Einstein)

RESUMO

Nanopartículas de dióxido de titânio são amplamente utilizadas como fotocatalisadores. A fração relativa do polimorfo de dióxido de titânio (anatásio, rutilo, ou bruquita), a dimensão das nanopartículas e a dopagem afetam significativamente o desempenho fotocatalítico desse material. Devido à menor energia de superfície, a fase anatásio é favorecida em escala nanométrica. Porém, elementos dopantes, tais como o nióbio, podem mudar esse comportamento devido a alterações tanto na superfície quanto no volume das nanopartículas. Contudo, o efeito do nióbio na estabilidade relativa das fases anatásio e rutilo ainda não é bem entendido do ponto de vista termodinâmico. Visando uma melhor compreensão desse efeito, na primeira parte desse trabalho, foi construído um novo diagrama de fases preditivo para TiO_2 dopado com Nb_2O_5, que mostra a estabilidade do polimorfo da titânia em função da composição e tamanho de grão. Na sequência, nanopartículas de TiO_2 dopadas com 0 a 5 mol% de Nb_2O_5 foram sintetizadas por precipitação simultânea. 5 mol% Nb_2O_5 postergou a transformação de anatásio para rutilo em aproximadamente 200 °C. Após tratamento térmico do TiO_2 dopado com 5 mol% Nb_2O_5 a 700 °C, não foi detectada a fase rutilo, enquanto TiO_2 não dopado apresentou 90 % dessa fase. Para amostras calcinadas a 450 °C por 7 h, uma diminuição no tamanho do cristalito de 11.8 para 5.9 nm e um aumento na área superficial específica de 92 para 168 m^2/g foram observados entre o TiO_2 não dopado e o TiO_2 dopado com 5 mol% de Nb_2O_5. A atividade fotocatalítica do anatásio foi medida pela taxa de decomposição do azul de metileno sob iluminação ultravioleta e luz visível e comparado com um catalisador comercial padrão (TiO_2 P25). Os resultados mostraram que o TiO_2 dopado com 5 mol% Nb_2O_5 apresentou atividade fotocatalítica superior àquela medida para o TiO_2 P25 sob luz visível. O desempenho aumentado foi atribuído à mudança da química de superfície associada com uma breve mudança na energia da banda proibida. Então, TiO_2 dopado com 5 mol% de Nb_2O_5 foi aplicado sobre revestimentos cerâmicos esmaltados por spray de modo a formar um filme nanométrico após sinterização entre 600-900 °C. O caráter super-hidrofílico foi avaliado pela medida do ângulo de contato da água sob irradiação UV. A degradação do azul de metileno foi realizada de acordo com ISO 10.678 e JIS R 1703-2. Os resultados mostraram um melhor desempenho das amostras dopadas em todas as temperaturas testadas. Em 800 °C, as amostras dopadas alcançaram ângulo de contato de água próximo de zero em apenas 15 min sob irradiação UV. As imagens de MEV mostraram que o dopante

Nb_2O_5 drasticamente diminui o tamanho do grão das nanopartículas de TiO_2.

Palavras-chave: pentóxido de nióbio, dióxido de titânio, energia de superfície, entalpia, anatásio, rutilo, estabilidade de fase, fotocatálise, revestimentos cerâmicos.

ABSTRACT

Titanium dioxide nanoparticles are widely used as photocatalysts. The relative fraction of titanium dioxide polymorph, i.e. anatase, rutile, or brookite, the nanoparticle size and the doping significantly affect the photocatalytic performance of this material. Due to the smaller surface energy, the anatase phase is more favorable at nanoscale. Doping elements, such as niobium, are expected to modify this behavior, due to changes in both surface and bulk energies. However, the effect of niobium on the relative stability of anatase and rutile phases is not well understood from the thermodynamic point of view. Aiming a better understanding of this effect, in the first part of this work, a new predictive nanoscale phase diagram was built for Nb_2O_5-doped TiO_2, which shows the stable titania polymorph as a function of the composition and size. In the sequence, TiO_2 nanoparticles doped with 0 to 5 mol% Nb_2O_5 were synthesized by simultaneous precipitation. 5 mol% Nb_2O_5 postponed the anatase to rutile transformation by about 200 °C. After thermal treatment of 5 mol% Nb_2O_5-doped TiO_2 at 700 °C, no rutile was detected, while undoped TiO_2 presented 90 wt.% of this phase. For samples calcined at 450 °C for 7 h, a decreasing on crystallite size from 11.8 to 5.9 nm and an increasing on specific surface area from 92 to 168 m^2/g were observed between the undoped TiO_2 and 5 mol% Nb_2O_5-doped TiO_2. Photocatalytic activity of anatase polymorph was measured by the decomposition rate of methylene blue under ultraviolet and daylight illumination and compared to commercial standard catalyst (TiO_2 P25). The results showed higher photocatalytic activity for 5 mol% Nb_2O_5-doped TiO_2 than P25 under visible light. The enhanced performance was attributed to surface chemistry change associated with a slight shift in the band gap. Thus, 5 mol% Nb_2O_5-doped TiO_2 was coated on glazed ceramic tiles by spraying to form a nanometric film on the surface of the ceramic tiles after sintering from 600-900 °C. The superhydrophilic character was evaluated by measuring the water contact angle under UV-irradiation. The degradation of methylene blue was performed according to ISO 10.678 and JIS R 1703-2. The results showed better performance of doped samples at all temperature tested (600-900 °C). At 800 °C, the doped samples achieved water contact angle near to zero in just 15 min under UV-irradiation. The SEM images showed that Nb_2O_5 doping drastically decreases the grain size of the TiO_2 nanoparticles.

Keywords: niobium pentoxide, titanium dioxide, surface energy, enthalpy, anatase, rutile, phase stability, photocatalysis, ceramic tiles.

LIST OF FIGURES

LIST OF TABLES

LIST OF ABBREVIATIONS

AFM	=	Atomic Force Microscopy
ART	=	Anatase-to-Rutile Transformation
ASTM	=	American Society for Testing and Materials
BET	=	Brunauer Emmett Teller
CB	=	Conduction Band
CE	=	Counter Electrode
DSC	=	Differential Scanning Calorimetry
DSSC	=	Dye Sensitized Solar Cell
EM	=	Electron Microscopy
HRTEM	=	High Resolution Transmission Electron Microscopy
ISO	=	International Organization for Standardization
JCPDS	=	Joint Committee on Powder Diffraction Standards
JIS	=	Japanese Industrial Standard
LPD	=	Liquid Phase Deposition
MB	=	Methylene Blue
MWCNTs	=	Multi-walled Carbon Nanotubes
NB	=	Niobium Butoxide
PC	=	Photocatalytic
PCE	=	Powder Conversion Efficiency
PVC	=	Polyvinyl Chloride
PVDF	=	Polyvinylidene Fluoride
RE	=	Rare-Earth
SEM	=	Scanning Electron Microscopy
TEM	=	Transmission Electron Microscopy
TG	=	Thermal Gravimetric Analysis
TTIP	=	Titanium (IV) Isopropoxide
UV	=	Ultra Violet
UVA	=	Ultra Violet A
UVB	=	Ultra Violet B
VB	=	Valence Band
WPF	=	Whole Pattern Fitting
XRD	=	X-ray Diffraction

LIST OF SYMBOLS

A	=	Area
d	=	Grain size
e^-	=	Electron
E	=	Intensity
E_a	=	Activation Energy
E_p	=	Photo UV-radiation intensity
G_{bulk}	=	Bulk free energy
G_{sys}	=	Total free energy
h^+	=	Hole
Lc	=	Load Scratching
p/p_0	=	Relative pressure
P_{MB}	=	Specific photoactivity
R	=	Decomposition activity index
R_{dark}	=	Specific degradation rate in the dark
R_{irr}	=	Specific degradation rate under UV irradiation
S	=	Entropy
γ	=	Surface energy
Γ_s	=	Solute Excess
$\Delta A\lambda$	=	Absorption difference from one measurement to another
ΔH_{ads}	=	Heat of adsorption
ΔH_{ds}	=	Enthalpy of drop solution
ΔH_{seg}	=	Enthalpy of segregation
ε	=	MB molar extinction coefficient at 664 nm
ζ_{MB}	=	Photonic efficiency
θ	=	Surface Coverage
θ_c	=	Monolayer coverage of dissociative water
θ_p	=	Physisorption monolayer coverage
ρ	=	Density

TABLE OF CONTENTS

1 INTRODUCTION

Titanium dioxide is widely used in the materials science field. The main applications are cosmetics, sunscreens, food coloring, toothpastes, polymers, paints and photocatalysis [1]. Since 1972, when Fujishima and Honda published an important paper about TiO_2 photocatalyst [2], the scientific community has exhaustively studied this subject. The interest on TiO_2 as a photocatalytic material is mainly attributed to the low production costs, high chemical stability, no toxicity and high photoactivity [3]. An electron-hole pair is generated when a TiO_2 photocatalyst site absorbs a photon with energy equal to or greater than its band-gap. Then, the pair is split into a free electron and a free hole, which helps the reduction and oxidation of species adsorbed at the semiconductor and induces oxidative degradation of species in solution through radical reactions [4].

Nowadays, nanotechnology has introduced interesting properties on materials that are not commonly seen in bulk samples. These properties are attributed to the fact that a large fraction of the atoms are within the interface region. Considering that this region represents around 0.5 nm thick shell, a particle with 15 nm will have roughly 20% of the atoms within the interface volume, which will increase even more for smaller particles [5]. Thus, in order to properly study this fascinating nanoscale world the knowledge of the surfaces phenomena is very important. A good example of the unprecedented characteristics of nanomaterials is the phase stability of TiO_2. The most common TiO_2 polymorphs are anatase and rutile phases. Rutile is known as the stable phase, while anatase as metastable. However, thermodynamic studies have shown that at nanoscale, anatase is actually more stable than rutile. This leads to a crossover at a specific surface area or crystallite size where rutile becomes the most thermodynamic stable one and the phase transition happens [6, 7].

In practice, anatase becomes rutile by thermal treatment at temperatures in the range 400-1200 °C. The earlier or later phase transition will happen depending on some parameters, e.g. particle size or shape, surface area, atmosphere, heating rate and impurities. Thus, depending on the phase desired, it will be necessary to play in favor or against the phase transition according to the temperature.

One of the most common ways to promote or inhibit the ART is the use of dopants. Several dopants have been mentioned in the

literature; some of them not only postpone the phase transformation but also can improve some TiO_2 properties, e.g. photocatalytic activity. Niobium has been a promising candidate to postpone the ART and at the same time to enhance the catalysis of titania. Thus, in this work Nb_2O_5 was chosen as dopant in TiO_2, in order to produce nanoparticles, which can be used in a thermodynamic study to better understand the role of the doping on the phase stability and to enhance practical applications as photocatalysts.

1.1 AIM

1.1.1 General Objective

The aim of this thesis is to study the anatase-rutile phase stability of Nb_2O_5-doped TiO_2 by the thermodynamic point of view, as well as to determine the amount of Nb_2O_5 doping that provides higher photocatalytic activity to be applied in glazed ceramic tiles.

1.1.2 Specific Objectives

The specific objectives of this thesis are listed below:

- To perform a systematic thermodynamic study on variable amounts of Nb_2O_5 doping in TiO_2.
- To obtain surface energies and enthalpies of drop solution of pure TiO_2 and Nb_2O_5-doped TiO_2 in order to make a predictive anatase-rutile phase transition diagram at nanoscale.
- To study the anatase to rutile phase transition as a function of temperature.
- To analyze the influence of doping concentration for powders calcined at same temperature (0-5 mol% Nb_2O_5-doped TiO_2) on crystallite size and specific surface area.
- To perform comparative studies of photocatalytic activity by degradation of methylene blue for TiO_2 and Nb_2O_5-doped powders on UV and visible light.
- To manufacture ceramic tiles coated with Nb_2O_5-doped TiO_2 and pure TiO_2 and characterize them according to photocatalytic and superhydrophilic characters.

1.2 Thesis structure

This thesis is divided into 7 chapters, as described below:

- Chapter 1 provides a general introduction to the subject discussed in this thesis, the aim and the specific objectives.
- Chapter 2 is a literature review focusing on titanium dioxide. It includes extraction and production, general applications, as well as photocatalysis and superhydrophilic properties. The crystallite phases are also discussed, with special regard to anatase to rutile transition.
- A literature review on photocatalytic ceramic tiles was made in Chapter 3. The deposition methods and adhesion behavior of TiO_2 on the substrate are discussed. The effects of deposition on tiles surface properties, as color, brightness, cleanability and roughness is presented, as well as the photocatalytic activity.
- Chapter 4 corresponds to the primary materials and methods used throughout this work. Details on each technique used are provided in the respective chapters.
- Chapter 5 is a systematic thermodynamic study to build a predictive anatase-rutile phase transition diagram at the nanoscale. TiO_2 and Nb_2O_5-doped TiO_2 were synthesized by simultaneous precipitation. After calcinations, pure anatase and rutile were obtained up to 2 mol% of Nb_2O_5-doping. The surface energies and enthalpies of drop solution were obtained using water adsorption and high temperature oxide melt solution calorimetry.
- In Chapter 6, the photocatalytic activity of the nanoparticles was evaluated by degradation of methylene blue solution. The photoactivity was measured under UV and visible light using the same surface area and weight concentration, comparing the results with P25. The anatase to rutile phase transition was also evaluated as a function of temperature and Nb concentration. The band

gap measurements and TEM images complete this chapter.

- In Chapter 7 Nb_2O_5-doped TiO_2 was synthesized by sol gel. The optimized sol was applied on ceramic tiles by spraying and treated thermally from 600-900 °C. The photocatalytic activity was evaluated by degradation of methylene blue. The evaluation of superhydrophilicity was measured by the water contact angle under UV-light. XRD and SEM images complete this chapter.

2 BACKGROUND

2.1 Titanium dioxide

2.1.1 Extraction and production

Titanium is a chemical element with atomic number 22 and atomic mass 47.87 u. It has a low density and it is a strong, lustrous, corrosion-resistant transition metal with a silver color. It was discovered in Cornwall, England, by William Gregor in 1791. Even though the element occurs in a number of mineral deposits, the main ones used to extract it are ilmenite and rutile, which are extensively distributed in the earth's crust and lithosphere [8].

The natural occurrence of the mineral titanium is TiO_2 (titanium dioxide), which is extracted from the earth and then further processed and purified. The two main routes to make its extraction are sulfate and chloride process. The first one uses the mineral ilmenite, which contains 40-60% TiO_2 and the second one uses the mineral rutile, which contains up to 90-95% TiO_2 [9].

Currently, about 60% of the TiO_2 worldwide production is generated by the chlorine process. However, some efforts have been done to improve the sulfate process. Nano-TiO_2 has been produced via sulfate process and parameters such as H_2SO_4 molar volume, reaction time; initial preheating temperature and H_2SO_4 concentration have been studied. The decomposition rate of ilmenite increases with the intensification of H_2SO_4 molar volume from 0.28 mol to 0.32 mol. The optimal reaction time to provide the maximum ore decomposition was found at 120 min, while the H_2SO_4 concentration was 13.5 mol/L [10].

2.1.2 Applications

Due to the high reflectivity of rutile and anatase, the primary application of TiO_2 is food coloring, cosmetics, sunscreens, toothpastes, polymers, paints, and any other products in which white pigmentation is wanted [1]. TiO_2 has been used in façades paints as one of the most efficient white pigments due to its high refractive index and chemical inertness. It is also widely used in waterborne paints, thanks to its compatibility with aqueous dispersions [11]. However, the use of TiO_2 in paints has some limitations. The polymeric binders used in paints to fix the pigment, when in contact

with titania, may be oxidized when exposed to sunlight. This effect is known as chalking, which is a non-adherent white powdery substance formed on the surface, similar to the chalk on the blackboard [1, 4].

Many products that are consumed in daily life use TiO_2 in their composition in order to improve the whiteness. The foods with the highest content of TiO_2 include candies, sweets, and chewing gums, placing the children as the main consumers. A child consumes 2-4 times more TiO_2 per kg_{bw} then an adult. Even though the TiO_2 nanomaterials used in foods are discharged as feces or urine, little is known about the effects of these nanoparticles in the human body. Some studies report a possible link of nano-TiO_2 to asthma, inflammation and Crohn's disease from gastrointestinal intake. However a risk assessment has not been published yet, care has to be taken when comparing exposure to effect [12].

The main use of TiO_2 in cosmetics is sunscreens. The intrinsic ability to filter ultraviolet (UVA/UVB) wavelength spectra provides a broader protection than any other sunscreening agent. In the past the sunscreens based on TiO_2 and ZnO let an opaque layer on the skin resulting in reluctance of consumers to use the products. This visual effect has been addressed by decreasing the particle size of these metal oxides to nanoscale. However, there are some concerns about the use of TiO_2 and ZnO nanoparticles in sunscreens. The first is about the photocatalytic properties, which can produce reactive oxygen species. Nevertheless, the manufacturers of nanoparticles containing sunscreens attempt to block the potential production of the reactive oxygen species by coating the nanoparticles or adding anti-oxidant compounds to the sunscreen formulation. Another concern is about the penetration of the sunscreen in the skin. Many researches have been made on this topic and the great majority of these studies indicated an apparent inability of TiO_2 and ZnO nanoparticles to reach viable cells in the dermis [13, 14].

In the energy field, titanium dioxide is one of the most recently investigated solar cell material, especially for dye sensitized solar cells (DSSCs). When sensitized with organic dyes or inorganic narrow band gap semiconductors, TiO_2 can absorb light into the visible light region and convert solar energy into electrical energy [15].

Due to the rapid growth of population and extensive usage of newly developed electricity-consuming devices, the energy consumption throughout the world is predicted to be increased at the

rate of 1.5% per annum from 2010 to 2040, and it is estimated that 30 TW of energy will be needed globally by the year 2050. Thus, this area has received special attention in the last years.

Even though the solar cell technology nowadays (~80-90%) is dominated by silicon-based material, TiO_2, ZnO and SnO_2 are widely used as photo-electrodes in the DSSCs. They have gained extensive attention because of their low production cost, ease of fabrication and tunable optical properties, such as color and transparency [16]. DSSCs are generally composed of a photoanode (dye-sensitized TiO_2 film), a counter electrode (CE), and an electrolyte containing a redox couple (iodide/triiodide). Fabrication of a qualified mesoporous TiO_2 film is crucial because the photoanode determines the power conversion efficiency (PCE) of the device to a large extent [17].

Among those widespread TiO_2 applications, photocatalytic activity is one of the most studied topic discussed in the literature nowadays. Titania is largely used in a variety of applications and products in the environmental and energy fields, including self-cleaning surfaces, air and water purification systems, sterilization, hydrogen evolution, and photoelectrochemical conversion [18].

2.1.2.1 Photocatalytic activity of TiO_2

For many years TiO_2 has been studied on the photocatalysis field due to its distinguished properties under UV light irradiation. According to Fujishima *et al.* [4], the first paper reported in the scientific literature about this TiO_2 behavior was in 1921. In that work, the authors proposed that titania was partially reduced during illumination with sunlight in the presence of an organic compound such as glycerol. Along the years, many reports have been made, with another important milestone in 1972, the Fujishima and Honda Nature paper [2], which has been cited thousands of times with an exponential increase after 2000. Coincidently, it was the same year in which the term superhydrophilicity appeared for the first time in the technical literature, in four papers published by three different research groups from Japan [19].

Currently, considerable attention is given to the development of photocatalysis. A variety of products across a broad range of research areas, including especially environmental and energy-related fields have used photocatalysis in their development. Fig. 1 shows the main applications of TiO_2 on photocatalysis field, which

are mostly related to the environment, as well as energy, such as solar cell and hydrogen based devices [18]. These applications do not depend only on the properties of the TiO_2 material itself, but also on the adjustments of the TiO_2 material host (e.g., inorganic and organic dyes) and on the interactions of TiO_2 materials with the environment [3].

Titanium dioxide is one of the photocatalytic materials most studied in the scientific community. Its availability associated with low production costs, high chemical stability, no toxicity and high photoactivity makes it an ideal photocatalyst. Furthermore, photogenerated electrons are reducing enough to produce superoxide from dioxygen [3, 20].

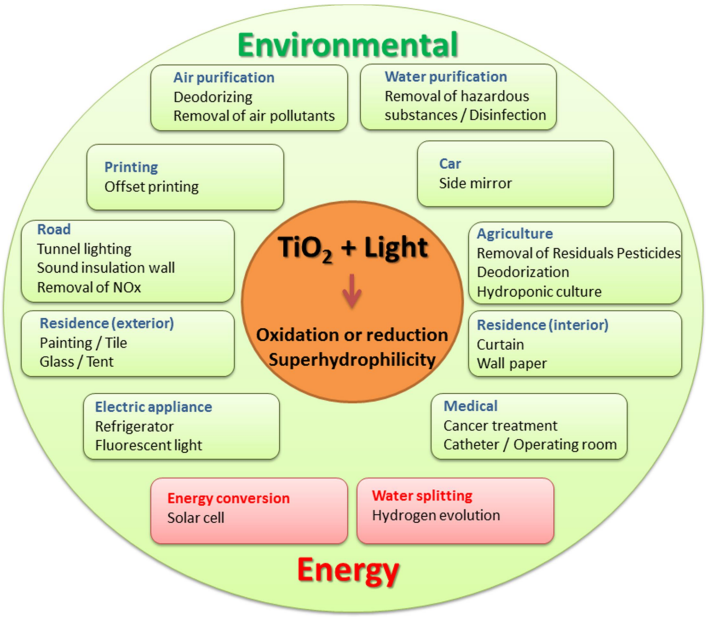

Figure 1. Applications of TiO_2 photocatalysis. (adapted from Nakata, 2012 [18]).

The TiO_2 photocatalytic properties are originated from the formation of photogenerated charge carries (holes and electrons), which occurs upon the absorption of ultraviolet (UV) light corresponding to the band gap [18]. Fig. 2 shows a schematic illustration of the formation of photogenerated charge carriers upon absorption of ultraviolet (UV) light. Two reactions occur

simultaneously: the first involving oxidation from photogenerated holes, and the second involving reduction from photogenerated electrons. Both processes must be balanced precisely for the photocatalyst itself do not undergo change, which is, after all, one of the basic requirements for a catalyst [4, 21].

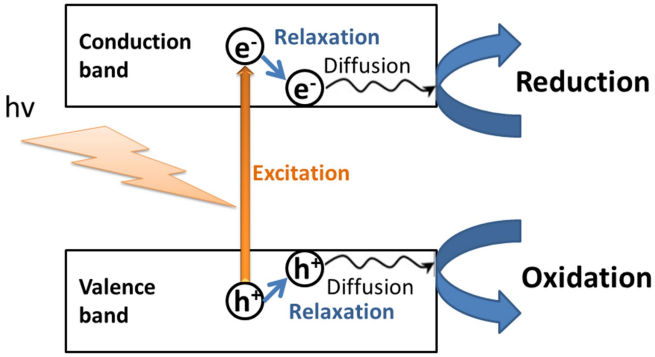

Figure 2. Schematic illustration of the formation of photogenerated charge carriers (hole and electron) upon absorption of ultraviolet (UV) light (adapted from Nakata, 2012 [18]).

The tendency of recombination of the generated positive and negative charge carriers by UV radiation are competing phenomena [20]. In comparison with other semiconductors, titanium dioxide has a relatively slow rate of charge carrier recombination. This places TiO_2 in advantage, since a photo-generated electron-hole pair needs a lifetime of at least 0.1 ns for chemical reactions to be facilitated [22]. If recombination occurs too fast, then there is no time for any other chemistry occurs, and photocatalytic activity is not observed. As titania has a relatively long live, around 250 nanoseconds, it allows the electron or hole to travel to the crystallite surface [23].

Titanium dioxide has three main polymorphs: rutile, anatase and brookite. Even though anatase has a larger band gap (~3.2 eV) if compared to rutile (~3.0 eV) [24, 25], the photocatalytic performance of anatase generally is considered superior than rutile. The first parameter that contributes to the improved performance is the high surface area, as the size of TiO_2 particles decreases, the fraction of atoms located at the surface increases. This leads to a high density of localized states, which involve electrons with energies between the conduction band and valence band and consequent surface-adsorbed hydroxyl radicals. Another important

aspect is the slow charge carrier recombination for anatase phase, which is essential for a good photocatalytic performance [26]. In addition, Sclafani and Herrmann [27] have shown by photoconductance measurements that rutile is less efficient in creating electron-hole pairs able to be followed by photosorption of oxygen. In parallel, after completion of photodesorption, rutile was less efficient in photoadsorbing oxygen. By contrast, anatase was able to substantially ionosorb oxygen, in the form of both O^- and O_2^- species. The O^- adsorbed species are principally involved in gas phase mild oxidation reactions, whereas O_2^- species are involved in electron capture in aqueous phase reactions to let photoholes react with surface OH^- groups.

Regarding to the grain size of titania, smaller grain sizes present a better performance related to the photocatalytic activity [28]. However, if the grain is too small, for some particular cases the activity is actually decreased. Wang *et al.* [29, 30] have studied the degradation of chloroform by TiO_2 with different grain sizes. According to their study, 11 nm TiO_2 presented higher activity than 6 nm and 20 nm. When the particle size becomes extremely small, due to the surface defect in semiconductors, surface recombination becomes an important process. In the regime of ultrafine particle size, most of the e^-/h^+ pairs are generated sufficiently close to the surface. They may quickly reach the surface, and undergo rapid surface recombination mainly due to the abundant surface trapping sites and the lack of driving force for e^-/h^+ pair separation. Since the characteristic time for surface e^-/h^+ recombination is much faster than that of the interfacial charge carrier transfer processes, the increase in the interfacial transfer rate will be outweighed by the increased surface recombination rate in ultrafine particles beyond a certain size reduction

2.1.2.2 Photocatalytic performance of TiO_2

The photocatalytic activity of TiO_2 has received special attention in the last years in order to improve its performance under UV and visible light. TiO_2 band gap is 3.2 eV for anatase and 3.0 eV for rutile, this means that just wavelengths shorter than ~400 nm can excite pairs of electrons and holes. Considering the whole sunlight spectrum, just 5% has sufficient energy to cause effective photosensitization [31]. Besides, energy loss due to light reflection,

transmission and energy loss as heat is inevitable in the photoprocess [32, 33].

The major practices to enhance the TiO_2 photoexcitation both under UV and visible light involve catalyst modification by doping, metal coating, surface sensitization, surface area increasing and development of secondary titania photocatalyst [33]. Among these practices, one of the most common is the use of doping into the TiO_2 lattice. Specific doping can even postpone the anatase-to-rutile phase transition regarding to temperature, as simultaneously changes the physical-chemistry of the surface of TiO_2, which can increase the photocatalytic performance. The main doping used are rare-earth (RE) [34-36], transition metals [37] and non-metals [38].

Among various RE doping, it can be cited Er^{3+} and Yb^{3+}. They have been used and improvements on the photocatalytic activity under visible light have been observed. The primary mechanism for the visible light sensitization is attributed to the availability of higher adsorption sites, increase of the BET surface area, decrease of the crystallite size and prevention of electron-hole recombination [35]. The formation of an excitation energy level below the conduction band of TiO_2 from the binding of electrons and oxygen vacancies decreases the excitation energy of RE doped TiO_2, resulting in highly active photocatalysts [35, 39]. Liang *et al.* [36] have studied the degradation of orange I by RE ions (Sm^{3+}, Nd^{3+}, Pr^{3+}) doped TiO_2. They found the highest photoactivity at 1.5% RE^{3+} dosage under UV light irradiation, and 1.0% RE^{3+} under visible light. The transitions of 4f electrons of RE^{3+} led to the enforcement of the optical adsorption of catalysts and favored the separation of photo-generated electron-hole pairs. Additionally, the red shift of the optical adsorption edge of TiO_2 by rare earth ion doping was helpful to the improvement of visible light photocatalytic activity of TiO_2. Hence, the transitions of 4f electrons of RE^{3+} and red shifts of the optical adsorption edge of TiO_2 by rare earth ion doping and dye sensitization enhanced visible light photocatalytic activity of TiO_2 [36].

Another set of doping is the metal doping, which has been widely used in order to improve the photocatalytic performance on the degradation of various organic pollutants under UV and visible light [3]. The performance of these materials does not depend just on the materials itself, but also on the organic pollutants, synthesis method, doping concentration and experimental procedure. Therefore, it is difficult to make unified conclusions. Choi *et al.* [40] have made a

systematic study with 21 metal ions on the oxidation of $CHCl_3$ and reduction of CCl_4. They found that the photocatalytic activity was related to the electron configuration of the dopant ion. In those dopant ions with closed electron shells, little or no effect on the activity was observed. Doping with Fe^{3+}, Mo^{5+}, Ru^{3+}, Os^{3+}, Re^{5+}, V^{4+}, and Rh^{3+} at 0.1-0.5 at.% significantly increase the photoreactivity for both oxidation and reduction while Co^{3+} and Al^{3+} doping decreases the photoreactivity. The relative efficiency of a metal ion dopant depends on whether it serves as a mediator of interfacial charge transfer or as a recombination center. The ability of a dopant to function as an effective trap is related to the dopant concentration, the energy level of dopants within the TiO_2 lattice, their d electronic configuration, the distribution of dopants within the particles, the electron donor concentration, and the incident light intensity [40]. The transition metal ions are interesting for inducing a batho-chromic shift of the band gap. However, these dopings change other physical properties such as lifetime of electron-hole pairs and adsorption characteristics. For any photocatalytic reaction, the lifetimes of electrons and holes must be long enough to allow them to reach the surface of photocatalyst. When transition metals ions are incorporated into TiO_2, new trapping sites are introduced which affect the lifetime of the charge carriers. For instance, Cr^{3+} and Mo^{5+} doping decrease the TiO_2 lifetime from 89.3 μs to 30 μs and 20 μs for Cr-doped-TiO_2 and Mo-doped-TiO_2, respectively. Then, due to reduced lifetime of TiO_2 doped with Cr^{3+}, fewer charge carriers can reach the surface and hence initiate degradation of the dye. So, Cr-doped-TiO_2 presents lower photocatalytic activity by degradation of Rhodamine B then pure TiO_2 [31].

In the present thesis was chosen the metal element Nb^{5+} in order to be used as doping component into TiO_2. The ionic radius of Nb^{5+} (0.64 Å) is only slightly larger than Ti^{4+} (0.605 Å). Then, a solid solution can be formed into the TiO_2 lattice. To compensate the excess charge of Nb^{5+} in substitution to Ti^{4+}, one Ti cation vacancy may be created per 4 Nb introduced. Alternatively, the stoichiometric reduction of Ti^{4+} to Ti^{3+} may also occur depending on preparation conditions, which will introduce shallow donor levels below the conduction band (CB) edge of TiO_2 [41, 42]. The electronic transition from valence band (VB) to these donor levels will be excited by the visible light and therefore render the Nb-doped TiO_2 photocatalyst to be visible light responsive, such as nonstoichiometric TiO_2 [43].

Nb_2O_5-doped titania has been shown to have higher photocatalytic activity for the degradation of diquat dibromide monohydrate under UV-light as compared to pure TiO_2 [44]. Photocatalytic oxidation of 4-chlorophenol and iodide as well as the photoreduction of hexavalent chromate (Cr^{6+}) have been studied by Nb-TiO_2 catalysts, which presented enhanced photocatalysis under visible light [45].

Nonmetal-doped TiO_2 is also used to improve the TiO_2 photocatalytic performance. Various nonmetal elements, such as B, C, N, F, Cl, and Br, have been successfully doped into TiO_2 nanomaterials and a desired band gap narrowing was achieved. For instance, C-doped TiO_2 presents three deep levels located at approximately 0.86, 1.30, and 2.34 eV below the conduction band in C-doped TiO_2, which are attributed to the intrinsic nature of TiO_2 for the first one and the two levels newly introduced by the C doping [3]. Asahi *et al.* [46] have calculated densities of states of the substitutional doping of C, N, F, P, or S for O in the anatase TiO_2 crystal. The substitutional doping of N was the most effective because its *p* states contribute to the band gap narrowing by mixing with O 2*p* states. Even though S doping shows a similar band gap narrowing, it is difficult to incorporate it into the TiO_2 crystal due to its large ionic radius, as evidenced by a much larger formation energy required for the substitution of N.

Recently, Horovitz *et al.* [47] have used N-doped TiO_2 as a coated photocatalytic membrane reactor on α-Al_2O_3 membrane. The degradation of carbamazepine was studied for doped and undoped TiO_2 films. Applying full spectrum, the N-doped TiO_2-coated-membranes produced a significantly higher (by >100%) degradation rate than undoped TiO_2-coated ones. These improvements can be attributed to some facts, for instance, N atoms can act to narrow the band gap of TiO_2, making it capable of absorbing visible light and hence exhibiting *vis*-driven photocatalysis. Oxygen vacancies contribute to the *vis* activity and the doped N atoms can enhance the stabilization of these oxygen vacancies.

2.1.2.3 Superhydrophilic property

The term superhydrophilicity, also called superwetting, is referred to the water (liquid) apparent contact angle less than 5° [19]. As discussed before, when TiO_2 is irradiated by UV-light, it presents the well-known photocatalytic phenomenon. Moreover, titania

presents superhydrophilicity, which was discovered by accident in the laboratories of Toto Inc. in 1995. In that case, a TiO_2 film was prepared with a certain percentage of SiO_2, and acquired superhydrophilic properties after UV illumination. The electrons and holes produced react in a different way (Fig. 3). The electrons tend to reduce the Ti^{4+} cations to the Ti^{3+} state, and the holes oxidize the O^{2-} anions. In the process, oxygen atoms are ejected, and then oxygen vacancies are created. Subsequently, the water molecules can occupy these oxygen vacancies, producing adsorbed OH groups, which tend to make the surface hydrophilic [20].

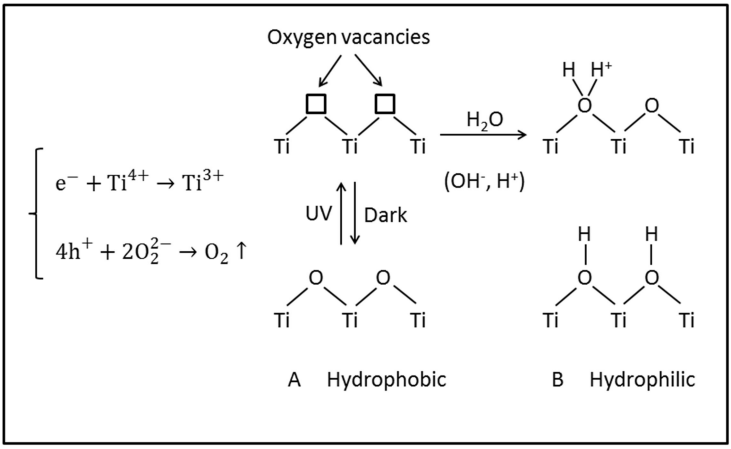

Figure 3. Mechanism of photoinduced hydrophilicity (adapted from [20]).

This phenomenon is reversible, though. Feng *et al.* [48] have fabricated TiO_2 nanorod films and found that the superhydrophobicity and superhydrophilicity could be switched back and forth. They have performed several cycles switching the nanorods from UV-light (2 h) and darkness (two weeks). After each cycle, the water contact angle turned to ~0° (superhydrophilic) or ~150° (superhydrophobicity). When the material is placed in the darkness, the adsorbed hydroxyl groups can gradually be replaced by atmospheric oxygen. Then, the surface evolves back to its original state, and the surface wettability converts from superhydrophilic to superhydrophobic again [48]. Strong evidence about this phenomenon is observed when the irradiated TiO_2 film is

exposed to pure O_2 gas in the dark. The water contact angle increment rate is remarkably accelerated [49].

Practical applications of superhydrophilic technology involve properties as self-cleaning, anti-fogging and biocompatibility, which can be applied to roads, houses, buildings, agriculture, electrical or electronic equipment, vehicles, consumer products and paints [20]. A self-cleaning material covered with TiO_2 can have this property since the organic contamination can be decomposed with the aid of ultraviolet light. However, the efficacy of self-cleaning surfaces was found to be dependent on the relative rates of decontamination vs. contamination. The TiO_2 photocatalyst can keep the surface clean only when the photocatalytic decontamination rate is greater than that of contamination [4]. Thus, Wang *et al.* [49] have suggested that the self-cleaning property is increased when the materials are used at external environments, where they can be exposed to water flow, such as natural rainfall. Several external products have been developed, such as tiles, glass and tents, which are based on the photocatalytic and superhydrophilic properties of TiO_2, and can be maintained clean by the action of sunlight and rainwater. As shown in Fig. 4, the organic matter, such as oil, is decomposed thanks to the TiO_2 photocatalytic properties. Additionally, organic contaminants and dust can be washed out by rainwater because of the superhydrophilic property of TiO_2 [50].

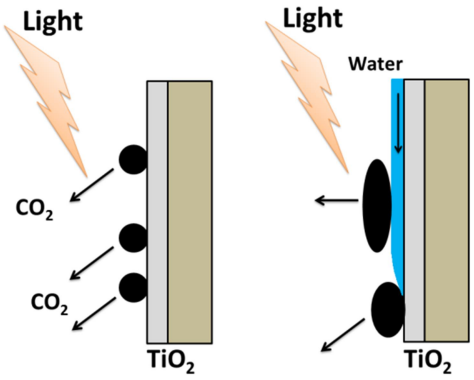

Figure 4. Schematic diagram of the decontamination process occurred on the superhydrophilic self-cleaning surface (adapted from [50]).

Naturally, the self-cleaning surface will not be clean forever. The process depends on the illumination conditions of sunlight, the

amount of rainfall, and the accumulation rate of organics and dirty. However, the self-cleaning surface will retard the rate of contamination, maintaining the surface clean for a long period. Thus, this can save a lot of time and cost for cleaning maintenance, particularly for high buildings and flexible plastic materials [50].

Recently, novel applications, which use TiO_2 properties, such as superhydrophilicity have been proposed in the literature. For instance, Léonard *et al.* [51] have made a stainless steel coated with TiO_2 and Multi-Walled Carbon Nanotubes (MWCNTs) doped TiO_2. The proposal was to increase the lifetime of steel materials. The combination of the three properties (anticorrosive protection, photocatalytic activity and superhydrophilicity) allows developing a material with low fouling and with a reduced corrosion. Therefore, the final material that can be set in inaccessible places has a longer lifetime. TiO_2 alone induces a decrease of the corrosion due to its photogenerated electron and due to a barrier effect. Introduction of MWCNTs enhances the anticorrosive property of TiO_2 by increasing the corrosion potential (anodic displacement) and decreasing corrosion current [51]. On the other hand, the superhydrophilic property of TiO_2 has been used to enhance the oil/water separation using poly(vinylidene fluoride) (PVDF) membrane. TiO_2 nanoparticles were directly anchored on the surface of PVDF membrane and the permeation flux for some oil/water emulsions was considerable high [52].

2.1.3 Crystalline Phases

The three main polymorphs of TiO_2 at atmospheric pressure are rutile, anatase, and brookite. The most stable one is rutile, while anatase and brookite are metastable [53]. Even though these are the main polymorphs, another five high-pressure phases of TiO_2 have been reported:

- TiO_2 II or srilankite, an orthorhombic polymorph of the lead oxide structure;
- Cubic fluorite-type polymorph;
- Pyrite-type polymorph;
- Monoclinic baddeleyite-type polymorph; and
- Cotunnite-type polymorph.

Several publications have discussed the stability of these phases. However, for research and development applications they are of minor significance [1].

Due to the difficulty of synthesis, brookite is also rarely studied. Thus, this chapter will focus at the two most studied phases in the literature, which are anatase and rutile. The crystal structure of these two phases can be described in terms of chains of TiO_6 octahedra, where each Ti^{4+} ion is surrounded by an octahedron of six O^{2-} ions. The difference between these two structures is the distortion of each octahedron and the assembly pattern of the octahedral chains. While a slight orthorhombic distortion is shown in the rutile octahedron, the anatase is significantly distorted, and then its symmetry is lower than orthorhombic. The distances among the atoms also are different from one phase to another. The Ti-Ti distances in anatase are larger, whereas the Ti-O distances are shorter than those in rutile. Furthermore, different mass densities and electronic band structures are observed between the two phases. Each octahedron of anatase is in contact with eight neighbors, four sharing edge and four sharing a corner. For rutile structure, each octahedron is in contact with 10 neighbor octahedrons, two sharing edge oxygen pairs and eight sharing corner oxygen atoms [3].

The exposed crystal faces influence TiO_2 properties, such as superhydrophilicity. Fig. 5 shows the three main crystal faces for anatase. The most predominant face is the plan (101) (Fig. 5a), which is corrugated, also with alternating rows of 5-coordinate Ti atoms and bridging oxygens that are at the edges of the corrugations. The (001) face (Fig. 5b) is rather flat but can undergo a (1 × 4) reconstruction. These two surfaces are common for natural crystals and they have low surface energies. The third presented face is the surface (100), which is less common on typical nanocrystals, but it is observed on rod-like anatase grown hydrothermally under basic conditions [4]. Rutile also has three main crystal faces, which are (110), (100), and (001). They are represented at Fig. 6a, 6b and 6c, respectively. The most thermally stable is (110), and consequently it has been the most studied one. It has rows of bridging oxygens connected to just two atoms. Then, the corresponding Ti atoms are 6-coordinate. However, there are rows of 5-coordinate Ti atoms running parallel to the rows of bridging oxygens and alternating with these. The (100) surface also has alternating rows of bridging oxygens and 5-coordinate Ti atoms. However, they are in a different geometric relationship with each

other. Between these three faces, the surface (001) is the one thermally less stable, restructuring above 475 °C [4]. It can also be mentioned that, owing to the different crystal structure and associated exposed planes of the two polymorphs, anatase has been reported to have a lower surface enthalpy and lower surface free energy than rutile [54].

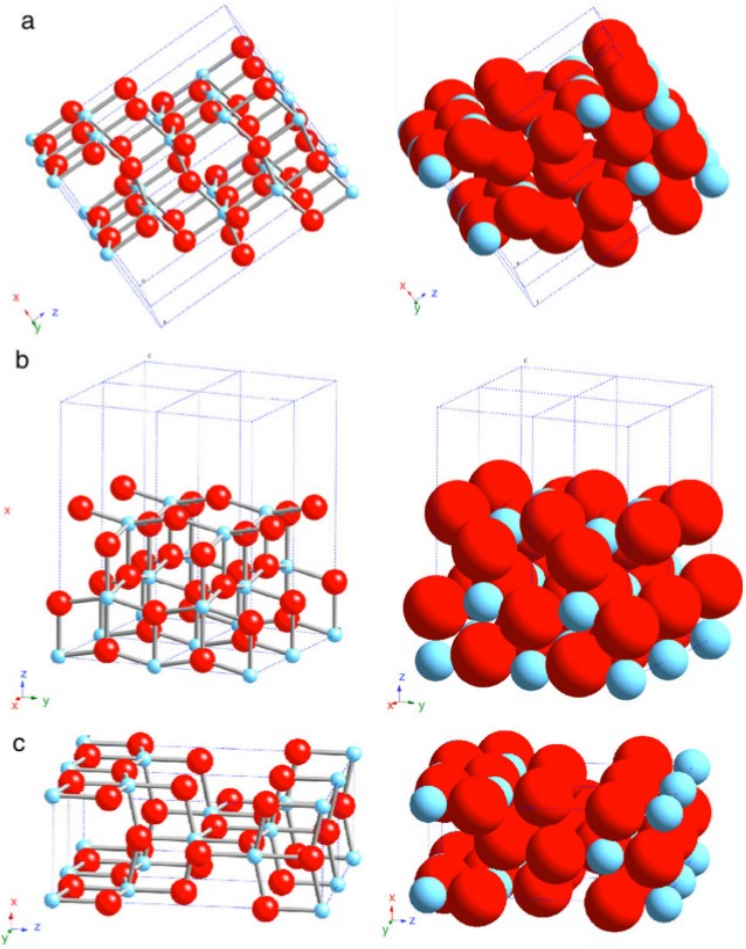

Figure 5. Schematic representations of selected low-index faces of anatase: (a) (101); (b) (100); and (c) (001) [4].

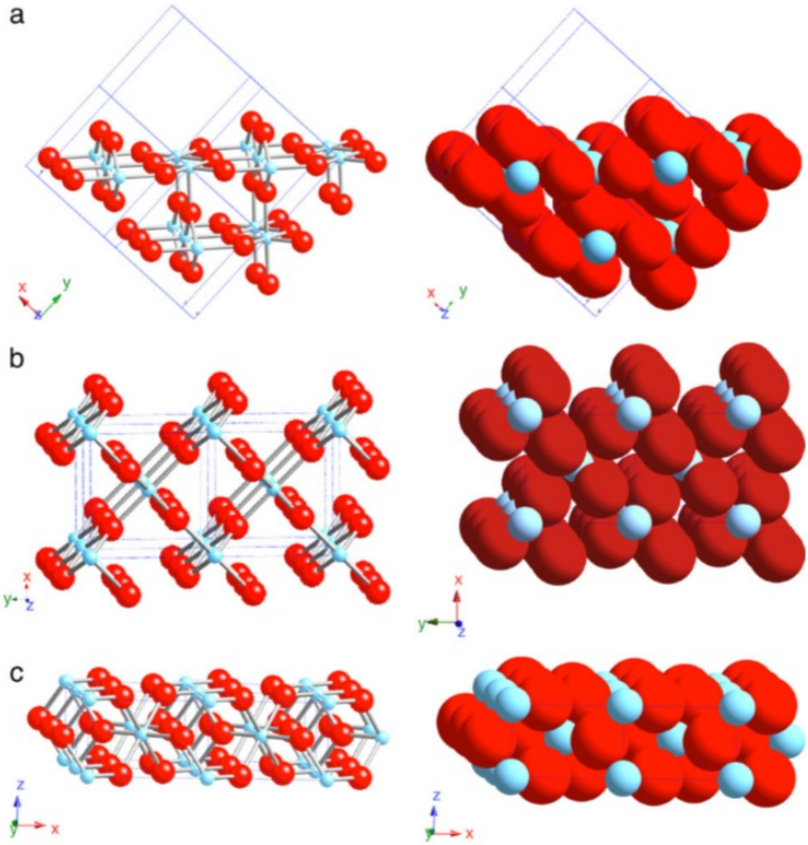

Figure 6. Schematic representations of selected low-index faces of rutile: (a) (110); (b) (100); and (c) (001) [4].

Other properties also differentiate anatase from rutile, as shown at Table 1. Both phases have tetragonal crystal structure, but anatase has four atoms per unit cell, while rutile has just two. It can also be noted that the lattice parameters and unit cell volume are different between the two. When anatase transforms to rutile, the lattice *a* and *b* extend a little, going from 0.3785 to 0.4594, and the lattice *c* shrinks from 0.9514 to 0.2958. Then, a change in density is expected between the two phases. Due to the lattice *c* shrinkage, rutile has a smaller unit cell volume and consequently higher density.

Another notable difference is the solubility of anatase in hydrofluoric acid (HF). This is an alternative method of measuring the rutile/anatase proportions. The anatase phase is dissolved, leaving the rutile phase intact. The disadvantages of this method is the health risk, potential loss of material during washing, loss of anatase, and potential for slight solubility of rutile. However, it could be useful for the removal of trace levels of anatase in order to enhance the purity of rutile powders [55, 56].

Table 1. Properties of anatase and rutile [1].

Property	***Anatase***	***Rutile***
Crystal Structure	Tetragonal	Tetragonal
Atoms per unit cell (Z)	4	2
Lattice parameters (nm)	a = b = 0.3785 c = 0.9514	a = b = 0.4594 c = 0.29589
Unit cell volume (nm^3)	0.1363	0.0624
Density ($kg.m^{-3}$)	3894	4250
Calculated indirect band gap	3.23-3.59 (eV) 345.4-383.9 (nm)	3.02-3.24 (eV) 382.7-410.1 (nm)
Experimental band gap	~3.2 (eV) ~387 (nm)	~3.0 (eV) ~413 (nm)
Refractive index	2.54, 2.49	2.79, 2.903
Solubility in HF	Soluble	Insoluble
Solubility in H_2O	Insoluble	Insoluble
Hardness (Mohs)	5.5-6	6-6.5
Bulk modulus (GPa)	183	206

Besides the differential solubility, anatase and rutile also can be identified by X-ray diffraction, laser Raman microspectroscopy and impedance spectroscopy. The X-ray diffraction is the most used method to identify and quantify the two phases. The results can be treated with the aid of a software to quantify the proportions of anatase/rutile [57], or the analyses can be performed manually using the method of Spurr and Myers [1]. This method uses the ratio of rutile (110) peak at 27.355° 2θ to the anatase (101) peak at 25.176° 2θ. The ratio of the intensities of those peaks, I_R/I_A, is used in the empirically determined formula (Eq. 1) to give the weight fractions of anatase and rutile:

$$\frac{W_R}{W_A} = 1.22\frac{I_R}{I_A} - 0.028\infty \quad (1)$$

However, the accuracy of the results using Eq. 1 can be affected by some factors, such as preferred orientation, encapsulation, lattice distortion, degree of crystallinity, grain size, morphology, and surface nucleation of rutile [1].

Another frequently used method to identify anatase/rutile phases is laser Raman microscopectroscopy. The respective phases have distinct Raman spectra, which can be used for qualitative and quantitative mineralogical analysis. This method has also been used quantitatively for on-line process control in the manufacture of titania powder by Hunstasman Tioxide Inc. [58]. Comparing to X-ray diffraction, the main advantage of the Raman method is the analysis of thin films. The materials require a considerable calibration in order to be analyzed by XRD, the peaks are very diffuse, and the background can be like any amorphous phase, which if it is present, cannot be determined. On the other hand, with laser Raman microspectroscopy, those problems do not happen, then the analyses are more sensitive and efficient [1].

The last and less used method to examine the anatase to rutile transformation is impedance spectroscopy, which was employed by Suresh *et al.* [59]. It measures the dielectric properties of a medium as a function of frequency. However, since the method relies on the difference in resistivity between the two phases, it presents two uncertainties associated with electrical resistivity measurement. The resistivity is a function of the grain connectivity, which is a microstructural factor rather than a mineralogical one. In addition, the electrical properties are affected by the dopants and impurities.

2.1.4 Anatase-to-rutile phase transition

The initial crystalline phase formed in the synthesis of TiO_2 is generally anatase. The crystallization from the amorphous hydroxide is an exothermic reaction and it has the activation energy (E_a) for the nucleation growth of 181 kJ/mol [60]. From the thermodynamic point of view, the anatase phase is formed first due to the lower surface energy at smaller grain sizes [7]. However, it is a metastable phase and it will transform to rutile at temperature varying from 400 to 1200 °C. The parameters that influence the transition temperature for undoped anatase are:

- particle size,
- particle shape,
- surface area,
- atmosphere,
- volume of sample,
- nature of sample container,
- heating rate,
- soaking time,
- impurities (from raw materials and container), and
- measurement technique [1].

The anatase-to-rutile transformation, also known as ART, is reconstructive. The transformation involves the breaking and reforming of bonds [61]. As shown in Table 1, the ART involves a contraction of the c-axis and an overall volume reduction.

For the ART proceed at a measurable rate, sufficient thermal energy is required to facilitate the rearrangement of atoms. This energy requirement is reached at ~600-700 °C in air in the absence of dopants or impurities. However, since the impurities are always present, the transformation can be enhanced or impeded by them. Furthermore, one of the most important factors that affect the ART is the presence and amount of defects on the oxygen sublattice. For instance, the increased levels of oxygen vacancies in reducing atmosphere during heating promote the phase transformation [1].

Both anatase and rutile phases have particular properties that can be crucial for specific applications. For example, in the photocatalytic field, the anatase has been cited as the most effective between the two [23, 62]. So, if the TiO_2 is used as a film on a material that requires high temperature process, the control of ART will be needed in order to avoid the phase transition and keep the performance of this material. On the other hand, if rutile phase is desired in processes that have temperature constraints, a manipulation on process conditions or material will be needed to promote the formation of rutile at lower temperature. Thus, the understanding of the stability of the TiO_2 polymorphs is an important tool to control the process.

One of the most used tools to promote or inhibit the anatase to rutile phase transition is the use of doping. The ionic radius and the valence is one of the factors that can direct influence the phase transition. Cations with small radii and low valence accelerate the transition to rutile. This is due to the increasing of oxygen

vacancies, which is result of the substitution of Ti^{4+} ions for cations with lower valences. In contrast, cations with valence >4 should inhibit the ART. Assuming that the cations of valence higher than 4 will substitute the Ti ions in the anatase lattice, this will annihilate the existing oxygen vacancies and the formation of Ti interstitials of the same or lower valence [1].

Besides doping, other parameters can affect the transition. For instance, thermal treatment in air or O_2 can inhibit the ART, mainly because of the filling of oxygen vacancies [63]. Furthermore, the grain size is a very important parameter that will affect the stability of the phase. The critical grain size or surface area where one phase is more stable than the other was determined by thermodynamic studies. Fig. 7 shows the phase diagram for nanocrystalline titania, as developed by Castro [5].

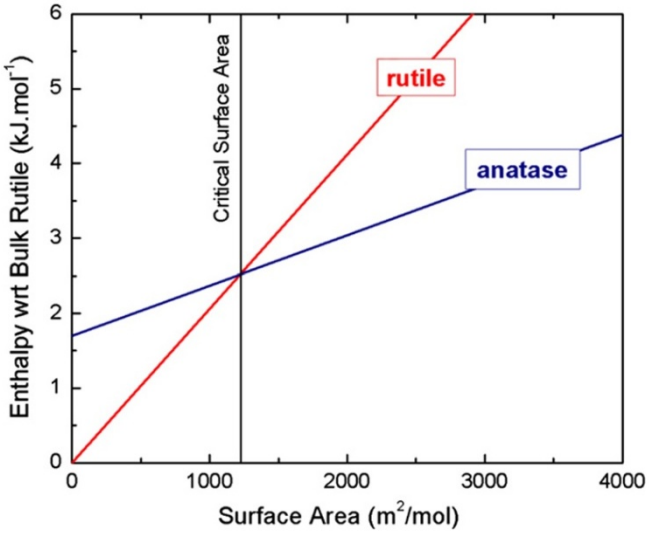

Figure 7. Phase diagram for nanocrystalline titania considering the surface contribution to the total energy of the system [5].

According to Fig. 7, decreasing particle size (increasing surface area), an energy crossover is observed between the phases at a critical size below which anatase is more stable than rutile. Considering that anatase has lower surface energy than rutile, this behavior can be predicted using Eq. 2.

$$G_{sys} = G_{bulk} + \gamma A \quad (2)$$

where G_{sys} is the total free energy; G_{bulk} is the bulk free energy; γ is a general term accounting for the interface energies; and A is the respective area. This equation takes into account that nanocrystalline ceramics are thermodynamically non equilibrium states. Increasing surface area (decreasing particle size) one should expect that the total free energy of rutile nanoparticles would increase faster with surface area than anatase [5].

3. A REVIEW ON PHOTOCATALYTIC CERAMIC TILES: TECHNOLOGY AND CHALLENGES[1]

A review of the latest research in photocatalytic ceramic tiles was made in this chapter. It is discussed the methods used to deposit the particles on the surface, highlighting the advantages and disadvantages of each method. The adhesion of TiO_2 on the surface of ceramic tiles is evaluated and the main tests presented. The influence of the TiO_2 on the characteristics of ceramic tiles, as color, brightness, cleanability and roughness is discussed according to the available data. Finally, the photocatalytic performance is shown and the problems faced to compare those data are discussed.

3.1 Introduction

The production of ceramic tiles with improved technical and/or esthetical properties has received special attention in the last years. The implementation of new technologies that are able to aggregate value to the final product, as decoration with high definition [64] or low thickness products [65, 66] opened the market for functional tiles, with tasks that go beyond the traditional applications [67]. Recently, efforts to produce self-cleaning materials using TiO_2 on the surface of ceramic tiles have been intensified. These novel products facilitate to keep the building exterior clean by utilizing solar energy through photocatalytic (PC) phenomena [68]. However, manufacturing these tiles requires special attention, as well as further processing steps.

The knowledge of the phenomena involved in such photocatalytic activity and superhydrophilic properties of TiO_2 is crucial to make a successful self-cleaning product. For ceramic tiles, critical aspects have to be considered: high sintering temperature, reaction between TiO_2 and substrate, adhesion of the TiO_2 film/particles and changes in the appearance of the tile surface. The lack of control of one or more of these aspects can result in products that will not work properly or will lose the properties over time. For instance, Ducman *et al*. [69] have measured the degradation of methylene blue (MB) of four commercial ceramic tiles named as photocatalytic products available on the market. Not surprisingly, their PC efficiency was very different: the best performance was 62% MB decomposition

[1] To be submitted for publication.

after 6 h, while the worst one was just 3% after the same period of time (the other two were 15% and 41% of MB degradation). Those differences are a good example of problems that may arise in the industrial production of PC ceramic tiles.

Indeed, the technological and scientific parameters to be kept under control for a suitable industrial scale application are not completely understood yet. Some of those parameters are connected with the need of immobilizing the photocatalyst on the ceramic tiles by suitable powder deposition and sintering techniques. This implies in the modification of the production cycle, including an additional annealing step at a temperature that is a compromise: not too high (to avoid the anatase-to-rutile transformation, ART), but high enough to achieve a good adhesion of TiO_2 particles on the ceramic substrate. In fact, it is necessary to obtain materials that are able to maintain their additional functionalities over time in different working conditions [70].

Besides the self-cleaning properties, ceramic tiles coated with photoactive TiO_2 can present other properties as antibacterial activity, i.e., a bacteriostatic action. These materials could be used in hospitals, schools, restaurants, houses, or any place that needs a especial attention for the human health [71]. The purpose of these materials is to kill fungi and bacteria from the surface of ceramic tiles, having by this way a self-sterile ceramic tile. Moreover, TiO_2 coating on the surface of ceramic tiles can be also exploited as a re-usable photocatalytic material for water cleaning. Instead of having suspended powders, which must be filtered afterwards, PC tiles can be used as catalyst support after mere rinsing of the tiles with water and without affecting the photocatalytic activity [72, 73].

Considering this promising picture, some efforts have been spent to improve the photocatalytic performance of the coated ceramic tiles. The use of doping or coupled photocatalyst materials may be an alternative to increase the photoactivity performance [57, 74]. The doping can even shift the ART to higher temperatures, allowing a higher annealing temperature to improve the adhesion or also increase the photocatalytic performance of the ceramic tiles produced at the same temperature using pure TiO_2.

Another important aspect to be aware when planning the development of photoactive ceramic tiles on an industrial scale is the PC performance. Usually the results achieved with TiO_2 powders in a suspension do not match with those after final coating. In many cases, a considerable decrease in performance was

observed, since the formation of films reduce significantly the total surface area available for reaction. Seabra *et al*. [73] have studied the degradation of Orange II dye for four different powders. Curiously, the powder with higher PC performance suspended in water did not correspond to the most efficient when applied on ceramic tiles.

Thus, the aim of this work is to critically review the information available in the literature about photocatalytic ceramic tiles, especially for TiO_2 coatings. The purpose is to discuss obstacles and challenges to the diffusion of photocatalytic tiles. This review is divided in five sections: deposition methods; adhesion of TiO_2 on ceramic tiles; effects on the substrate, like color, brightness, cleanability and roughness; the photocatalytic properties; and the characterizations performed on the coatings.

3.2 Deposition methods

The deposition method represents a key step in the production of photocatalytic ceramic tiles. Its choice directly influences some basic parameters, such as the total amount of TiO_2 deposited, the layer thickness, and surface roughness, which in turn are closely related to the PC performance of the products. Moreover, other aspects such as surface area of TiO_2 layers, particles adhesion on the substrate and the TiO_2 polymorph can markedly affect the PC performance and durability over time. On the other hand, in most cases it is strictly necessary to preserve the surface properties of the ceramic tiles in terms of color, brightness and cleanability after the functional layer deposition [69, 70].

Most of the works available in the literature refer to deposition methods already used on glaze lines for decoration purpose. However, some methods applied at laboratory scale are not easily transferrable to the industrial scale. Examples of these methods are liquid phase deposition (LPD) [71] and dip coating [75-77]. Both methods consist in the immersion of the tiles in suspended TiO_2 particles or their precursors (i.e. titanium hydroxide) followed by controlled emersion at a given rate. These methods imply that both sides of the samples will be coated by the TiO_2 containing solution, leading to an increase of production costs. Moreover, especially for LPD, the time requested to keep the tile immersed in the solution is too long. This aspect is in contrast to the high speed required in the production lines nowadays [71]. Table 2 shows the deposition

methods that have already been tested for application of TiO_2 on the surface of ceramic tiles. As it can be seen, spraying is the most used technique at lab scale due to the simplicity and availability of the method. Furthermore, it can be easily transferred to the production lines.

Table 2. Methods to deposit TiO_2 on the surface of ceramic tiles.

Deposition Methods	***TiO_2 film thickness (µm)***	***Roughness (nm)***	***Advantages***	***Disadvantages***
Spraying [68, 69, 74, 78-83]	0.1 – 3.0 [69, 74, 79, 81, 82]	10 – 30 [82]	Low cost; Easy operation; Thin TiO_2 films; Homogeneous coatings	Control of processing parameters in automated conditions
Screen Printing [72, 84]	5.0 – 35.0 [72, 84]	~299 [84]	Well-established technique; Low cost	Use of organic medium; Thick TiO_2 thickness; High roughness
Ink Jet Printing [70]	~70.0 [70]	No information	No contact with the tiles; Patterning of surfaces	Thick TiO_2 thickness
Roller Printing [70]	~100.0 [70]	No information	Easy process	Direct contact with the tile; Need of controlling the texturing of roller surface; Thick TiO_2 thickness
Dip Coating [75-77]	No information	60-690 [72, 84]	Very thin film	Low speed process; Both sides coated
Liquid Phase Deposition (LPD) [71]	~0.2 [71]	No information	Very thin film	Low speed process; Both sides coated

The data showed in Table 2 only refer to TiO_2 coatings on ceramic tiles, bringing back a great evidence of the huge variation on thickness and roughness according to the method used. Details about the methods as well as the differences among them are discussed hereafter.

3.2.1 Spraying

Spraying is currently the most common technique to deposit TiO_2 on the surface of ceramic tiles as it comes out from more than 50% of the works available in the literature. Usually, tiles manufactures already have glazing lines equipped with spraying machines to apply water after drying and subsequently, to deposit glazes on the ceramic tiles. This can enable the technology transfer, making the process sortable for the industrial scale [69, 74]. As it can be seen in Table 2, the thickness of sprayed coatings typically are in the 0.1-3.0 μm range, which is very thin if compared with those obtained by roller printing, ink jet, or screen printing [70, 72, 84]. Regarding to the roughness, just one work has reported data using spraying (10-30 nm), which are the lowest values in Table 2. Of course, these data do not depend just on the deposition technique. It can vary according to the glaze and substrate parameters, especially when very thin coatings are produced.

Spraying can use TiO_2 suspensions [69] or a synthesized sol [68, 74], or even a mixture of TiO_2 powders with glazes [80]. The TiO_2 particles can be as small as 7 nm [69, 79] and the PC performance of the coated ceramic tiles will depend on the TiO_2 used, sintering temperature, and crystalline phase. The amount of TiO_2 suspension deposited on the ceramic tiles can be regulated adjusting the line speed in a continuous process. For manufacturing plants where very high speed is needed, two or more spraying heads may be used.

3.2.2 Screen printing

Screen printing is a well-established decoration technique used in ceramic tiles manufacturing. Its introduction at industrial level can be dated back to 50 years ago - flat and rotary screen printing, to 1960s and 1970s, respectively. Moreover, flexographic and intaglio printing were introduced in the 1990s [64]. Currently it is utilized to produce special decorations during second or third firing.

The method has been recently tested to deposit TiO_2 on ceramic tiles [72, 84] for functional purposes. Positive results in terms of PC degradation of orange II under UV-light [85], visible light [72] and sunlight irradiation [84] have been reported. The research typically uses commercial powders available on the market as TiO_2 from Kronos [72, 84] or Degussa P25 [85], dispersed in a suspension medium (often an organic one) properly deposited [72]. However,

the use of these organic media can decrease the PC performance of the coated ceramic tiles. In fact, depending on their physical properties, i.e. the degradation temperature or even the softening point, organic vestiges can remain as covering of the deposited TiO_2 particles or as undesired impurities among them. Thus, it will reduce the number of active surface sites available for the catalytic process [72, 73].

If compared to other methods, screen printing generates thicker layers with a typical thickness in the 5-35 μm range [72, 84]. This could be a disadvantage, since the use of materials at the nanoscale requires lower amount of powders for the required properties due to their high surface area and reactivity. The thickness and the amount of TiO_2 deposited on ceramic tiles can vary according to the sieving screens used. It has been reported, for example, that a 55 μm sieving screen can deliver 25 g/m² of TiO_2, while a 136 μm sieve, 50 g/m² TiO_2 [72].

Rego *et al*.[84] have reported roughness values of ~300 nm using AFM. Marcos *et al*. [72] have shown SEM micrographs for screen printed samples fired at different temperatures. The TiO_2 layers presented a granular texture that could be of interest for PC purposes due to the increased surface area. However, the same group has reported later that the screen-printing process causes an unpleasant appearance of the ceramic tile surfaces with a high degree of roughness that makes it more difficult to be cleaned. All these features can represent a drawback for screen printed PC tiles [73].

3.2.3 Ink jet printing

Ink jet printing is a recent innovation for decorative purposes in the production of ceramic tiles. Its introduction improved the quality of printing on the ceramic support providing the surfaces with a wide range of esthetical features. If compared to other methods, the advantages are mainly related to the fact that it is a non-contact, digital process. Therefore, fragile or non-flat substrates, which are difficult to treat with screen or roller printing, can be processed without any restriction [86].

Ink jet printing is based on the digitally controlled ejection of drops of fluid from a print head onto the substrate. The ink-jet printers are classified as either continuous (CIJ) or drop-on-demand (DOD). The last one, which is widely used in tiles manufacturing,

allows to deposit a precise quantity of functional ink on the substrate in the form of droplets. The process essentially involves the ejection of a fixed quantity of ink from a nozzle through a sudden, quasi-adiabatic reduction of the ink chamber volume via piezoelectric action. A chamber filled with liquid is contracted in response to the application of an external voltage. This sudden reduction sets up a shockwave in the liquid, which causes a liquid drop to eject from the nozzle. The ejected drop falls due to gravity and air resistance until it impinges on the substrate, spreads under momentum acquired in the motion, and surface tension aided flow along the surface. The drop then dries through solvent evaporation [64].

This technique has been recently tested for application of TiO_2 films on ceramic tiles. It is suitable for covering large areas with TiO_2 in a continuous high speed process [70]. A thickness of TiO_2 ink jet printed layers of about 70 μm has been reported, which is quite similar to the typical range (~65 μm) cited in the literature for decorative ink applications. Indeed, it can be considered thick, if compared to that delivered by spraying techniques (0.1-3.0 μm) [86]. Raimondo *et al*. [70] have compared the deposition of TiO_2 dispersed nanopowders by ink jet and roller printing. It was observed by high magnification SEM images that both methods produce TiO_2 particles assemblage as flakes moieties, whose distribution and frequency depend on the deposition technique. The flakes are larger when roller printing is used and higher amount of TiO_2 is deposited. However, at higher annealing temperatures (up to 1000 °C) the surface becomes smoother in both processes. Regarding to the superhydrophilic property, all coated samples fired up to 800 °C presented water contact angle lower than 5° after 2 h under UV-light irradiation. The wettability before irradiation varies from 20° to 50°, decreasing on coated samples with higher annealing temperatures in accordance with the simultaneous reduction of surface roughness.

3.2.4 Roller printing

Roller printing is a decorative technique that has been widely employed in the industries since 1990s. A common roller printer uses a silicon roll, which is formed by small holes that are filled with the ink and transferred to the ceramic tiles by direct contact with the tile surface. The technique has been tested for application of TiO_2 films on ceramic tiles [70]. The outcoming superhydrophilic performances were similar to those provided by TiO_2 printed by ink jet, as discussed before. However, the thickness of the coatings increased up to about 100 μm, which is the highest value provided by all techniques. This potentially involves an undesired worsening of the esthetical appearance of tiles.

Another hindrance of this technique is a possible presence of small spaces between the drops deposited, which may reduce the overall photoactivity of the products. For overcoming this drawback, it is necessary to design special rolls with smaller holes and smaller spaces among them.

3.2.5 Glazing

Some researchers have mixed TiO_2 with glaze and then applied it on the ceramic tiles by different processes, e.g. dip coating [75] or spraying [80]. Glazing might be very convenient, since the particles could be deposited with no additional equipment on the production line. The problem faced with this practice is related with the exposed surface area of TiO_2 particles. If titania is mixed with the glaze, most particles will be trapped in the glazed film. Thus, just few particles will be exposed on the surface, which will decrease the photoactivity of the ceramic tiles. Moreover, high amounts of TiO_2 mixed with glaze can result in cracks after sintering [75], which is an undesired effect.

Tezza *et al*. [80] have studied the degradation of MB using TiO_2 powders mixed with frits. After sintering at 850 and 900 °C, the photocatalytic activity was very low, showing just a little degradation after 5 h under UV-light. The lower performance was attributed to the large particle sizes of TiO_2, to the anatase-to-rutile transformation, and also to the fact that the TiO_2 particles were surrounded by melted frits, which decreased the TiO_2 sites exposed for the photocatalytic activity.

3.3 Adhesion

The adhesion of functional layers on a given substrate is one of the most critical variables directly affecting the long term performance of the products. Among the papers dealing with PC ceramic tiles, less than 30% have tested this property and most of them come from the same group. Even when the material works well at a first moment, it is not guaranteed that the same performance will remain over time. Therefore, in case of a material with a lifetime of 10 to 20 years, the aim of making a self-cleaning ceramic tile will be ruined if the TiO_2 goes away over time. In this way, some efforts have been done to evaluate the adhesion of the TiO_2 coated ceramic tiles. However, specific studies that can provide standard values to be used for industries in order to estimate the material durability are still missing.

Nevertheless, some researchers approached the problem of improving the particles adhesion to the substrate, for instance by increasing the sintering temperature or introducing adhesion promoters between the functional layer and the substrate. Seabra *et al*. [73] have deposited TiO_2 on glazed ceramic tiles and have reported that, when the samples are fired at temperature as high as 950 °C, the coating results firmly adhered to the substrate. However, when annealing steps were performed at 850 °C, the coating's adhesion revealed not to be sufficient and the removal of powder was easy even by touching. They have also tried to increase the content of serigraphic base with the aim of increasing the adhesion, but its presence was deleterious for the PC performance of the coated ceramic tiles. The annealing temperature is another processing parameter to be strictly controlled to avoid loss of PC activity. As already discussed, the PC efficiency is reduced due to the transformation of anatase (PC active phase) to rutile (PC inactive phase) and the consequent grain growth with the lowering of the specific surface area [87].

In the literature, some experimental procedures have been proposed to evaluate the adhesion of the TiO_2 films on ceramic tiles. In this review, some of them were selected and a brief description is provided.

3.3.1 Scratch test

The scratch test has been used to verify the adhesion of TiO_2 coated on unglazed porcelain stoneware [81-83], glazed [83], and polished ceramic tiles [82]. Specific equipment can be designed to characterize the adhesion of the surface coating or alternatively it can be used equipments designed to evaluate the scratching resistance of the material. The experiment consists in making a scratch on the surface of the coated ceramic with a linearly increasing load (e.g. 0.1-30 N) at constant speed. Commonly a diamond tool is used as the scratching indenter. The output of the progressive load scratch tests are called Lc1, which is the load where the first cracking occurs and Lc2 that is the load at each catastrophic failure begins. In other words, Lc1 shows the maximum force the coating resists before presenting any visual effect on it and Lc2 shows the force at which the coating is completely removed. In order to obtain a precise result, the scratches can be observed by optical microscopy. Some equipment already come with an attached microscope, which makes the analysis easier. Fig. 8 shows a typical example of scratch test on unglazed porcelain tile coated with SiO_2/TiO_2, in which the coating resistance increases as TiO_2 ratio and temperature increase [81].

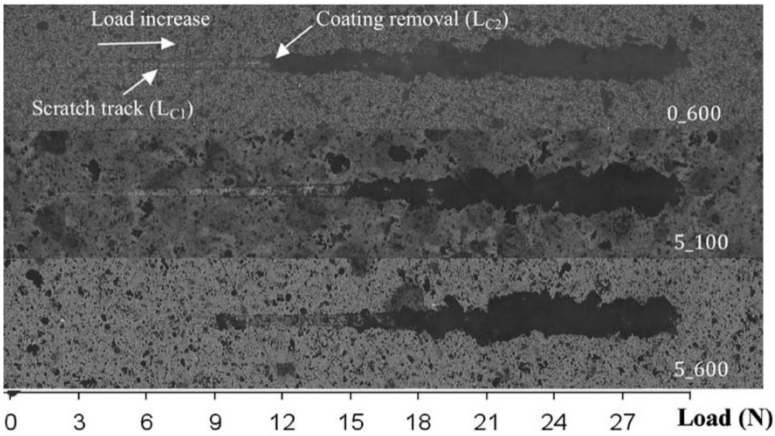

Figure 8. Optical image of the samples after the progressive scratch test [81].

This method was also used to evaluate the adhesion of TiO_2 doping in films. The analysis was carried out for undoped TiO_2 films and Ag-doped-TiO_2 films. The results have shown no significant difference from doped and undoped TiO_2 films [82].

3.3.2 Alternative Methods

Some authors have reported some alternative ways to evaluate the TiO_2 adhesion on ceramic tiles. Murugan *et al.* [68] have used the the tape test (ASTM D3359-08 Method B). According to them, the thin TiO_2 film coated by sol gel has not presented significant delamination, corresponding to a 5B level, which is the maximum adhesion according to the test. This method will not be explained in detail here, because it actually covers procedures for assessing the adhesion of coatings on metallic substrates which is not the scope of this review.

An alternative test was performed by Raimondo *et al.* [70] on TiO_2 films coated by roller printing and ink jet printing. They have used brushing abrasion (2500 cycles) in the presence of a neutral detergent. Then, the water contact angle was measured before and after the aged surfaces. It was found that higher temperature (e.g. 800 °C) and larger amounts of TiO_2 (~ 4.6 g/m² TiO_2) can maintain the superhydrophilicity. However, for lower amounts of TiO_2, e.g. <3.6 g/m² and lower temperature (e.g. 400 °C) the superhydrophilicity was lost.

3.4 Effects of the TiO_2 coating on ceramic tiles

The ideal scenario for TiO_2 coated ceramic tiles should be a transparent thin film that does not affect any characteristic of the product. Nevertheless, some properties, such as color, brightness, cleanability, roughness and durability of the TiO_2 coatings may vary after coating with titania.

3.4.1 Color

Color is a very important control parameter for ceramic tiles, which influences directly the product final quality. Efforts have been done along the years to understand how to keep the tonality constant among the tiles, e.g. by analyzing the effect of ink density and mesh opening gradient on color variation [88]. Thus, it is

important that a TiO_2 coating on ceramic tiles does not have any side effect on this property.

The color changing on coated tiles can be evaluated by UV-vis spectroscopy using the CIELab method. The method defines a color through three parameters, L*, a* and b*, which correspond to brightness, red/green and yellow/blue color intensities, respectively. Moreover, a color difference can be defined as ΔE*, based on the relationship described by Eq. 3.

$$\Delta E^* = [(\Delta L^*)^2 + (\Delta a^*)^2 + (\Delta b^*)^2]^{\frac{1}{2}} \quad (3)$$

where ΔL*, Δa* and Δb* correspond to the differences in luminosity and in chromaticity between the two colors. If ΔE* is <1, it means that there is no hue variation. This method has been used to evaluate the hue variation on unglazed and glazed porcelain tiles coated with SiO_2/TiO_2 (wt% ratio 95/5) [81, 83]. The results have not shown any difference in the visual aspect, since ΔE* was lower than one. On the other hand, Ag-doped-TiO_2 samples have shown some variation in color when applied on glazed ceramic tiles [82]. It is worth notice that those evaluations were made with TiO_2 coated by spraying, which provides a thin film thickness.

3.4.2 Brightness

Brightness can be defined as the luminance of a body. Apart from its hue or saturation, which an observer uses to determine the comparative luminance of another body, the reflection parameters can be evaluated using the gloss of the sample. An instrument called glossmeter can be used to measure specular reflection gloss of a surface. It is determined by projecting a beam of light at a fixed intensity and angle onto a surface and measuring the amount of reflected light at an equal but opposite angle. This parameter is correlated with the surface roughness of the samples. So, the value tends to be higher for glazed ceramic tiles comparing to unglazed ones [82]. The amount of TiO_2 and the temperature can affect this characteristic; higher temperature and higher amount of TiO_2 decrease the absolute value of the gloss of the sample [81-83].

3.4.3 Cleanability

Ceramic surfaces are often used when an easy-to-clean surface is needed, for instance, in hospitals and in industrial clean rooms or domestic kitchens and bathrooms [76]. Thus, it is important that the TiO_2 coating does not affect this essential function of the ceramic tile surface. Cleanability is associated with the stain resistance, which may be interpreted as the difficulty of removing any substance in contact with the surface without reacting with it. Stain resistance varies widely in ceramic tiles, depending on the type of surface. For unglazed polished porcelain stoneware, the resistance to stains is proportional to the concentration of surface defects, either inherited by the ceramic body (i.e. pores) or originated during polishing (e.g. grooves, scratches) [89].

The measurements can be addressed using a standard procedure, e.g. ISO 10545 – Part 14, which specifies a method for determining the resistance to stains of the surface of ceramic tiles. The surface of the tile is maintained in contact with various test solutions (staining agents) for a sufficient period of time. Then, the tile is subjected to specific cleaning procedures and, finally, it is examined to detect any irreversible changes in appearance [90].

TiO_2 thin films on ceramic tiles should not change the original cleanability of the glazed ceramic tile. Kuisma *et al.* [76] have demonstrated that the cleanability of TiO_2-coated ceramic glazed surfaces remain unchanged after heat treatment at 500 °C. The maintenance of cleanability was possible thanks to the low roughness. On the other hand, the cleanability also depends on the deposition method used. Seabra *et al.* [73] have reported that screen-printing gives to the ceramic tile surface a high degree of roughness and consequently it makes them difficult to clean.

Despite a high rough surface has normally low cleanability, under UV-irradiation this property is improved for soil containing organic particles. This is attributed mainly to the higher photocatalytic activity due to the increased surface area. However, for oil soil the UV-radiation does not show any improvement in the cleanability of the coated ceramic tiles [77].

3.4.4 Roughness

The roughness of ceramic tile surface influences aspects as cleanability, visual effects as brightness and properties as anti-

slipping. Thus, if the original characteristics of ceramic tiles are desired to be maintained, the TiO_2 coating should not change the roughness of the surfaces. On the other hand, if the purpose of the coated ceramic tiles is to act as a photocatalyst for water cleaning, a higher surface roughness is desired. This is because the surface available will be larger and the photocatalytic reaction rate will be increased as well [91].

The roughness of TiO_2 coated ceramic tiles has been measured using contact profilometry [76] and atomic force microscopy (AFM) [82, 84]. In the first one, the average roughness (Ra) is based on the centerline of a surface, and it describes the average height or depth of the peaks above and below the centerline. The Ra value usually stated in μm is the most commonly used descriptor of surface roughness and it can be calculated in both two and three dimensional forms [76]. AFM is a kind of scanning probe microscopy that can provide a 3D profile on a nanoscale by measuring forces between a sharp probe (radius less than 10 nm) and a surface at very short distances (0.2-10 nm probe-sample separation).

In order to consider the ceramic tiles hygienic, Ra has to be lower than 0.8 μm. In Table 2, all ceramic tiles coated with TiO_2 are below of this value [76, 77, 82, 84], which shows that the tiles can be coated by TiO_2 films and the hygienic properties can be maintained.

3.4.5 Durability

The durability of TiO_2 coating on ceramic tiles has rarely been investigated. It can be performed using a standard procedure, such as UNI-EN 1096-2. This method is related to artificial weathering of coatings on glass for buildings in outdoor and indoor applications [92]. Sciancalepore *et al*. [83] have evaluated the durability of SiO_2-TiO_2 coating on ceramic tiles, after aging treatments within a climatic chamber. For condensate resistance, the test was performed for 21 days in air at constant temperature (40 °C); for acid resistance, the test was conducted for 5 days in a SO_2-saturated atmosphere; and finally, for salt spray resistance, it was performed for 21 days at constant temperature (40 °C) with a 5 g/L NaCl solution. The samples were analyzed before and after the tests by SEM and the results showed a very homogeneous and intact coating, which was not altered by the performed treatment. In fact,

even if some defects were present, they did not affect the functionality of the coating.

3.5 Photocatalytic properties of coated ceramic tiles

One of the objectives of making a photocatalytic ceramic tile is to have a self-cleaning surface. This specific characteristic is governed by two properties of TiO_2: the photocatalytic degradation of organics, and the superhydrophilicity. The decomposition of organics will work if the rate of decontamination is higher than the contamination. For external applications, the superhydrophilic property also helps to keep the tiles clean. The action of the increased wettability of water from the rain will create a thin water film, washing out dusts from the surface of the ceramic tiles [4, 49, 50].

However, the coated surface will not present necessarily both properties at the same time [20]. The works available in the literature rarely evaluate those characteristics simultaneously. Table 3 shows 18 selected references that dealed exclusively with photocatalytic ceramic tiles. It shows photocatalytic tests and which dye was used in the case of dye degradation. Just five of those studies have dealed with degradation of dyes and water contact angle at the same research. Of course, it has to be considered that some researchers have focused their efforts on other aspects, as antibacterial materials [71, 75], or water remediation applications [72, 84].

Table 3. Photocatalytic tests performed on photoactive TiO_2 coated ceramic tiles.

Ref.	Degradation of dyes	Dyes used	Water contact angle	Anti-bacterial action	Degradation of NO_x
Hasmaliza, 2016, [75]	No	---	No	Yes	No
Sciancalepore, 2015, [83]	Yes	MB	Yes	No	No
Tezza, 2015, [80]	Yes	MB	Yes	No	No
Ke, 2014, [74]	Yes	MB	No	No	No
Niederhausern, 2013, [82]	Yes	MB	Yes	Yes	No
Ducman, 2013, [69]	Yes	MB	No	No	No
Murugan, 2013, [68]	Yes	MB	No	No	No
Petrovic, 2012, [79]	Yes	MB, Rhodamine and Crystal violet	No	No	No
Raimondo, 2012, [70]	Yes	MB	Yes	No	Yes
Seabra, 2011, [73]	Yes	Orange II	No	No	No
Bondioli, 2009, [81]	Yes	MB	Yes	No	No
Rego, 2009, [84]	Yes	Orange II	No	No	No
Ruiz, 2009, [85]	Yes	Orange II	No	No	No
São Marcos, 2008, [72]	Yes	Orange II	No	No	No
SUN, 2008, [71]	No	---	No	Yes	No
Kuisma, 2007, [76]	No	---	No	No	No
Maatta, 2007, [77]	No	---	Yes	No	No
Kemmitt, 2004, [78]	Yes	Rhodamine	No	No	No

The degradation of dyes was performed in the majority of the papers, while water contact angle, anti-bacterial and degradation of NO_x were measured less frequently. Degradation of NO_x was only evaluated once [70].

Particularly, water contact angle measurements and degradation of methylene blue seems to become a standard experiment for PC ceramic tiles. This dye is also the most common used; orange II, rhodamine and crystal violet were less commonly employed.

In the next sections, the experiments are discussed individually.

3.5.1 Photo-degradation of dye

The photo-degradation of dyes is the main test performed on PC ceramic tiles. Dyes are frequently used as model pollutant substances because their concentration can be easily examined using a spectrometer [79]. Hereafter, the degradation of methylene blue and orange II, which represent the main tested dyes on PC ceramic tiles, will be discussed.

3.5.1.1 Methylene blue

Degradation of methylene blue is widely tested on catalysis field. It has become a very popular dye due to its highly colored nature, good chemical stability, and low cost [79]. A standard test for determination of photocatalytic activity of surfaces in aqueous medium by degradation of methylene blue was published in 2010 (ISO 10678:2010) [93]. This standard applies artificial ultraviolet (UV) radiation and describes the parameters and apparatus to be used. The three main steps are: (1) pre-irradiation to decompose any possible organic contaminants remaining by photocatalytic oxidation on the surface of the material tested; (2) pre-adsorption of MB solution on the surface of the PC ceramic tiles; (3) and photocatalytic test itself. The results are expressed by the specific photoactivity, P_{MB} (Eq. 4) or by photonic efficiency, ζ_{MB} (Eq. 5).

$$P_{MB} = R_{irr} - R_{dark} \quad (4)$$

where R_{irr} is the specific degradation rate with UV radiation and R_{dark} is the specific degradation rate without UV radiation.

$$\zeta_{\mathrm{MB}} = \frac{P_{\mathrm{MB}}}{E_{\mathrm{p}}} \times 100 \quad (5)$$

where E_{p} is the photo UV-radiation intensity.

A Japanese Industrial Standard, (JIS R 1703-2) presents an alternative procedure to ISO 10678, but the results are represented by the decomposition activity index, R (μmol/L/min). This value is calculated from the gradient of the straight line of MB concentration C(t) and the ultraviolet light irradiation time [94].

Alternatively, several other parameters have been applied to evaluate the photoactivity of ceramic tiles. Thus, a comparison of this property in ceramic tiles is not straightforward, since there are different experimental parameters and forms to show the results. For instance, the volume of MB during the experiment according to the ISO and JIS is 35 mL. However, in the experiments this value varies from 6 to 150 mL; the total reaction time, which supposed to be up to 3 h, varies from 3 to 8 h; the time interval to measure the absorbance is in the range from 20 min to 2 h (whereas every 20 min is the reference). Moreover, the concentration of MB varies from 10 to 15 μmol/L and the UV light intensity from 10 to 20 W/m².

A practical experiment to evaluate the self-cleaning property was suggested by Murugan *et al*. [68] for TiO_2 coated glazed ceramic tiles (Fig. 9). A tile was divided in two zones, TiO_2 coated (bottom) and uncoated (top). A permanent marker stain was applied on the surface and the tile was left under sun light for 55 h. The stain made on TiO_2 coated zone is hardly visible after the test, supporting the self-cleaning property.

Figure 9. Demonstration of self-cleaning effect on glazed tiles using permanent marker stain: (a) 0 h and (b) after 55 h of sun light irradiation [68].

Considering the experimental parameters, it is concluded that the direct comparison of performance among the various researches is a quite complicate task. Thus, the discussion is limited on the evaluation of the findings proposed in each investigation using MB solutions, as summarized in Table 4.

Table 4. Degradation of methylene blue solutions with PC ceramic tiles.

Ref.	Procedure and effects on MB degradation
Tezza, 2015 [80]	Glazed ceramic tiles were obtained after mixing TiO_2 with two commercial ceramic frits. Thus, the mixed glazes were sprayed on ceramic tiles and sintered at 850-1000 °C. A very low degradation of MB was achieved after 5 h of exposition to UV light. The main reasons were the TiO_2 particles surrounded by the melted frits, not being exposed to the surface of the tiles and large particle size after sintering.
Sciancalepore, 2015 [83]	Mixing of silica/titania (ratio 95/5 wt%) on glazed (average roughness, R_a, 5.5 µm) and matt (R_a, 42.8 µm) porcelain stoneware tiles and heated up at 100, 200, 400 and 600 °C for 5 min. Degradation of MB was higher in all glazed tiles (smaller

	roughness) and it decreased as the temperature increased. After a PEI III test, the photocatalytic activity ability decreased ~75% on glazed tiles and ~50% for matt porcelain stoneware.
Ke, 2014 [74]	$TiO_2/ZnTiO_3$ prepared by sol-gel technique was coated on glazed ceramic tiles. The degradation of MB of anatase $TiO_2/ZnTiO_3$ was higher than anatase TiO_2 and rutile $TiO_2/ZnTiO_3$. Smaller crystalline size and higher surface area was achieved for doped samples.
Ducman, 2013 [69]	TiO_2 suspensions (1% and 4%) were prepared in isopropanol and deposited on the ceramic tiles by spraying. Drying at 100 °C and firing up to 700 -850 °C. All tiles fired up to 850 °C presented a very low activity. The sample just dried at 100 °C and those fired up to 700 °C presented similar activity. The lower activity was found for samples sintered at 850 °C attributed to the ART and grain growth.
Petrovic, 2012 [79]	Ceramic tiles coated by TiO_2 suspensions (4.5, 1, 0.5 and 0.1 wt%) and fired up to 700 °C for 30 min. Degradation of MB was higher for samples coated with 4.5 wt% TiO_2. For those coated with 0.1 and 0.5 wt%, degradation was very low. Difference in performance was attributed to the TiO_2 concentration on the surface.

3.5.1.2 Orange II

TiO_2 coated ceramic tiles for photocatalytic decomposition of Orange II have been applied in water remediation [72, 73, 84]. The idea was sustained by the use of ceramic tiles as a material for degradation of the dye, instead of using suspended powder.

From the practical point of view, catalysts suspended in slurry have to be filtered afterwards. This filtration process is sometimes a difficult task, and particles can be lost along the way. This extra process is avoided when a PC ceramic tile is employed. After the degradation of the dye, just a simple rinse is needed and the tiles are ready to get back on work. A summary of the main findings in the literature about degradation of orange II solutions by PC ceramic tiles is shown in Table 5.

Table 5. Degradation of Orange II solutions with PC ceramic tiles.

Ref.	Procedure and effects on Orange II degradation
Seabra, 2011 [73]	Degradation of Orange II for four commercial TiO_2 powders: Kronos, P25, QCH and QCr. When they were used in suspension, P25 has presented the best performance, while QCr has not presented any degradation at all, which was directly attributed to the grain size. After applying the powders on the ceramic tiles and sintering at 950 °C, Kronos has shown the best results due to the postponing of ART.
Rego, 2009 [84]	Photocatalytic degradation of Orange II comparing TiO_2 and ZnO coated ceramic tiles under sunlight irradiation. The films were made by screen-printing and firing up to 850 °C. TiO_2 coating achieved ~90% degradation after 10 h and ZnO coating, 83% after 12 h. For degradation with different solution pH, the natural pH of the dye suspension (~7.6) had a better performance.
Ruiz, 2009 [85]	Photocatalytic activity comparing 10 different glazes, ZrO_2 frit and a TiO_2 glaze (0.2-4.0% TiO_2). Three glazes presented some activity (anorthite, cassiterite and zircon). ZrO_2 frits (2.5-12% ZrO_2) presented higher activity at higher ZrO_2 percentage. TiO_2 glaze (4%) sintered at 790 °C had photo-degradation similar to P25.
Marcos, 2008 [72]	TiO_2 layers (Kronos) were deposited by screen-printing on glazed ceramic tiles (25 and 50 g/m² TiO_2 layers). Photo-degradation of Orange II was evaluated under visible light. The annealing temperatures were from 300-1100 °C. The tiles fired at 1100 °C did not presented any photocatalytic activity. Best rate constant was achieved at 950 °C with 50 g/m² of TiO_2 (0.056 min^{-1}).

3.5.2 Superhydrophilicity

Superhydrophilicity (water contact angle <5°) is another distinct photo-induced phenomenon of TiO_2. The electrons tend to reduce the Ti^{4+} cations to the Ti^{3+} state, and the holes oxidize the O^{2-} anions. In this process, oxygen atoms are ejected, and then oxygen vacancies are created. Subsequently, the water molecules can occupy these oxygen vacancies, producing adsorbed OH groups, which tend to make the surface hydrophilic [20].

This experiment has become an important and popular photocatalytic test for ceramic tiles [70, 77, 80-83]. Practical

applications of superhydrophilic technology involve properties as self-cleaning and anti-fogging.

A standard test method for self-cleaning performance of semiconducting photocatalytic materials can be carried out by measuring the water contact angle according to ISO 27448 [95]. The test method is directed for bulk photocatalysts or photocatalytic coatings, which are usually made from semiconducting metal oxides such as titanium dioxide [95].

Superhydrophilicity is time dependent, which can vary from less than 10 min [81, 82] to over 2 h [70, 77]. However, ISO 27448 also specifies the use of an organic substance (oleic acid) on the surface of the active ceramic as a pretreatment to evaluate the self-cleaning performance. The test simultaneously evaluates the decomposition of the organic substance and the hydrophilic property. In this case, it takes longer to achieve a very low water contact angle because of the organic decomposition. Considering a PC ceramic tile, the water contact angle increases when the oleic acid is applied on the surface of the ceramic. Then, as the organic is decomposed, the hydrophilic property takes place, but to reach the hydrophilic water contact angle in this process it can take over 50 h [83].

The roughness of the sample influences directly on the water contact angle before and after UV-radiation. A lower roughness provides a lower water contact angle on the surface of the ceramic tiles [77]. This is also evident when the water contact angle is measured before irradiation in different annealing temperatures, e.g. 400-1000 °C. The higher is the temperature, the lower is the roughness and the lower is the contact angle [70].

Even though rutile is normally not photocatalytic active, some evidences show that it can present the superhydrophilicity. [20].

3.5.3 Antibacterial activity

PC ceramic tiles can be very employed in hospitals, schools, and restaurants due to the antibacterial activity, since fungi and bacteria may harm the human health. However, new PC ceramic tiles usually are focused on photocatalytic activity and self-cleaning properties. As a result, this relevant characteristic is rarely investigated in the literature. This is also attributed to the need of specific tests, which are usually not available in the ceramic tiles laboratories.

The Japanese Standard JIS Z 2801:2010 [96], specifies a test for antibacterial activity and efficacy to bacteria on the surface of

antibacterial products. Two type of bacteria are described, *Staphylococcus aureus* and *Escherichia coli*. A number of parameters must be followed in order to make a reliable test. [96]

Antibacterial activity is the value that shows the difference in logarithmic values of number of viable bacteria between the antibacterial products and the untreated product after inoculation followed by incubation of bacteria [96]. Ag-TiO_2 coated glazed ceramic tiles have been studied and higher performance has been observed in comparison to pure TiO_2 coating [71, 82]. Even without UV irradiation, Ag with TiO_2 can reduce up to 100% of the bacterial colonies. Two theories attribute the performance to the presence of Ag. One supports that metal silver can react with water and release silver ions, and silver ions combine with sulphydryl in bacteria, resulting in the blocking of breathing and finally the death of the bacteria. The other one says that silver can react with the oxygen dissolved in water and generate activated oxygen $O\cdot$ that can decompose the bacteria [71].

3.6 Characterizations

The development of a PC ceramic tile involves a number of analyses that give important information, which are essential to understand and evaluate the photo activity. Scanning Electron Microscopy (SEM) is present in most papers (Fig. 10), giving valuable evidence about the material performance. Usually, for TiO_2 coated ceramic tiles, SEM is used to analyze the microstructure, grain sizes, thickness and shape of the particles and coatings. At the surface microstructure it is also possible to observe whether or not the TiO_2 particles are covered with glass [69, 80], which will make the surface less photoactive.

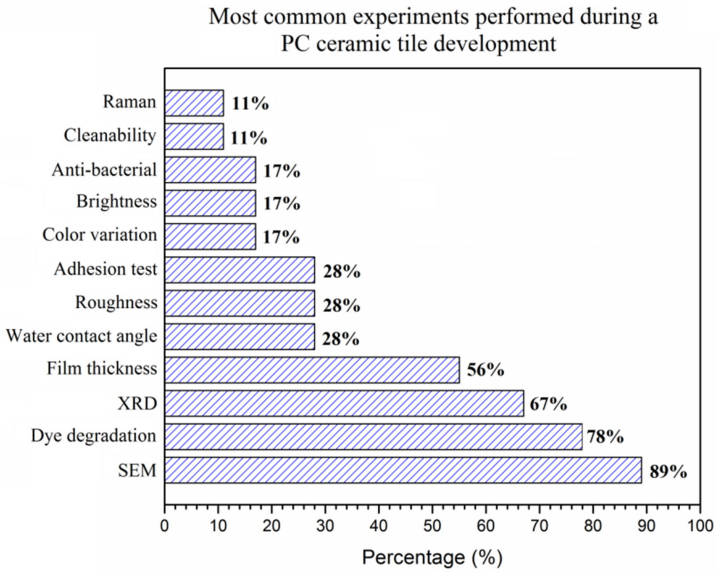

Figure 10. The most common experiments performed during a PC ceramic tile development. The bars mean the frequency the experiments appeared in the papers up to date.

Dye degradation is the second more common analysis, followed by X-ray diffraction (XRD) and film thickness measurement. Both X-ray diffraction and Raman are used to identify the crystalline phase, which are of crucial importance in the photocatalytic field.

3.7 Summary and future challenges

Photocatalytic ceramic tiles have been manufactured and commercialized around the world. However, the optimal processing conditions are still a challenge, even from the performance point of view, as from the production costs. In terms of process, some choices have to be made when the production of those materials starts.

Spraying is the most popular application method used. The thin film obtained by this technique allows the use of TiO_2 nanoparticles efficiently, increasing the PC performance due to the higher surface area achieved. The sintering temperature also plays an important

hole on the development of PC ceramic tiles. A traditional ceramic tile has sintering temperature around 1150-1200 °C. However, if the TiO_2 is sintered at those temperatures the anatase to rutile phase transition will take place, as well as the coarsening and the material will not be photoactive anymore. Alternatively, a second fire has been applied, with usual temperature varying from 600-900 °C, which is the range where the anatase phase is preserved and high crystallinity is achieved, consequently higher PC performance. The extra sintering process involves a change in logistics and increases the production costs. This extra cost will be worth if the value of the new material is marketed correctly, and it will be sustainable if a long term performance is guaranteed.

The performance along the years depends firstly to the maintenance of TiO_2 on the surface of the material. This is related with the adhesion of TiO_2 films, as well as the place where the material is installed. The adhesion can be tested by scratching test, tape test and brushing abrasion. The durability of TiO_2 coating ceramic tiles also can be evaluated by artificial weathering of coatings on glass for building in outdoor and indoor applications. However, just few researchers have tested those characteristics in their ceramics.

Characteristics, as color, brightness, roughness and cleanability of a PC ceramic tile coated with TiO_2 in most of the cases are not affected. However, there are still some variable that can affect them, e.g., Ag-doped-TiO_2 slightly changes the ceramic surface color. The use of screen-printing as application method can influence the roughness and the visible aspects. Moreover, brightness can be affected by the amount of TiO_2 deposited and temperature.

The most common test used to evaluate the photoactivity is the degradation of methylene blue. Even though there are international standards available, as ISO 10678 and JIS R 1703-2, the experimental parameters from one research to another may be different, so the PC performance comparison becomes difficult.

Nanoparticles made possible the use of very small amounts of TiO_2 with improved performance. However, manufacturing a photocatalytic ceramic tile with a single fire, is still not possible. The lack of parameters to specify the service life according to the area installed and the practical relationship of the dye degradation with the self-cleaning property are also questions that remain unanswered.

4. PRIMARY METHODS AND TECHNIQUES

This chapter outlines general aspects of the main techniques and equipment used throughout this work. Details are provided at the respective chapter.

4.1 Synthesis of TiO_2 nanoparticles

Throughout the thesis, three syntheses methods have been used to produce TiO_2 nanoparticles. Those methods were hydrothermal, co-precipitation and sol gel.

4.1.1 Hydrothermal method

Hydrothermal synthesis usually refers to heterogeneous reactions in aqueous media above 100 °C and 1 bar. The method was introduced into modern solid state research after 1945. The interest was centered on the growth of pure crystals of sufficient size, which could present interesting physical properties. The use of autoclaves, which serve as protection for the reaction vessel is required to withstand the pressure applied during the synthesis. From the standpoint of behavior towards corrosion, Teflon is the ideal container material. Thus, the entire autoclave with all reactants, including the joint, is placed within the oven, which can be operated with temperature gradients as well as isothermally [97].

The chemicals used to produce TiO_2 nanoparticles via hydrothermal method in this work were based on Liu *et al.*'s work [98]. Titanium butoxide (10 mL), butanol (60 mL), acetone (10 mL) and acetic acid (10 mL) were first mixed. Then, a mixture of butanol (40 mL) and distilled water (3 mL) was added to the former solution. The new solution was mixed for 1 h and transferred to an autoclave for hydrothermal process at 240 °C for 6 h. For Nb_2O_5-doped-TiO_2, niobium butoxide was used as precursor.

4.1.2 Co-precipitation

Precipitation is a nucleation and growth process with controlled kinetics. High nucleation and slow growth rates are usually required to keep the particle powders small. The solubility of the desired cations dissolved in an aqueous solution in the precipitation technique is exceeded by evaporation of the liquid or by adding a

chemical precipitant agent. Then, the precipitation of metal hydroxides is promoted. The control of nucleation and growth mechanisms and consequently of the particles morphology can be achieved with the modification of pH and temperature of the solution [99].

The method has been used to synthesize various common ceramics nanoparticles, as NiO [100], TiO_2 [101], ZnO [102], and $ZnAl_2O_4$ [103]. Usually, a stoichiometric amount of the desired metal nitrate is dissolved in distilled water and slowly dripped into ammonia. Titanium (IV) isopropoxide (TTIP) was used as Ti precursor, being slowly dripped into an ammonium hydroxide solution (NH_4OH, 5M) under vigorous stirring. For Nb_2O_5-doped-TiO_2, niobium butoxide (NB) was used as precursor. Then, TTIP and NB were mixed for 10 min in the desired stoichiometric ratio and dripped into the ammonium hydroxide solution.

An amount in excess of ammonia was used in order to keep the pH difference with the metal ion solution. This helps driving nucleation of the smallest hydroxide particles, which become oxide nanoparticles. The solution turns an opaque slurry as the metal hydroxide precipitates. Afterwards, the colloidal suspension is centrifuged to separate the nanoparticles from the liquid. Then, it is washed out with distilled water and ethanol to remove any residual ammonia from the hydroxide's surface. The powders are dried and then ground with pestle and mortar. The final process to obtain the oxide is the calcination at the appropriate crystallization temperature.

4.1.3 Sol-gel technique

The sol-gel is one of the most used methods to produce TiO_2 thin films due to its cost effectiveness, homogeneity, and reliability. In a typical process, a colloidal suspension (a sol) is formed from the hydrolysis and polycondensation reactions of the precursors, which are usually metal salts. Then, the prepared sol is deposited on the substrate, following the polymerization and eventual loss of solvent. Hence, the liquid sol is transformed into a solid gel phase [104].

The technique has been used to produce pure TiO_2 films, as well doped-TiO_2 [105]. In this thesis, the sol was made with the optimized 1:5:0.3 volume percentage titanium (IV) isopropoxide (TTIP), ethanol and diethanolamine [68]. For Nb_2O_5-doped-TiO_2, niobium butoxide (NB) was used as Nb precursor. TTIP and NB

were mixed at the stoichiometric amount desired and stirred for 10 min. Then, the mixture was dripped slowly into the ethanol/diethanolamine solution. Afterwards, the solution was stirred for 2 h at room temperature to enhance the reaction rate between diethanolamine and TTIP.

This synthesis was intended to form a thin TiO_2 film on ceramic tiles. In this way, the produced sol was dissolved again in ethanol (50 wt%) to reduce the viscosity and applied by spraying on the tiles.

4.2 Powders characterization

The main techniques used were thermal gravimetric analysis (TG), differential scanning calorimetry (DSC), X-ray diffraction (XRD), specific surface area by BET, scanning electron microscopy (SEM) and transmission electron microscopy (TEM).

4.2.1 Thermal gravimetric analysis and differential scanning calorimetry

Thermal gravimetric analysis (TG) is a technique in which the mass of a substance is measured as a function of temperature while the substance is subjected to a controlled temperature program. The most suitable methods for quantitative determination are measurements based on mass-changes in the course of decomposition (possibly oxidation and reduction) processes [106]. This method is usually applied simultaneously with differential scanning calorimetry (DSC) or differential thermal analysis (DTA).

DSC and DTA are thermal analyses that measure how physical properties of a sample change along with temperature against time. In both techniques, two crucibles are heated in the measurement chamber. One contains the material being investigated and another one is typically empty, which is used as reference.

In the case of DSC, the instruments most used are the heat flux DSC and the power compensated DSC. In the heat flux DSC system the sample and reference are heated at the same rate from a single heating source. Then, the temperature difference between the crucibles is recorded and converted to a power difference, which gives the difference in heat flow. In the power compensated DSC, the sample and the reference are heated separately. The sample and reference are maintained at the same temperature, and the difference

in thermal power required to maintain them at the same temperature is measured and plotted as a function of temperature or time [107].

4.2.2 X-ray diffraction

X-ray diffraction is a widely used technique for characterizing crystalline materials. From the XRD measurements information can be extract such as crystalline phases, lattice strain, lattice parameters and dislocation densities. X-rays are a form of electromagnetic radiation that has high energies and short wavelengths, which are in the order of the atomic spacings for solids. The sample is bombarded by X-rays of a certain wavelength, λ, at an incident angle, θ. The X-rays can either pass directly through the crystal or, depending on the angle of incidence, interact with certain atoms in the lattice. The interaction makes the X-rays to be scattered at every atomic location [108, 109].

When the atoms are regularly spaced in a crystalline lattice and the incident radiation has the wavelength in order of this spacing, a constructive interference will occur for some angles and a destructive interference for others. The constructive interference amplifies the signal and the destructive cancels each other out. Thus, the constructive interference is represented by large peaks on a XRD pattern. This phenomenon is governed by the Bragg's law, which is represented by Eq. 6 and Fig. 11.

$$n\lambda = 2d \sin\theta \tag{6}$$

where n is the order of reflection, which may be any integer (1, 2, 3,…) consistent with sin θ not exceeding unity and d is the parallel crystal lattice spacing.

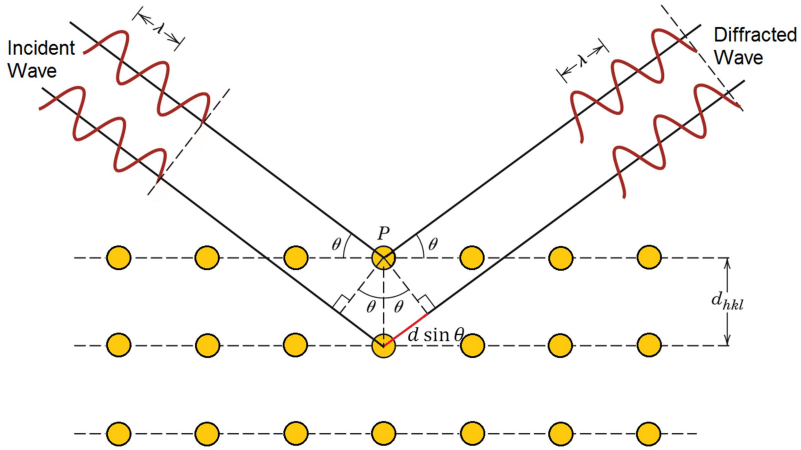

Figure 11. Schematic illustration of Bragg's law of incident electromagnetic wave of wavelength λ within a material with parallel crystal lattice spacing *d*. (Adapted from [108]).

From the XRD data can be calculated the crystallite size using the Scherrer formula, Eq. 7.

$$L = \frac{K\lambda}{\beta \cos\theta} \tag{7}$$

The Scherrer formula was developed in 1918, to calculate the crystallite size (L) by XRD radiation of wavelength λ (nm) from measuring full width at half maximum of peaks (β) in radian located at any 2θ in the pattern. Shape factor of K can be 0.62-2.08 and is usually taken as about 0.89. As the particle becomes smaller, the width of the diffraction peak increases. This is generated by nanocrystals deviating from that of a perfect crystal extending infinitely in all directions. However, broadening is just significant when the crystals are below 100 nm, which is one limitation to the technique [110].

4.2.3 Specific surface area

The specific surface area of the powders in this work was measured using the Brunauer, Emmett and Teller (BET) method, based on the physical adsorption of gases [111]. The amount of gas

adsorbed depends on the exposed surface and also on the temperature, gas pressure and strength of interaction between the gas and solid. In this thesis, nitrogen was used, due to the high purity and strong interaction with most solids.

Before performing the test, a pretreatment was carried out to remove any gas and vapor that was physically adsorbed on the sample surface. In this work, the pretreatment was performed by heating the samples under vacuum at 400 °C for 12 h. Previous experiments using XRD diffraction before and after the pretreatment have shown no changes in phase composition and crystallite sizes of the samples.

During the experiment, the sample has to be cooled using liquid N_2 in order to obtain detectable amounts of adsorption. This is necessary because of the weak interaction between gaseous and solid phases. Then, a known amount of nitrogen gas is released stepwise in the sample cell. Hence, by creating conditions of partial vacuum, relative pressures lower than the atmospheric pressure are achieved. When the saturation pressure is reached, no more adsorption occurs. After the adsorption layers are formed, the sample is removed from the nitrogen atmosphere and heated to cause the adsorbed nitrogen to be released from the material and quantified. The data collected is displayed in the form of a BET isotherm, which plots the amount of gas adsorbed as a function of the relative pressure.

4.2.4 Electron microscopy

Electron microscopy (EM) can be defined as a specialized field of science that employs the electron microscope as a tool and uses a beam of electrons to form an image of a specimen. The advantage of the electron microscopes in comparison with optical microscopes is the much shorter wavelength of the electron (e.g., $\lambda = 0.005$ nm at an accelerating voltage of 50 kV) when compared to the wavelengths of visible light ($\lambda = 400$ nm to 700 nm). Thus, if the voltage is accelerated in EM, the wavelength decreases and the resolution increases [112].

There are two basic types of electron microscopy, scanning electron microscopy (SEM) and transmission electron microscopy (TEM). They differ fundamentally in their principles and applications. The SEM generates an image with the help of secondary electrons that gives the viewer the impression of three

dimensions, while the transmission electron microscope projects electrons through an ultrathin slice of the specimen and produces a two-dimensional image. Depending on the instrument used, specimens can be magnified roughly between 10 and 100,000 times in SEM and between 500 to 500,000 times for TEM [112].

In this thesis, SEM was employed to analyze microstructure and thickness of TiO_2 coatings, while TEM was used in powder specimens to observe surface morphology and particle size distribution.

4.3 Thermodynamics studies

The thermodynamics studies performed in this thesis were related to the surface energy, calculated by water adsorption and enthalpy of drop solution, determined by high temperature oxide melt solution calorimetry (HSC).

4.3.1 Water adsorption

Water adsorption microcalorimetry is based on the thermodynamics of water adsorption on an anhydrous ceramic surface. The aim of the experiment is to measure the heat of adsorption of water molecules on the surface of an oxide as a function of the relative pressures. In this work, an ASAP 2020 sorption system connected to a Calvet-type microcalorimeter (Setaram DSC-111) was used (See Fig. 12). Firstly, the sample is heated up to remove all water from the surface. The temperature and time required is determined by thermogravimetry. Then, the sample is cooled down to room temperature, and microdoses of water (~2 μmol) are injected by the dosimeter in the analysis chamber. The system re-establishes equilibrium by adsorbing water on the sample. The pressure after the equilibrium is the same in the reference side and in the sample side of the fork. ASAP 2020 measures the pressure and water coverage after the system reaches the equilibrium. At the same time, the DSC microcalorimeter measures the energetics of the adsorption step and reports the difference between the right (sample) and left (reference) forks. Then, another dose of water is introduced in the system from ASAP 2020. Water vapor again adsorbs onto the specimen to re-establish equilibrium. The dosing repeats until the desired relative pressure is reached [5, 113, 114].

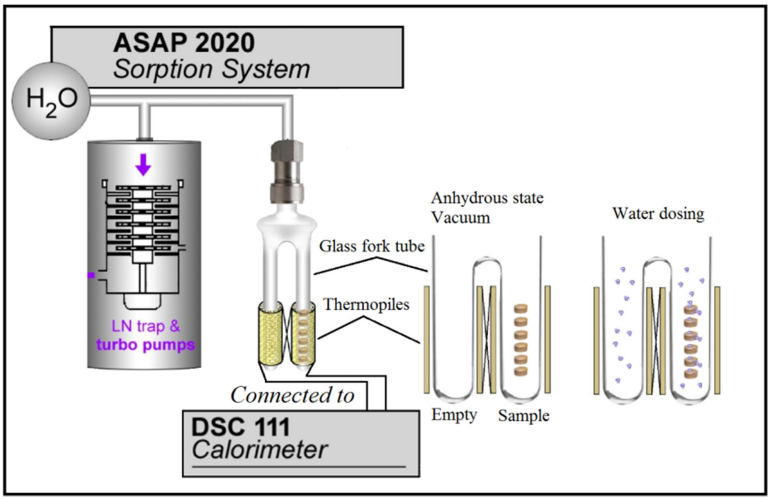

Figure 12. Schematic representation of water adsorption experiment. (adapted from [113, 114]).

The water adsorption on the anhydrous surface takes place in three distinct stages: (1) the first molecules adsorb on the surface in a dissociative manner, where the adsorption enthalpies are considerably more exothermic than liquid water; (2) this is followed by the adsorption of molecules that are still affected by the surface chemistry, but weakly; (3) at certain coverage, the water builds up enough monolayers that the outermost water adsorbed will not suffer interaction from the solid surface anymore. Thus, the enthalpy of water adsorption will be equal to that of liquid water (-44 kJ/mol) and the surface energy is known to be 0.072 J/m² [5, 113].

Castro and Quach [114] suggested that if a water adsorption experiment is performed in a closed system, the surface energy will change according to Eq. 8.

$$\gamma_2 = \gamma_1 + \theta \times \Delta H_{ads} \quad (8)$$

where θ is the surface coverage, ΔH_{ads} is the measured heat of adsorption, and γ_1 and γ_2 are the surface energies before and after the given adsorption coverage takes place, respectively. The

equation establishes a relationship between the surface energies at different water coverage. Therefore, from Eq. 8 the surface energy can be calculated at any water coverage if both adsorbed amount and heat of adsorption are known.

In this work, the surface energy of the specimen was calculated using the second order surface energy differential equation proposed by Drazin and Castro [113]. The equations were solved numerically using a custom written program (MATLAB 2010a) after inserting fitted experimental data from both water adsorption quantity and associated heat of adsorption. Details about the method are shown in Chapter 5.

4.3.2 High temperature oxide melt solution calorimetry (HSC)

High temperature solution calorimeters are very accurate instruments capable of assessing the heat of high temperature dissolution of samples dropped from a room temperature condition into the hot molten solvent [5]. In this work, a custom-built instrument that operates at 800 °C was used, which is located in the Peter A. Rock Thermochemistry Laboratory at UC Davis. A schematic representation of the calorimeter used is shown in Fig. 13.

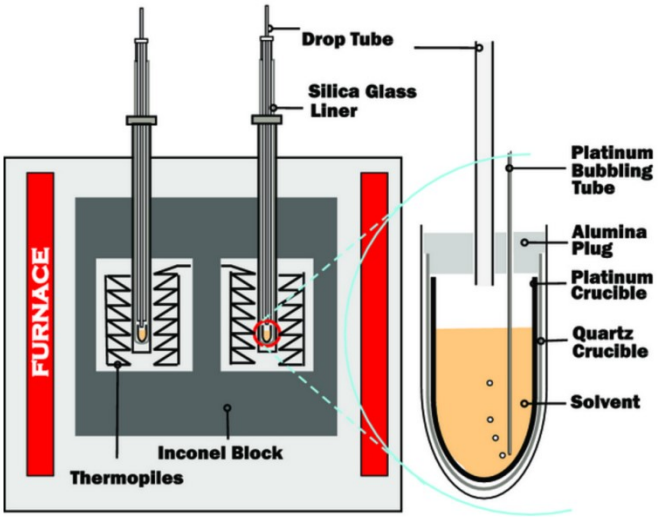

Figure 13. Schematic representation of high-temperature twin Calvet calorimeter and assembly for drop solution calorimetry in a molten oxide solvent. (adapted from [115]).

The four basic components are: an Inconel cylinder, the electrical furnace elements, a case with insulation, and two thermopiles. Basically, the Inconel cylinder is the thermal ballast that stabilizes the temperature of the system. The Inconel block is surrounded by a cylindrical electric furnace that is the main source of heating. The case and insulation surrounding the furnace control the heat flow from the calorimeter. Inside the Inconel block there are two thermopiles, each one is composed of 6 star shaped assembles of eight thermocouples wired in series. The Pt crucibles, where the solvents will dissolve the samples are set up in the center of the thermopile. Moreover, there are Inconel protection tubes to separate the thermopiles from the glassware and provide an extra protection from solvent leaks in the calorimeter.

The samples were carefully prepared to avoid any residues from the synthesis. The presence of impurities can compromise the data; for instance, carbonates can combust during dissolution at high temperature and the heat can overcome the small interface energy contributions. To make sure that the samples were clean, mass spectroscopy was performed in all samples and no carbon residue was detected. The pristine samples were then hand pressed and the pellets (~5 mg) were dropped into molten sodium molybdate ($3Na_2O.4MoO_3$) solvent. During the reaction, the thermopile tracks changes in temperature between points in the calorimeter chamber and points in the Inconel block. The signal is proportional to the temperature difference at each of the spots that the thermocouples connect, and therefore the rate of heat flow is proportional to this microvolt signal. The total heat effect seen is proportional to the rate of heat flow integrated over time, *i.e.,* the area under the calorimetric peak [116]. The units of the integrated area are arbitrary units (also called counts) which can be converted into units of heat (joules) with suitable calibration procedures.

Special care during the experimental procedure will guarantee the constancy of the results. The use of gas bubbling through the calorimetric solvent, for instance, stirs the melt, enhancing dissolution and oxidation rates, dispersing the solute particles in the melt, and preventing local saturation [115]. Flushing a continuous gas on the head space above the crucible is also an important routine; it helps to maintain the gas composition constant. In this thesis was used oxygen gas. Changes in the composition of the gas above the solvent can change the heat flow characteristics of the

calorimeter during an experiment and cause significant shifts in the baseline. Furthermore, the calorimeter has tubes that communicate its interior with outside in order to introduce samples. This makes the calorimeter sensitive to its surroundings. So, the calorimetry room has special air conditioning and humidity control.

4.4 Photocatalytic studies

The effect of photocatalysis is not easily inspected visually, and no appropriate and official evaluation methods have been proposed. Furthermore, diverse functions of photocatalysts cannot be evaluated with a single method; so, different evaluation methods are provided for self-cleaning, water decontamination, air purification and anti-bacterial actions, respectively [95].

This work has focused on the self-cleaning property of TiO_2 coated ceramic tiles. As mentioned in Chapter 2, the self-cleaning property can be evaluated by two experiments, which are degradation of dye and superhydrophilic property. In order to attend this requirement, the degradation of methylene blue dye was performed and the superhydrophilicity was evaluated by measuring the water contact angle under UV-light.

The MB degradation in this thesis was evaluated using TiO_2 powders dispersed in a MB solution and also using TiO_2 coated glazed ceramic tiles as a photocatalyst. Details about the powders characterization, as the catalysts concentration in the slurry can be found in Chapter 6. In addition, the procedure for the MB degradation on coated ceramic tiles is described in details in Chapter 7.

The international standard ISO 10678:2010 was used as a guide [93]. The standard describes the method for the determination of the photocatalytic activity of surfaces by degradation of the MB dye molecule in aqueous solution using ultraviolet (UV) radiation. The principle is to degrade the MB molecules that are in contact with the potentially photocatalytically active surface, with the overall result being the discoloration of the solution. The UV/visible spectroscopy determines the amount of dye remaining in the solution at regular intervals of the UV radiation. An identical sample was used as the reference without any UV radiation. Then, the final results are expressed in specific degradation rates and the respective photonic efficiencies characteristic of the surface tested.

The superhydrophilic property was evaluated by measuring the water contact angle on the treated surface before and after UV radiation. The measurements in this case were performed following ISO 27448 [95]. When a tangent line is drawn from the contact point of the solid, liquid and vapor phases (normally air) along the curve of the liquid on the solid, the angle between the line and the solid surface is referred to as the contact angle θ (Fig. 14).

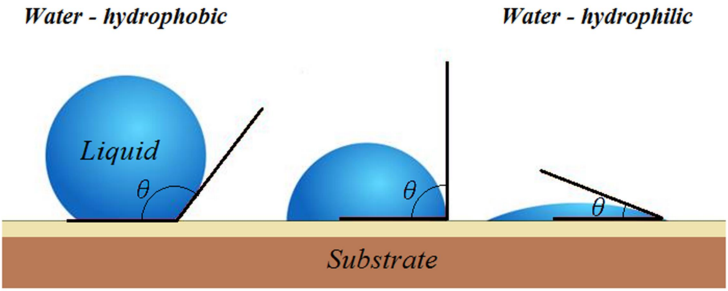

Figure 14. Surface wetting types.

The water contact angle was measured using 1 μL water droplet deposited direct on the coated surface. The time among the measurements was decided depending to the sample (5-15 min) and the measurement was stopped when θ <5°.

5. SURFACE ENERGY EFFECTS ON THE STABILITY OF ANATASE AND RUTILE NANOCRYSTALS: A PREDICTIVE DIAGRAM FOR Nb_2O_5-DOPED-TiO_2[2]

In this Chapter, a set of thermodynamic data was collected in order to build a new predictive nanoscale phase diagram for Nb_2O_5-doped TiO_2. Water adsorption microcalorimetry and high temperature oxide melt solution were used to obtain the surface and bulk enthalpies.

5.1 Introduction

Titanium dioxide presents three main polymorphs: anatase, rutile and brookite. All three polymorphs can be readily synthesized in the laboratory and typically, the metastable anatase and brookite will transform into the thermodynamically stable rutile upon calcination at temperatures exceeding 600 °C [117]. Some studies have been performed on the thermodynamic viewpoint to better understand the stability of the TiO_2 polymorphs [6, 118-122]. Even though rutile is the most stable form of TiO_2 and anatase is known as a metastable phase, at the nanoscale, anatase becomes more stable than rutile [6, 7]. This is related to the competition between surface and bulk energies, leading to a crossover in thermodynamic stability when particle sizes are decreased. Thus, anatase shows a range of particle sizes in which it is thermodynamically stable as long as coarsening is avoided [6].

Several dopants have been studied targeting the control of TiO_2 stability at the nanoscale and its properties. Among them, niobium improves TiO_2 performance for oxygen sensing [123-125], solar cells applications [126, 127], and photocatalysis [44, 57, 128]. When doping TiO_2 with Nb_2O_5, since the ionic radius of Nb^{5+} (0.64 Å) is only slightly larger than Ti^{4+} (0.605 Å), Nb^{5+} forms solid solution in the lattice of TiO_2. One Ti cationic vacancy is then created per every four Nb ions to compensate the excess charge, or a stoichiometric reduction of Ti^{4+} to Ti^{3+} can take place to accommodate it [41]. Atanacio *et al*. [129] have showed that niobium has a potential to segregate on the surface of TiO_2 under oxidizing conditions. The segregation tendency is enhanced by the

[2] Published in Applied Surface Science 393 (2017) 103-109. http://dx.doi.org/10.1016/j.apsusc.2016.09.126.

presence of titanium vacancies, which are formed at the TiO_2/O_2 interface and trapped at the surface.

The use of dopants prone to segregation has been cited as a tool to decrease interface energies in oxides [5, 130-134] and observed to follow Eq. 9:

$$\gamma_S = \gamma_0 + \Gamma_S \Delta H_{seg} \quad (9)$$

where γ_s is the surface energy of the doped material; γ_0 represents the surface energy of undoped material; Γ_s is the solute excess at the surface; and ΔH_{seg} is the enthalpy of segregation. From Eq. 9, one can draw the conclusion that the surface energies decrease with an increase in the surface excess of the dopant, a concept well established for liquids by Gibbs' adsorption isotherm.

If a dopant is changing the surface energy of an oxide with intrinsic polymorphism, the stability of particular phases can be remarkably affected when the surface area is enlarged (smaller grain sizes). As demonstrated for Y and Ca doped zirconia [135, 136], a new phase diagram complementing the conventional temperature-composition diagram must be introduced, with the grain size as a new key variable to account for the surface energetic contribution. Quantitative prediction of the effect of the dopant on the surface energy is therefore of interest to enable phase stability design.

Many methods have been proposed in the literature to measure the surface energy of oxides [5]. Among them, water adsorption microcalorimetry has recently demonstrated potential to accurately assess surface energies of doped systems [114] and was recently explored in TiO_2 based systems [137]. The principle of this technique is the relationship between the heat of adsorption of water molecules on the surface of the oxide and the surface energy itself. An adsorption theory previously described in details enables calculating the surface energy of the anhydrous surface state or at a given hydration condition [113, 114].

In this chapter, surfaces energies of 0 to 2 mol% Nb_2O_5-doped TiO_2 were measured using water adsorption microcalorimetry [113]. The data was combined with oxide melt drop solution enthalpy to deliver reliable thermodynamic information on the bulk energetics of the system and the results used to build a new, predictive nanophase diagram for anatase-rutile in the studied compositional range.

5.2 Experimental Procedure

5.2.1 Sample preparation

TiO_2 containing 0, 0.5, 1, 2 and 5 mol% Nb_2O_5 was synthesized by simultaneous precipitation. The samples are labeled as 0NbTi, 0.5NbTi, 1NbTi, 2NbTi and 5NbTi. The Ti and Nb precursors used were titanium (IV) isopropoxide (TTIP, Aldrich) and niobium butoxide (Aldrich), respectively. TTIP and Nb-butoxide were mixed for 10 min to obtain a homogeneous solution and then dripped into an ammonium hydroxide solution (NH_4OH, 5M, Fisher Scientific) under vigorous stirring. The obtained colloidal suspension was centrifuged at 3000 rpm for 5 min to separate the nanopowders from the liquid and washed three times (in water, water/ethanol 1:1 in volume, and ethanol) to remove any residual ammonia. The samples were dried at 90 °C for 72 h and ground with a pestle and mortar. In order to obtain anatase phase and eliminate any ethanol residual from the powders, the dried hydroxides were calcined in a box furnace (Lindberg/Blue M) under oxygen atmosphere at 450 °C for 7 h. Bulk rutile phases were obtained after calcination in a tube furnace (Thermolyne type 54500) at 1200 °C for 2 h.

5.2.2 Characterization

Powder X-ray Diffraction (XRD) patterns were collected using a Bruker AXD D8 Advance diffractometer using CuKα radiation (λ = 1.5406 Å), operated at 40 kV and 40 mA. Data were collected in the range 20° to 90°. LaB_6 (NIST SRM 660a) was mixed with the samples as a standard for the lattice parameter calculations. The crystallite size was determined by WPF (Whole Pattern Fitting) refinement in the JADE software (version 6.11, 2002, Materials Data Inc., Livermore, CA). Surface area measurements were carried out using the Brunauer, Emmett, and Teller (BET) method with nitrogen gas adsorption (Micromeritics Gemini VII). Thermogravimetry results showed that significant mass changes can only be observed up to 400 °C; hence, this temperature was selected for degassing prior to both BET (Micromeritics VacPrep 061, sample degas system) and water adsorption experiments.

5.2.3 Water adsorption

The water adsorption microcalorimetric experiments were performed using a Micromeritics ASAP 2020 coupled with a Calvet-type microcalorimeter (Sensys Evo, Setaram, France). The objective of the experiment is to measure the heat of adsorption of water molecules on the surface of an oxide as a function of the relative pressures. The instrument and methodology are described in detail elsewhere [113, 114]. The samples were placed in the chamber and degassed (at 400 °C for 12 h) to ensure an initial anhydrous surface condition. Lightly hand pressed pellets with total surface area ~2 m^2 were used (12-24 mg depending of the sample surface area). The chamber was kept at 25 °C, and the dosing routine was programmed to be ~2 µmol H_2O per dose and equilibration time ~1.75 h for the first four doses, ~1 h for the fifth dose, ~0.75 h for sixth and seventh and ~0.5 h from eighth on. A correction for water adsorption on the tube and manifold was made from a blank run (empty tubes).

The anhydrous surfaces energies of the synthesized specimens were calculated using the water adsorption data and computing them using a custom written function (MATLAB Release 2010a, MathWorks, Natick, MA), reported elsewhere [29]. The water adsorption curve was fit using a modified Langmuir-BET adsorption curve (Eq. 10), where the regression Eq. fit the water adsorption data as a function of pressure;

$$\theta = \theta_c \frac{b\sqrt{x}}{1 + b\sqrt{x}} + \theta_p \frac{cx}{(1-x)(1+(c-1)x)} \tag{10}$$

where θ_c is the monolayer coverage of the dissociative water; θ_p is the physisorption monolayer coverage; b and c are unit-less fit parameters that depend on the specimen; and x is the relative pressure (p/p_0). The differential heat of adsorption curve was fitted using the Eq. 11 [29].

$$\frac{dH_R}{d\theta} = De^{-\theta/d} + E(f\theta - \theta^2)e^{-\theta/e} + \left.\frac{dH_{con}}{d\theta}\right|_{T_o, p_o} \tag{11}$$

Eq. 11 is an empirical relationship for the differential heat of water adsorption as a function of the water coverage, where H_R is the heat of adsorption, and H_{con} is the enthalpy of liquefaction of water. The Eq. requires five parameters: d and e are decay parameters that relate how strong the specimen's surface affects the adsorbed water; and D, E, and f are fit parameters with units of kJ/mol, kJ/mol³, and mol, respectively.

After fitting the water adsorption curve and the differential heat of adsorption data using Eqs. (10) and (11), the surfaces energies of the samples were numerically computed by plugging the mentioned equations into Eq. (12).

$$\mathrm{SA}\frac{\mathrm{d}^2\gamma}{\mathrm{d}x^2} = \frac{\mathrm{d}\theta}{\mathrm{d}x}\left\{\frac{\mathrm{d}^2 H_r}{\mathrm{d}\theta^2}\frac{\mathrm{d}\theta}{\mathrm{d}x} + \frac{\mathrm{d}\mu_{gas}}{\mathrm{d}x} - \gamma\frac{\mathrm{d}^2\mathrm{SA}}{\mathrm{d}\theta^2}\frac{\mathrm{d}\theta}{\mathrm{d}x} + \frac{\mathrm{d}\gamma}{\mathrm{d}x}\left(\frac{\mathrm{SA}}{\theta} - 2\frac{\mathrm{dSA}}{\mathrm{d}\theta} + \mathrm{SA}\frac{\mathrm{d}^2\theta}{\mathrm{d}x^2}\left(\frac{\mathrm{d}x}{\mathrm{d}\theta}\right)^2\right)\right\} \quad (12)$$

Eq. (12) correlates the surface energy and water adsorption. The adsorbed water is a function of the pressure, x; and the differential heat of water adsorption is a function of the adsorbed water, θ. In this Equation, SA is the surface area of the sample; γ is the surface energy at a given state; and μ_{gas} is the vapor chemical potential.

5.2.4 Oxide melt solution calorimetry

High-temperature drop solution calorimetry was carried out using a custom-built Calvet-type twin calorimeter [138]. This equipment provides energy of dissolution of oxide samples, which appropriate thermochemical cycles can be used to obtain bulk enthalpy information. Laboratory standard calibration with transposed temperature drops of ~5 mg alpha alumina pellets was used. Hand pressed pellets (~5 mg) were weighted using microbalance and dropped into molten sodium molybdate ($3Na_2O.4MoO_3$) solvent at ~800 °C in the calorimeter. Oxygen was bubbled through the solvent at the rate of 3.3 mL/min to facilitate sample dissolution. Oxygen was also flushed over the solvent in the calorimeter (50 mL/min) to maintain constant composition for the gas phase over solvent. Changes in the composition of the gas above the solvent can change the heat flow characteristics of the calorimeter during an experiment. Before dropping the samples in the calorimeter, the powders were left in the calorimetric suite for at least 3 days to equilibrate in a 50% relative humidity environment. Several drops

were made to obtain statistics. The error reported was determined by the standard deviations. Thermogravimetry was used to measure the water content on the samples at degassing conditions to enable a quantitative thermochemical cycle.

5.3 Results and Discussion

5.3.1 Nanoparticles' characterization

The X-ray diffraction patterns for pure TiO_2 and Nb_2O_5-doped TiO_2 samples are shown in Fig. 15. The pure (undoped) anatase phase (JCPDS card n. 71-1167) used in the experiments is shown in Fig. 15a. Broad peaks can be observed, which is typical of nanosized crystallites. No second phase was detected by XRD, so that only the peaks referred to the anatase phase are indicated. The absence of niobium oxide phases suggests that niobium is dissolved into TiO_2 or segregated on the surface of titania nanoparticles. The powders referring to the rutile phase were calcined at 1200 °C for 2 h and are shown in Fig. 15b. The polymorph is referenced using JCPDS card n.86-0147. Sharp peaks are observed, which is common in bulk samples. Notice that the diffraction pattern for 5 mol% Nb_2O_5-doped TiO_2 is not shown at Fig. 15b. This sample has presented titanium niobium oxide phase ($TiNb_2O_7$ – monoclinic, JCPDS card n. 39-1407) in addition to rutile [129]. Thus, the energetic studies, which requires single phase were not carried out for this sample. No second phase was detected for 0-2 mol% Nb_2O_5-doped-TiO_2 rutile. All peaks match with TiO_2 rutile phase.

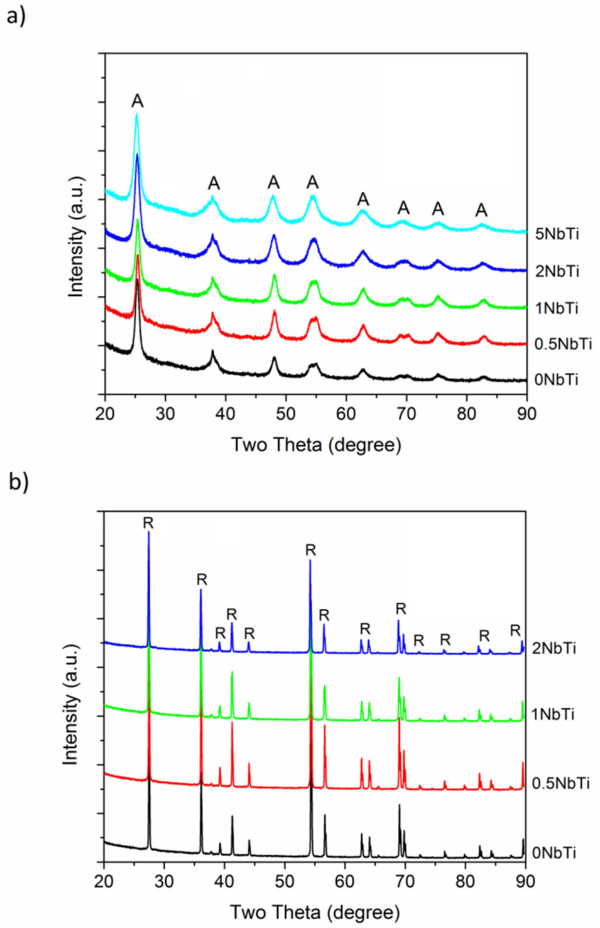

Figure 15. XRD patterns of Nb_2O_5-doped TiO_2. a) Anatase (0-5 mol% calcined at 450 °C for 7 h), and b) Rutile (0-2 mol% calcined at 1200 °C for 2 h).

The results for lattice parameters a, b and c for both anatase and rutile phases are shown in Table 6. A systematic expansion is observed in the lattice parameters with increasing of Nb_2O_5 doping. As the ionic radius of the Nb^{5+} ions into octahedral coordination is larger than Ti^{4+}, the increase in the cell parameters with the increasing Nb content confirms that Nb is incorporated in the TiO_2 lattice. This trend is in agreement with the results found in the literature [41, 119]. The lattice parameter ratio (c/a) for anatase and

rutile phases is shown in Fig. 16. Both phases have similar trend. Up to 2 mol% Nb_2O_5 doping, a systematic decreasing on the c/a ratio is observed, and for 5 mol% the value is statistically the same as 2 mol% Nb_2O_5-doping. The ratio decreasing with the increasing of Nb_2O_5 concentration suggests the formation of limited solid solution. For this work this limit was achieved at 2 mol% Nb_2O_5-doping. Thus, this value was used as doping limit for surface energies and enthalpy of drop solution measurements. Consequently, it was the doping limit for the phase diagram as well. According to Vegard's law [139], a linear dependence of lattice parameter on dopant concentration is expected when all dopant content is dissolved in solid solution. The deviation from linearity proposes the occurrence of surface segregation [130].

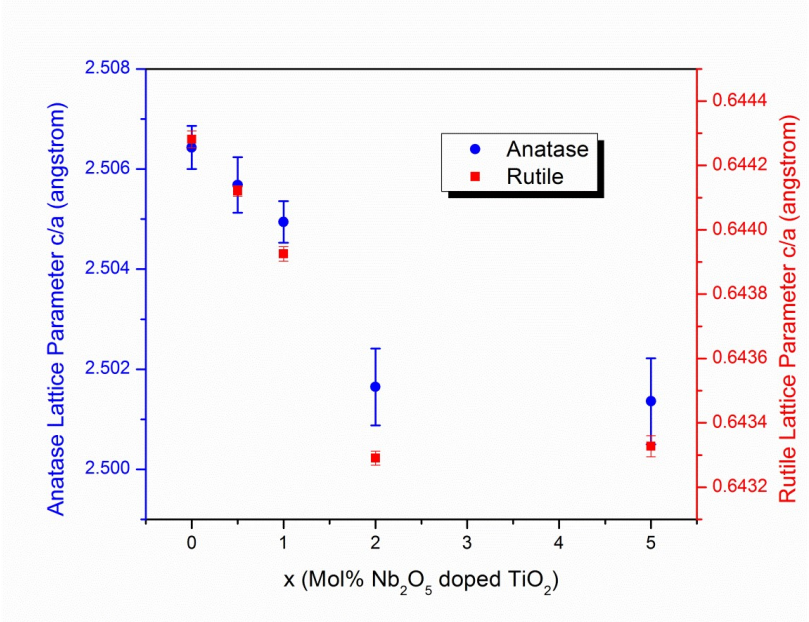

Figure 16. The lattice parameter ratio (c/a) for 0-5 mol% Nb_2O_5-doped-TiO_2 samples for anatase and rutile phases.

The crystallite sizes calculated from WPF refinement for all samples are also shown in Table 6. For anatase phase it is possible to observe a systematic decreasing in the grain sizes as the doping content increases. As all anatase samples were calcined at the same temperature and time, the decrease on the grain sizes can be

attributed to Nb_2O_5-doping content, which suggests an increase in the stability of TiO_2 nanoparticles against coarsening. According to coarsening models [140], the particle size is directly proportional to the surface energy, then it is expect that lower surface energy promotes smaller particle sizes at a given temperature. The grain sizes for rutile phases are >100 nm, so the WPF refinement cannot give a reliable result for grain size.

Table 6. Crystallite sizes and lattice parameters calculated using a WPF Refinement in JADE 6 Software.

Sample	*Grain size (nm)*	*Lattice Parameter a=b (Å)*	*Lattice Parameter c (Å)*
0NbTi (Anatase)	11.8±0.3	3.7873±0.0003	9.4926±0.0010
0.5NbTi (Anatase)	9.6±0.3	3.7887±0.0003	9.4932±0.0013
1NbTi (Anatase)	8.4±0.2	3.7902±0.0003	9.4943±0.0010
2NbTi (Anatase)	6.8±0.2	3.7942±0.0004	9.4918±0.0018
5NbTi (Anatase)	5.9±0.3	3.7992±0.0005	9.5033±0.0019
0NbTi (Rutile)	>100	4.5926±0.0001	2.9589±0.0001
0.5NbTi (Rutile)	>100	4.5945±0.0001	2.9594±0.0001
1NbTi (Rutile)	>100	4.5973±0.0001	2.9603±0.0001
2NbTi (Rutile)	>100	4.6032±0.0001	2.9612±0.0001
5NbTi (Rutile)	>100	4.6033±0.0001	2.9614±0.0001

5.3.2 Surface energy measurements

The surface energies of the polymorphs were determined using water adsorption microcalorimetry. Fig. 17 shows the isotherm curves for anatase phase. Enthalpy of adsorption plotted against water coverage is shown in Fig. 17a and water coverage versus relative pressure in Fig. 17b. According to Castro and Quach [114], the adsorption behavior shows the presence of three stages based on the derivative of the adsorption isotherm curve. At very small relative pressures (<0.02), there is a rapid increasing on coverage when the pressure increases. The enthalpies of water adsorption in this first stage are very negative, suggesting a highly reactive surface. These exceedingly negative heats at low coverage indicate that there is a strong exothermic reaction in the first few monolayers. This can be explained by the dissociative nature of water due to chemisorbed water bonds with the surface [113]. For

the second stage, which is up to about 0.3, the slope of the isotherm is smaller. In addition, at the third region (relative pressure >0.3), the slope of the isotherm curve rapidly increases. However, the differential enthalpy of water adsorption gets close to the enthalpy of liquid water condensation, -44 kJ/mol (dotted line at Fig. 17a), indicating that the new adsorbed water layers present a liquid-like behavior [114].

In order to calculate the surface energy, one should fit the data using Eqs. 10 and 11, followed by solving differential Eq. 12. Fig. 18 shows the surface energies values for 0-2 mol% Nb_2O_5-doped TiO_2 versus surface area. The surface energies and surface area are inversely proportional. The surface energy for the anatase phase decreases while the surface area increases as a function of the Nb concentration. This is consistent with the crystallite size data, and confirms an increase in the thermodynamic stability of the nanoparticles with lower surface energy [134]. This phenomenon can also be associated to surface segregation of dopants. As the Nb_2O_5 has a potential to segregate on the surface of TiO_2 under oxidizing conditions [129], the decreasing on surface energy and increasing on the surface area is expected. In addition to the thermodynamics, though, the segregated dopant, niobium pentoxide on the surface of TiO_2, can also act as pinning agent limiting the growth rate. This behavior has been also observed for chromium-doped SnO_2, an iso-structural material [141].

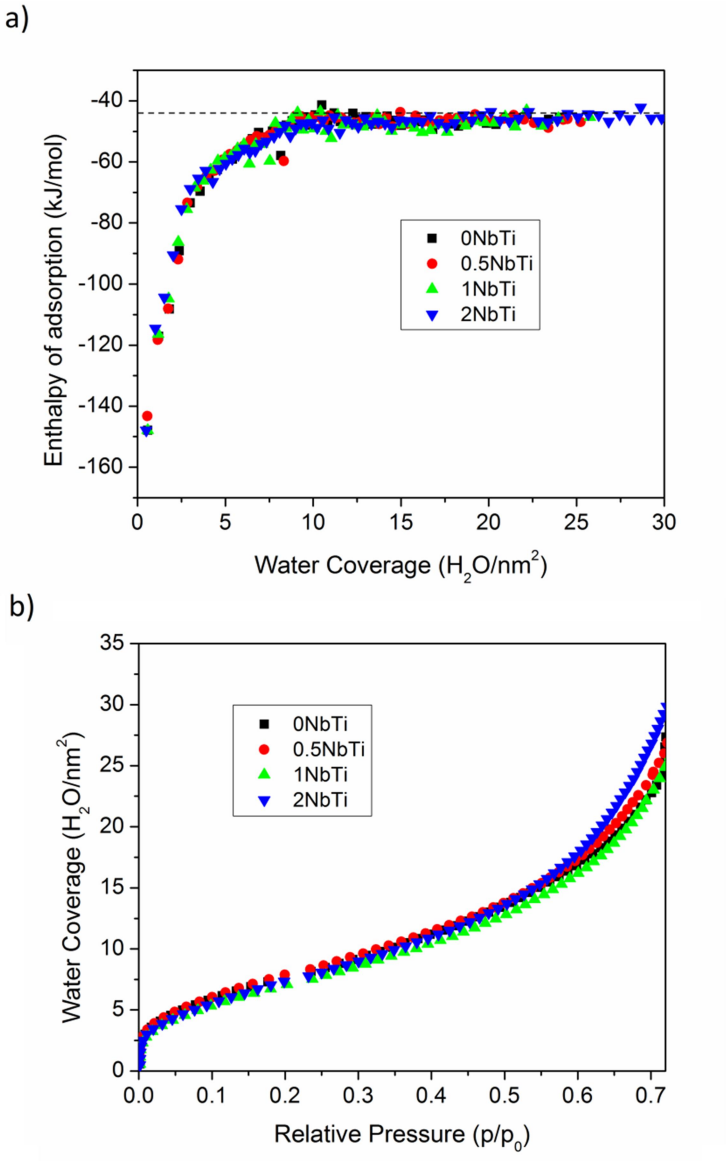

Figure 17. Water adsorption microcalorimetry data: (a) Enthalpy of water adsorption plotted against water coverage; (b) Water coverage isotherms plotted as H_2O molecules per nm² against the relative pressure.

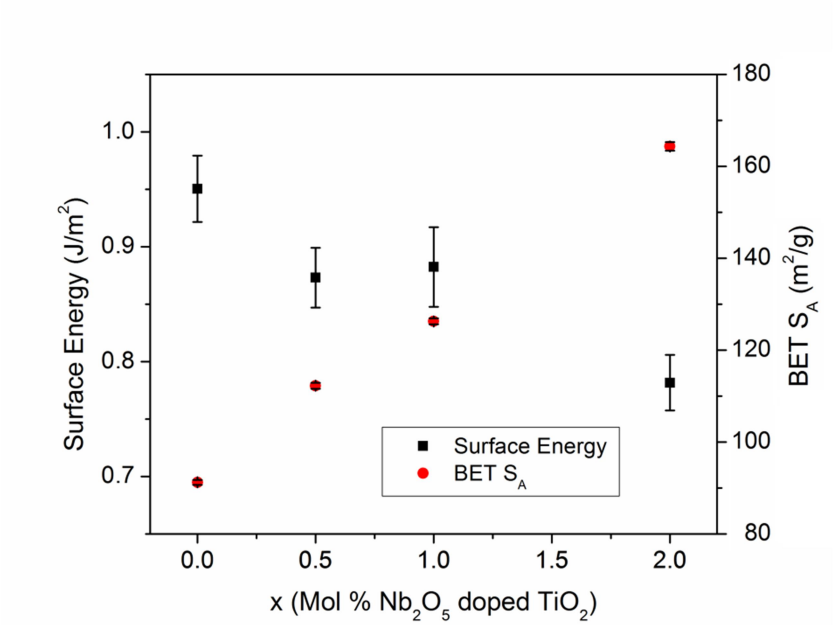

Figure 18. Surface energy (J/m²) versus BET surface area (m²/g) is plotted against 0-5 mol% of Nb_2O_5-doped-TiO_2 (anatase phase).

Table 7 compares the surface energies from this work to the literature data for undoped TiO_2 (Nb_2O_5-doped-TiO_2 surface energies are not available for comparison). The TiO_2 anatase surface energy found in this work was 0.95 ± 0.03 J/m². The results calculated with DFT by Hummer *et al*. [119] and Lazzeri *et al*. [120] for (001) plane are 0.96 and 0.90 J/m², respectively. These results are pretty consistent to the value shown in this work for undoped anatase titania. However, the values are not in agreement with simulations for other planes (100), (101) and (110) reported by Barnard and Zapol [122]. This is not contradictory, though, as in fact our experimental surface energy is a result of averaging of the contribution of all present surface planes. Naicker *et al*. [118] have found a surface energy of 2.1 J/m^2 by using molecular dynamics in whole nanoparticles (where surface planes are averaged like in our experimental work). This value is however very high, what can be explained by the fact their particles are too small (<4 nm). Small particles have non-negligible energetic effects of edges, defects, and high-index, high-energy surfaces effects on the total surface energy.

As the particle size increases, the effect of edges and defects is expected to decrease [119]. Castro and Wang [7], and Levchenko *et al*. [6] have presented experimental data on anatase surface energy for pure TiO_2 to be 0.67 ± 0.05 and 0.74 ± 0.04 J/m², respectively. These are lower than ours, but the TiO_2 particles were synthesized hydrothermally by these researchers. The synthesis method is well known to have effects on morphology of the particles and hence on average surface energies.

Table 7. Surface energies for anatase TiO_2 (J/m^2) as measured by water adsorption microcalorimetry and literature data as indicated by the superscripts.

Reference	Surface energies for anatase TiO_2 (J/m^2)
Castro and Wang [7]	0.67 ± 0.05
Levchenko et al. [6]	0.74 ± 0.04
Hummer et al. [119]	0.96 (001) 0.51 (100) 0.41 (101)
Lazzeri et al. [120]	0.90 (001) 1.09 (110) 0.44 (101)
Barnard and Zapol [122]	0.51 (001) 0.81 (110) 0.35 (101)
Naicker et al. [118]	2.1
This work	0.95 ± 0.03 (0NbTi) 0.87 ± 0.03 (0.5NbTi) 0.88 ± 0.03 (1NbTi) 0.78 ± 0.02 (2NbTi)

Due to limitations of the water adsorption microcalorimetry technique on measuring coarsened samples, it was not possible to directly determine the surface energy of rutile polymorphs. For the phase stability analysis, the rutile surface energy was assumed as 2.2 ± 0.07 J/m² based on recent calorimetric experiments [6].

Fig. 19 shows the differential scanning calorimetry data for 0-2 mol% Nb_2O_5-doped TiO_2 from 300 to 1000 °C. A first large exothermic peak is attributed to the crystallization, transformation from amorphous to anatase phase [142], which is postponed by the

increasing of Nb-doping. The second smaller exothermic peak observed between 600-800 °C is attributed to the anatase-rutile phase transition. It is clearly observed that the peaks move to the right side of the graph as the doping percentage increases. This shift shows that Nb_2O_5-doping is postponing the anatase-rutile phase transition in ~150 °C, suggesting that the doped samples are more stable than undoped samples. These results agree with the increase in stability of the anatase polymorph evidenced by surface energy, surface area and grain sizes data.

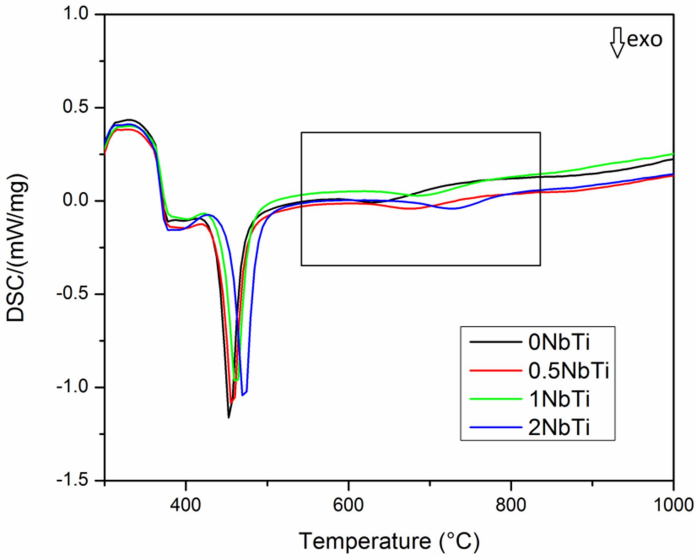

Figure 19. Differential scanning calorimetry (DSC) from 300 to 1000 °C.

5.3.3 Bulk energy measurements

Data on bulk energetics of each polymorph and composition are required to build a complete stability diagram. The bulk enthalpy can be related to its heat of "drop solution" measured by oxide melt drop solution calorimetry. The experiment is explained in detail in the experimental section. The samples were dropped from room temperature into a molten melt of sodium molybdate maintained at ~800 °C and the enthalpy of drop solution was recorded after

complete dissolution. Taking the differences in heat of drop solution of each phase, it is possible to determine the enthalpy difference during phase transition. In order to remove any surface contribution from the dissolution process and extract bulk enthalpy data, the rutile phase was calcined at 1200 °C for 2 h. On the other hand, since anatase could not be coarsened under the risk of transforming to rutile, the anatase data were corrected for adsorbed water and surface energy effects using the water adsorption data and heat content of H_2O vapor between 25 and 800 °C as 29.05 kJ/mol (see reference [134] for details on drop solution corrections).

Table 8 shows the uncorrected and corrected enthalpy of drop solution (ΔH_{ds}) measured for rutile and anatase phases of TiO_2 and Nb_2O_5-doped TiO_2. The differences among ΔH_{ds} for undoped TiO_2 rutile and doped samples are very small, but one observes that the uncorrected ΔH_{ds} tends to be less endothermic with the increasing of Nb_2O_5 concentration, while the surface-corrected ΔH_{ds} for bulk anatase shows negligible variance. This behavior confirms that Nb_2O_5-doping is stabilizing the anatase phase by decreasing its surface energy. According to the data presented in Table 8, the bulk-enthalpy of phase transition of TiO_2 is 10.02 ± 0.74 kJ/mol. The data found in the literature have a significant variation. Ranade *et al*. [143] have reported rutile-anatase enthalpy of transformation for TiO_2 being 2.61 ± 0.41 kJ/mol. Navrotsky and Kleppa [144], have obtained the enthalpy of phase transformation at 968 K as 6.57 ± 0.79 kJ/mol. They have used high-temperature oxide melt solution calorimetry in both cases [143, 144]. Hummer *et al*. [119] suggested that the transition enthalpy for the nanoanatase to nanorutile is 3.5, 6.8, and 2.5 kJ/mol for 1, 2, and 3 nm particles, respectively. They reported that the contribution of edges and vertices to the total surface energy decreases with particle size, while the change in the contribution from 2D surface structure is more modest. As a consequence, if edge and corner energies were not taken in consideration, the total transition enthalpy for nanoanatase to nanorutile would become 25.3, 11.9, and 13.2 kJ/mol for 1, 2, and 3 nm particles, respectively [119].

Table 8. The oxide melt drop solution enthalpies are tabulated for both the as measured drop solution experiments (ΔH_{DS}) and bulk corrected enthalpies (ΔH_{Bulk}). The number in parentheses denotes the number of drops reported in the average value and used to determine the standard errors.

Sample	*Enthalpy of drop solution ΔH_{DS} (kJ/mol)*	*Bulk enthalpy of drop solution ΔH_{Bulk} (kJ/mol)*
0NbTi (Anatase)	75.08±0.56(6)	63.90±0.69(6)
0.5NbTi (Anatase)	76.19±0.96(7)	65.75±1.06(7)
1NbTi (Anatase)	78.43±0.58(7)	67.73±0.97(7)
2NbTi (Anatase)	80.29±0.36(7)	65.17±0.76(7)
0NbTi (Rutile)	73.92±0.77(11)	73.92±0.77(11)
0.5NbTi (Rutile)	73.59±0.77(10)	73.59±0.77(10)
1NbTi (Rutile)	74.86±0.79(10)	74.86±0.79(10)
2NbTi (Rutile)	72.54±0.76(12)	72.54±0.76(12)

The final data necessary to complete the nanophase diagram are entropy values, which require Cp measurements from zero absolute to room temperature. In this case, Drazin and Castro [136] have suggested the use of surface energy, bulk enthalpy, and entropy data to create the diagram for the surface area and grain size critical for the phase transformation. According to their work, a standard surface excess term is generally added to the Gibbs free energy to account for the increased surface area (Eq. 13).

$$G = H - TS + \mathrm{SA}\gamma \tag{13}$$

where H is the molar enthalpy in kJ/mol; T is the absolute temperature in K; S is the molar entropy in J/mol; SA is the surface area in m²/mol; and γ is the surface energy in J/m².

The Gibbs free energy should be zero at chemical equilibrium between any two α and β polymorphs. Considering that the reaction occurs via a constant surface area process, we can write Eq. (14), where the delta symbol corresponds to the difference in the appropriate quantity of α and β polymorphs.

$$\Delta G_{\propto\rightarrow\beta} = \Delta H_{\alpha\rightarrow\beta} - T\Delta S_{\alpha\rightarrow\beta} + \mathrm{SA}\cdot\Delta\gamma_{\propto\rightarrow\beta} = 0 \tag{14}$$

The surface area of transition can be solved rearranging Eq. (14) as shown in Eq. (15). In order to the transformation happens naturally the denominator and numerator have to be positive simultaneously.

$$\mathrm{SA} = \frac{(H_\beta - H_\alpha) - T \cdot (S_\beta - S_\alpha)}{(\gamma_\beta - \gamma_\infty)} \tag{15}$$

The entropies for anatase and rutile are reported in the literature and have similar values [S^0 (298 K, rutile) = 50.35 ± 0.1 J/mol·K and S^0 (298 K, anatase) = 49.79 ± 0.1 J/mol·K] [145]. Nevertheless, $T\Delta_S$ was included in the calculations, but it did not change the overall sequence of stability. It was assumed here that entropic contributions for the small Nb doping are negligible.

5.3.4 Stability crossover and composition dependence

The nanophase diagram for Nb_2O_5-doped-TiO_2 is shown in Fig. 20. The stability crossover between the two polymorphs was calculated in m²/mol. However, the grain size is a more prevalent parameter. Thus, the surface area crossover was converted to grain size using the molar mass and density of Nb-Ti in conjunction with an approximation for the ideal specific surface area of a circular particle using Eq. 16.

$$\mathrm{SA}\left(\frac{m^2}{g}\right) = \frac{6}{\rho d} \tag{16}$$

where SA is the surface area; ρ is the density; and d is the grain size [136].

The calculated crossover between the two polymorphs in function of Nb_2O_5-concentration was fitted using the exponential Eq. 17.

$$\mathrm{y} = y_0 + 13.13686 \times \left(1 - e^{\left(-\frac{x}{0.568}\right)}\right) \tag{17}$$

where y is the crossover grain size; y_0 is the crossover for undoped TiO_2, which is 17.6 nm for this work; and x is the Nb_2O_5 molar fraction.

The shaded regions show the stable TiO_2 polymorph given a grain size in nm and Nb_2O_5 content in mole percent. According to the nanocrystalline phase diagram, Nb_2O_5-doping allows the TiO_2 to

grow more in anatase phase before it transforms into rutile. The shape of the curve is similar to the inverse trend of surface energy against doping content. Therefore, it is attributed the anatase stability according to the Nb concentration to the decreasing in surface energy.

Experimental data were collected to verify the veracity of the diagram. Samples were intentionally calcined to achieve specific grain sizes and the phases analyzed by X-ray diffraction. The results are shown in Fig. 20 as red squares for rutile phase and blue circles for anatase. These experimental results fit well with the proposed nanocrystalline diagram, confirming that the energetic analysis is quite predictive with respect to the phase stability.

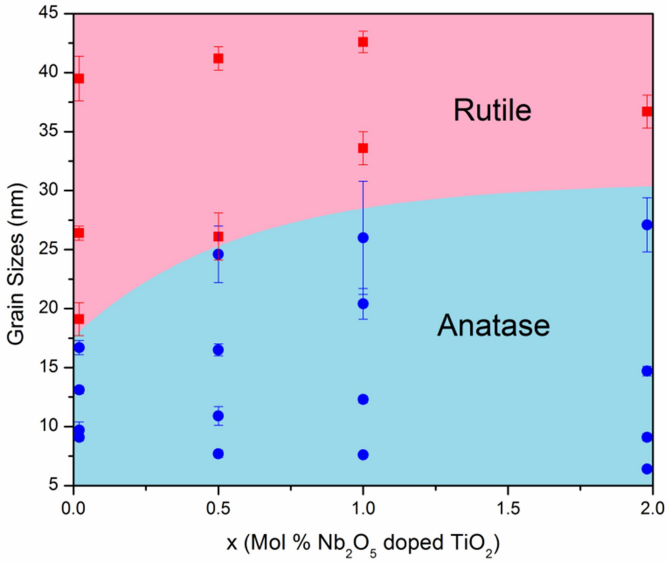

Figure 20. Grain size nanophase diagram. The shaded regions show the stable titania polymorph given a grain size in nm and Nb_2O_5 content in mol percent. The color coding is light red for rutile phase and light blue for anatase phase. Red square points are rutile phase obtained from real samples and grain sizes calculated using a WPF Refinement in JADE 6 Software. Blue dots are anatase phase real samples with grain sizes calculated using a WPF Refinement in JADE 6 Software.

The anatase-rutile crossover has been studied for undoped TiO_2 by several researches and the critical transformation values vary considerably. Barnard and Zapol [122], using density functional calculations, have found the anatase-rutile phase transition to be ~9.3 nm. They also reported that the transition energy and size vary depending upon factors such as reaction atmosphere and synthesis conditions. The anatase-to-rutile phase transition size also depends on the surface passivation. The size increases significantly to 23.1 nm when both the bridging oxygen and under-coordinated titanium atoms of the surface trilayer are H-terminated. Zhang and Banfield [54], assuming the surface stress equals the surface free energy in value, have reported that anatase is more stable than rutile for particle sizes lower than 14 nm, and lower than 9 nm if surface stress is not considered. Li *et al*., [146] using sol gel synthesis, have suggested the critical size for transition of anatase to rutile in somewhere between 32 and 42 nm. Castro and Wang [7], and Levchenko *et al*., [6] have reported the critical size for free nanoparticles as 61 and 67 nm, respectively. According to this short literature survey, this interval (9-67 nm) can be affected by the synthesis method, particle morphology, surface stress and purity. The data of this work fits within this, as it is a very broad range. Regardless of agreement with literature, these experimental results demonstrate that the thermodynamics of nanosized TiO_2 and the effect of dopants can significantly affect the polymorphism. In a particular set of samples, the thermodynamic data can be used to predict polymorphism.

5.4 Conclusions

A predictive anatase-rutile phase transition diagram was built at nanoscale for Nb_2O_5-doped-TiO_2. Nb_2O_5-doping postpones the ART, allowing the anatase grains to grow more than undoped TiO_2 before phase transition is observed. The stability crossover for undoped TiO_2 was found to be 17.3 nm, while 2 mol% Nb_2O_5-doped-TiO_2 crossover is ~30 nm. The nanophase diagram agrees with the experimental data used in this work. The surface energy for Nb_2O_5-doped-TiO_2 decreases systematically as the Nb concentration increases, confirming the higher stability for doped samples. This result is a powerful predictive tool that can be applied for nanotechnological efforts on Nb-Ti oxide systems.

6. PHOTOCATALYTIC Nb_2O_5-DOPED TiO_2 NANOPARTICLES FOR GLAZED CERAMIC TILES[3]

In this chapter, TiO_2 nanoparticles doped with 0 to 5 mol% Nb_2O_5 were synthesized by simultaneous precipitation. The anatase to rutile phase transformation was studied as a function of the temperature. Photocatalytic activity of anatase polymorph was measured by the decomposition rate of methylene blue under ultraviolet and daylight illumination and compared to commercial standard catalyst (P25).

6.1 Introduction

Oxide photocatalysts have been intensively investigated for applications in air and water remediation, self-cleaning and self-sterilizing surfaces. Among different photocatalytic materials, titanium dioxide (TiO_2) is by far the most attractive choice due to its high chemical stability, environmental inertness, and relative low cost [4, 147, 148]. One of the most emergent applications of TiO_2 is on glazed ceramic tiles [69, 70, 79]. The most common deposition techniques of TiO_2 on tile surfaces are roller printing [70], ink jet printing [70], spraying [69, 74, 79] and dip coating [68]. Ceramic tiles have received particular attention in the last years regarding innovative applications and manufacturing processes, such as reduced thickness products [65, 66] , digital decoration [149] and antimicrobial activity [150, 151], which aggregate value to those building materials.

When a TiO_2 photocatalyst site absorbs a photon with energy equal to or greater than its band-gap, an electron–hole pair is generated; subsequently, the pair is split into a free electron and a free hole [4]. The photogenerated electron/hole pair promotes the reduction and oxidation of species adsorbed at the surface of the semiconductor and induces oxidative degradation of species in solution through radical reactions [21]. Therefore, when TiO_2 is irradiated with UV-light, it can decompose organic dyes such as methylene blue (MB) [152, 153], alizarin S [154, 155], crocein orange G [154], methyl red [154, 156], and congo red [154, 157]. MB is commercially employed in textile, leather and paper

[3] Published in Ceramics International 42 (2016) 5113-5122. http://dx.doi.org/10.1016/j.ceramint.2015.12.029

industries, and it is one of the most used dyes for measurement of photocatalytic activity. Since dye-containing wastewater can block both sunlight penetration and oxygen dissolution, which are essential for aquatic life, there is considerable interest in treating these colored effluents before discharging them to water bodies [158]. Furthermore, discoloration of MB dye as a model pollutant is most often used for testing of materials with self-cleaning properties [69, 79, 159].

The optimization of TiO_2 performance as photocatalyst is an active research field given the above mentioned industrial relevance. This entails understanding the dependences of the catalytic behavior on the system chemistry, structure and microstructure. TiO_2 has three main polymorphs: rutile, anatase and brookite. Among those, anatase presents generally the highest activity, which is improved from high crystallinity and surface area [23, 62, 160], although a mix of anatase and rutile can improve photoactivity in some cases [56, 161-163]. Kordoult *et al.* [164] have studied the photodegradation of two representative azo-dyes, one acidic (Orange G) and one basic (Yellow 28) for different anatase-rutile ratios. For both azo-dyes they have showed that the increasing of rutile percentage decreases the photoactivity ratio.

Several dopants have been used to postpone the anatase-to-rutile transformation (ART) while simultaneously changing physical-chemistry of the surface of TiO_2 in order to increase its photocatalytic performance. For instance, rare-earth-doped TiO_2 has led to increased photocatalytic activity under visible light as compared to pure titanium dioxide [34-36]. Transition metals have also improved activity by reducing the recombination of photogenerated electrons and holes [37, 165, 166]. Non-metal doped TiO_2 has shown improvement on absorption and photocatalytic activity in the visible light region [38, 167].

Niobium has been considered a promising candidate for enhanced catalysis of titania [168]. The ionic radius of Nb^{5+} (0.64 Å) is only slightly larger than Ti^{4+} (0.605 Å). Thus, Nb^{5+} can form solid solution in the lattice of TiO_2. To compensate the excess charge of Nb^{5+} in substitution to Ti^{4+}, one Ti cation vacancy may be created per 4 Nb introduced. Alternatively, the stoichiometric reduction of Ti^{4+} to Ti^{3+} may also occur depending on preparation conditions, which will introduce shallow donor levels below the conduction band (CB) edge of TiO_2 [41, 42]. The electronic transition from valence band (VB) to these donor levels will be excited by the

visible light and therefore render the Nb-doped TiO_2 photocatalyst to be visible light responsive, such as nonstoichiometric TiO_2 [43].

Nb_2O_5-doped titania has been shown to have higher photocatalytic activity for the degradation of diquat dibromide monohydrate under UV-light as compared to pure TiO_2 [44]. Photocatalytic oxidation of 4-chlorophenol and iodide as well as the photoreduction of hexavalent chromate (Cr^{6+}) have been studied by Nb-TiO_2 catalysts, which presented enhanced photocatalysis under visible light [45].

In this work, the temperature of the anatase to rutile phase transition as a function of Nb_2O_5-doping concentration was studied in titania nanoparticles prepared by simultaneous precipitation in order to enhance anatase stability. The presence of anatase or anatase/rutile mixed phases at the 700–800 °C would allow the use of titania powder as a coating in glazed ceramic tiles, particularly for those processes which include a second firing stage at this temperature range for decoration purposes.

6.2 Experimental Procedure

6.2.1 Sample preparation

TiO_2 nanoparticles containing 0, 0.5 1, 2, and 5 mol% Nb_2O_5 were synthesized by simultaneous precipitation. The respective compositions were named 0NbTi, 0.5NbTi, 1NbTi, 2NbTi and 5NbTi. Titanium (IV) isopropoxide (TTIP, Sigma-Aldrich, ≥97%) and niobium butoxide (NB, Sigma-Aldrich, 99%) were used as Ti and Nb precursors, respectively. TTIP and NB were mixed for 10 min and they have visually formed a homogeneous solution. No partially pre-hydrolyzed was observed in this step. Thus, the solution was added dropwise into an ammonium hydroxide solution (NH_4OH, 5 M, Fisher Scientific) under vigorous stirring. The colloidal suspension was centrifuged at 3000 rpm for 5 min to separate the nanopowder from the liquid. The powder was then washed three times (in water, water/ethanol 1:1 in volume, and ethanol, respectively). The samples were dried at 90 °C for 72 h and ground with a pestle and mortar. The calcination procedure was performed in a box furnace (Lindberg/Blue M) at different times and temperatures (450–900 °C). For the photocatalytic experiments, calcination temperatures that lead to anatase-only with maximum

specific surface area were selected for each composition, i.e. 450 °C for 0NbTi, 2NbTi and 5NbTi; and 500 °C for 0.5NbTi and 1NbTi.

6.2.2 Characterization of powders

Powder X-ray Diffraction (XRD) patterns were obtained using a Bruker AXD D8 Advance diffractometer (Bruker AXS, Madison, WI) with Cu*K*α radiation, and λ=1.5406 Å, operated at 40 kV and 40 mA. Data were collected in the range 20–90° (2-theta) and the pattern profile fitting was performed using the Jade 6.1 (MDI) software to determine crystal structure, phase purity, and crystallite size. Specific surface area measurements were carried out using the Brunauer, Emmett, and Teller (BET) method with nitrogen gas adsorption (Micromeritics Gemini VII). Thermogravimetry results have showed that significant mass changes can only be observed up to 400 °C; hence, this temperature was selected for degassing prior to BET experiment (Micromeritics VacPrep 061, sample degassing system). Surface morphology and particle size distribution were analyzed by High Resolution Transmission Electron Microscopy (HRTEM; Jeol JEM 2500SE with 200 keV). The absorption studies were carried out by UV-visible spectrophotometer (Evolution 220, Thermo Scientific). The UV–vis absorption spectra were recorded in the wavelength range 300–800 nm. The values of the energy band gap were determined applying Kubelka-Munk phenomenological theory assuming the indirect band gap [169].

6.2.3 Photocatalytic activity

The photocatalytic activity of the prepared nanoparticles was assessed in liquid–solid media monitoring the degradation of the organic dye methylene blue (MB, Sigma-Aldrich) under UV and visible light. Commercial titania photocatalytic powder (Degussa, Evonik P25, Aeroxide TiO_2) was used as reference for comparison. P25 has been used as a reference photocatalyst due to high levels of activity in many reaction systems as reported in the literature [170].

The tests were performed at room temperature, in a cylindrical photocatalytic reactor (86 mm in diameter) containing an aqueous solution of the dye (0.3 L), at an initial concentration of 10 μmol. The concentration of the photocatalyst in the slurry was normalized by surface area (6 m^2) and by weight (50 mg). Table 9 shows the amount of powder used in the photocatalytic experiment for each

sample. In order to mix the solution thoroughly, the slurry was magnetically stirred throughout the reaction. The reactor was designed following the guidelines of the international standard ISO 10678 [93]. The distance between the lamp and the slurry was ~8.5 cm to obtain 10 $W \cdot m^{-2}$ intensity in the middle of the solution measured by radiometer (General UV513AB, Digital UV AB Light Meter). UV-light (GE black light F15) and visible light (GE daylight F15) sources were used.

Table 9. Nb_2O_5-doped TiO_2 and P25 characterization (specific surface areas and amount of powder used for photocatalytic activity).

Sample	*Calcination temperature (°C)*	*Calcination time (h)*	*Specific surface area ($m^2 \cdot g^{-1}$)*	*Amount of powder (mg)*[a]
0NbTi	450	7	92.5 ± 0.6	64.86
0.5NbTi	500	5	85.6 ± 0.5	70.09
1NbTi	500	5	92.9 ± 0.5	64.61
2NbTi	450	7	125.4 ± 0.6	47.86
5NbTi	450	7	168.9 ± 0.6	35.52
P25	---	---	54.1 ± 0.5	110.93

[a]Referring to ~6 m².

Along the experiments, the photocatalytic degradation of MB was monitored by sampling about 3 mL of the slurry from the reactor, at regular time intervals (up to 7 h). Before turning the lamps on, the suspensions with the photocatalyst were stirred in the dark for 10 min. The powders were separated from the suspension by centrifugation, and then the MB concentration in the liquid was determined by measuring the absorbance in a spectrometer (PerkinElmer precisely, Lambda 750 UV/vis Spectrometer) at a wavelength of 664 nm, using distilled water as reference.

6.3 Results and discussion

6.3.1 Structural characterization of Nb_2O_5-doped TiO_2

The prepared Nb_2O_5-doped TiO_2 powders were analyzed by XRD to verify the purity, crystallinity and phase(s) of samples calcined at different temperatures (450–900 °C). The powder XRD patterns of doped and undoped samples are shown in Fig. 21. At 450 and 500 °C most samples presented single anatase phase (JCPDS card n. 71-

1167), showing broad peaks typical of nanosized crystallites. A small amount of brookite (JCPDS card no. 76–1937) is observed in 1NbTi, 2NbTi and 5NbTi samples calcined at 450 °C, 500 °C and 600 °C. The existence of brookite in the samples can be identified by the diffraction peaks at 30.71 (211, reflection). Co-existence of anatase and brookite frequently occurs in water-based synthesis, but the photocatalytic activity, which is primarily responsible for the anatase phase, has been reported to be unaffected by it [171]. The diffraction peaks at 25.31, 37.81, 48.1, 53.91 and 55.1 can be indexed to the (101), (004), (200), (105) and (211) reflections of anatase TiO_2. The presence of rutile phase (JCPDS card n. 86-0147) was detected only at temperatures above 600 °C. The diffraction peaks at 27.41, 36.21, 41.31, 54.41 and 69.11 can be indexed to the (110), (101), (111), (211) and (112) reflections of rutile TiO_2.

Fig. 22 shows a compilation of rutile weight percentage determined from XRD patterns as a function of temperature of calcination. It is observed that the stability of anatase phase is enhanced with increasing Nb_2O_5 concentration. At 600 °C, the rutile percentage of 0NbTi, 0.5NbTi and 1NbTi is 48.4%, 19% and 6.8%, respectively. On the other hand, 2NbTi and 5NbTi did not show any transformation at this point. At 700 °C, just 5NbTi presents pure anatase phase. Other compositions have shown anatase–rutile mixture. The trend shown in Fig. 22 suggests that Nb_2O_5-doping can stabilize the anatase phase and postpone the phase transition to rutile. The ART delaying can be attributed to the formation of strong Nb–O–Ti bonds, which inhibit the movement of surface Ti atoms required to initiate the phase transformation [172]. The mobility of oxygen vacancies also influences the phase transformation rate, because they act as nucleation sites for the anatase to rutile transition [41]. This is expected to be decreased with increasing Nb content due to its higher valence (+5) substituting (+4) titanium sites.

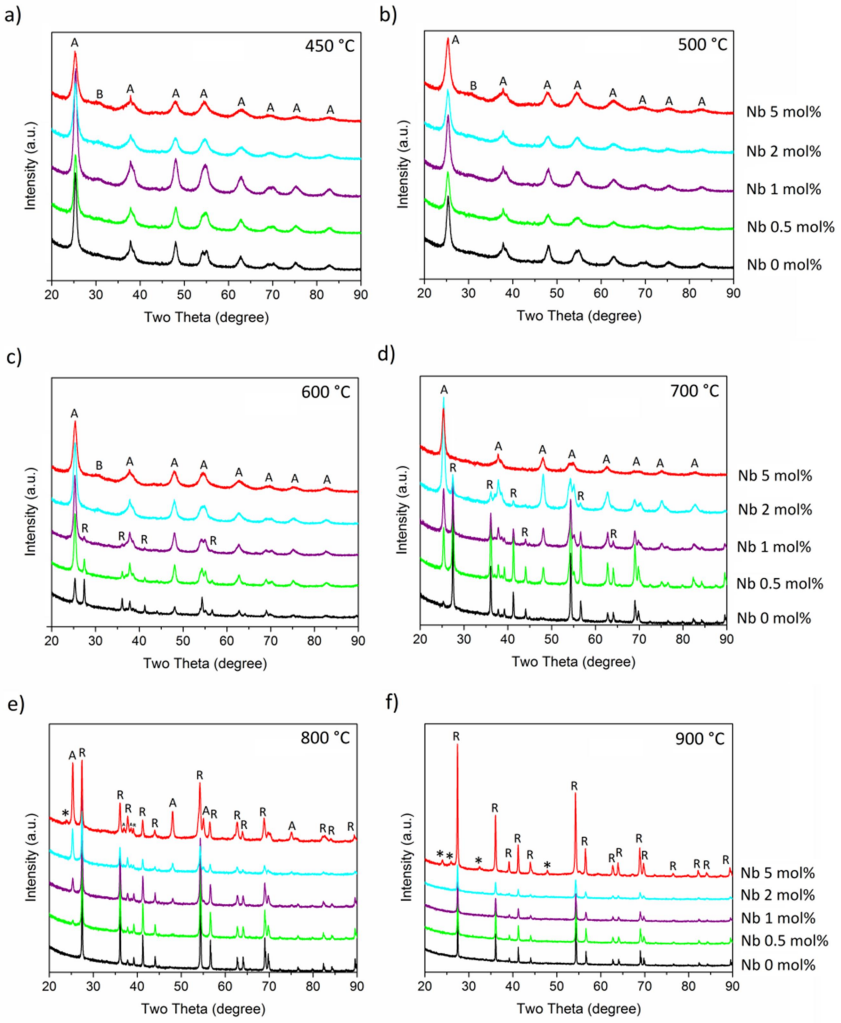

Figure 21. XRD patterns of Nb_2O_5-doped TiO_2 (0-5 mol%) calcined at 450-900 °C. a) 450 °C, b) 500 °C, c) 600 °C, d) 700 °C, e) 800 °C and f) 900 °C. (A-anatase; R-rutile; *$TiNb_2O_7$).

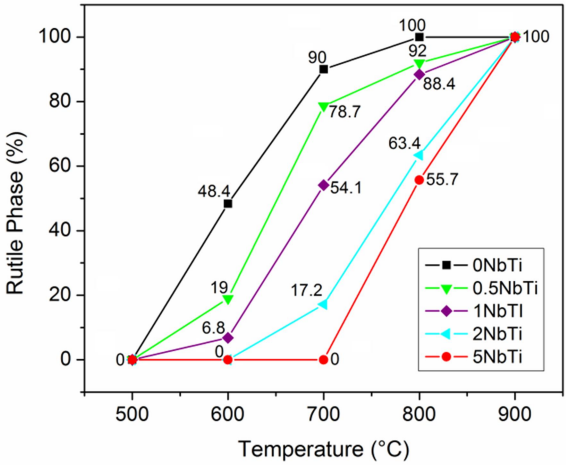

Figure 22. Rutile weight percentage as a function of the calcination temperature for Nb_2O_5-doped and non-doped TiO_2. Complementary percentage is anatase.

At 800 °C, 0NbTi has shown pure rutile phase, while the doped samples presented anatase–rutile mixed phases in different fraction weights, following the trend observed at 600 and 700 °C. Thus, the postponing of anatase–rutile phase transition by Nb_2O_5-doping may allow the use of TiO_2 as a high efficient photocatalyst material in systems that require higher processing temperatures. At 900 °C, all compositions have completely transformed to rutile. However, 5NbTi presents the titanium niobium oxide phase ($TiNb_2O_7$ – monoclinic, JCPDS card no. 39–1407) in addition to the rutile phase.

Traversa *et al.* [173] have studied Nb-doped-TiO_2 and Ta-doped-TiO_2 nano-sized powders to use at thick-film gas sensors for atmospheric pollutant monitoring. In their work, the presence of Nb (5 at% and 10 at%) has postponed the ART by about 200 °C, which agrees with this work. However, in Traversa's work the transition from anatase to rutile started 50 °C higher than what was reported here, even for pure TiO_2. This difference may be attributed to the synthesis method, which was sol–gel, but also to the presence of agglomerates (solid–solid interfaces) that has been proven to affect the anatase–rutile transition [7].

Atanacio *et al*. [129] have showed that niobium has a potential to segregate on the surface of TiO_2 under oxidizing conditions. Moreover, the segregation-induced enrichment of the surface in niobium results in the formation of a $TiNb_2O_7$-type surface structure. The observation of $TiNb_2O_7$ phase at 800 and 900 °C for the 5 mol% Nb_2O_5-doping suggests that niobium is segregated on the surface of TiO_2. However, the second phase remains undetectable for samples annealed at low temperature possibly because of a lack of crystallinity associated with very small grain sizes that would not provide enough coherent scattering in XRD [174]. Higher temperatures increase the crystallite size of the $TiNb_2O_7$ phase, making it visible.

Table 9 and 10 show a list of the powders tested for photocatalysis selected among those in which no rutile or second phases are observed. P25 was included as a reference. Specific surface area and the amount of powder were used as input data to provide ~6 m^2 of reactive surface. The samples with 0.5 and 1 mol% Nb_2O_5-doped TiO_2 were calcined at 500 °C for 5 h instead of 450 °C for 7 h in order to reach SA values close to those of pure TiO_2. The BET S_A values found for 0NbTi, 0.5NbTi and 1NbTi were 92.5 ± 0.6, 85.6 ± 0.5 and 92.9 ± 0.5 $m^2 \cdot g^{-1}$, respectively. For 2NbTi and 5NbTi, the values increased to 125.4 ± 0.6 and 168.9 ± 0.6 $m^2 \cdot g^{-1}$, respectively. The increase at the specific surface area for 2NbTi and 5NbTi when compared to pure TiO_2 is due to the lower crystallite sizes, which is shown in Table 10.

The anatase crystallite sizes, as determined by XRD for samples calcined at 450 °C for 7 h were 9.6 ± 0.5, 7.1 ± 0.2 and 6.0 ± 0.3 nm for 0NbTi, 2NbTi and 5NbTi respectively. This systematic decrease suggests that Nb_2O_5-doping is stabilizing TiO_2 nanopowder and consequently helping to postpone the ART. The Nb^{5+} radius is slightly larger than the Ti^{4+} radius and this means that Nb^{5+} induces a slight stress in the titania lattice, which may hinder the growth of the TiO_2 crystallites [175]. Moreover, Guidi *et al*. [176] suggested that the main mechanism for nucleation of rutile in doped TiO_2 samples was a slow surface nucleation, which also prevented conspicuous grain growth, and ascribed such inhibitions to a decrease in the ionic oxygen mobility. The powders calcined at 500 °C for 5 h presented crystallite sizes as 10.9 ± 0.5 and 9.0 ± 0.3 nm for 0.5NbTi and 1NbTi, respectively. These powders did not follow the trend showed for 0NbTi, 2NbTi and 5NbTi, because they were calcined at different times and temperatures. For comparison

purposes, P25 was also characterized. The BET S_A of P25 (54.1 ± 0.5 $m^2 \cdot g^{-1}$) is smaller than those values of any Nb_2O_5-doped-TiO_2 or pure TiO_2 used for photocatalytic activity in this work. P25 presented 81.1 wt% anatase and 18.9 wt% rutile and crystallite sizes of 22 ± 1 and 38 ± 8 nm for anatase and rutile, respectively.

Table 10. Nb_2O_5-doped TiO_2 and P25 characterization (Anatase and rutile crystallite sizes and wt%).

Sample	*Anatase (wt%)*	*Anatase crystallite size (nm)*	*Rutile (wt%)*	*Rutile crystallite size (nm)*
0NbTi	100	9.6 ± 0.5	0	---
0.5NbTi	100	10.9 ± 0.5	0	---
1NbTi	100	9.0 ± 0.3	0	---
2NbTi	100	7.1 ± 0.2	0	---
5NbTi	100	6.0 ± 0.3	0	---
P25	81.1	22 ± 1	18.9	38 ± 8

Fig. 23(a) and (b) shows HRTEM images for 0NbTi and 5NbTi calcined at 450 °C for 7 h. The particles are relatively isotropic and the estimated sizes are in the range of those obtained from XRD analysis. Powder agglomeration is also observed, which is usual in nanoparticles. Fig. 23(c) and (d) shows the size distribution of 0NbTi and 5NbTi obtained from 150 nanoparticles for both compositions. The average grain sizes determined by TEM is consistent with the values determined by XRD. The histograms show a tendency to a skewed distribution. However, 0NbTi has presented a right skewed distribution, presenting less powder above the average and 5NbTi has presented a left skewed distribution, with less powder below the mean. The decreasing on the grain size for doped samples can be attributed to the surface segregation of dopants. The hypothesis is that the presence of niobium pentoxide on the surface of TiO_2 can both affect the driving forces for particle growth and act as pinning agents limiting the growth rate. This behavior has been also observed for chromium-doped SnO_2 [141].

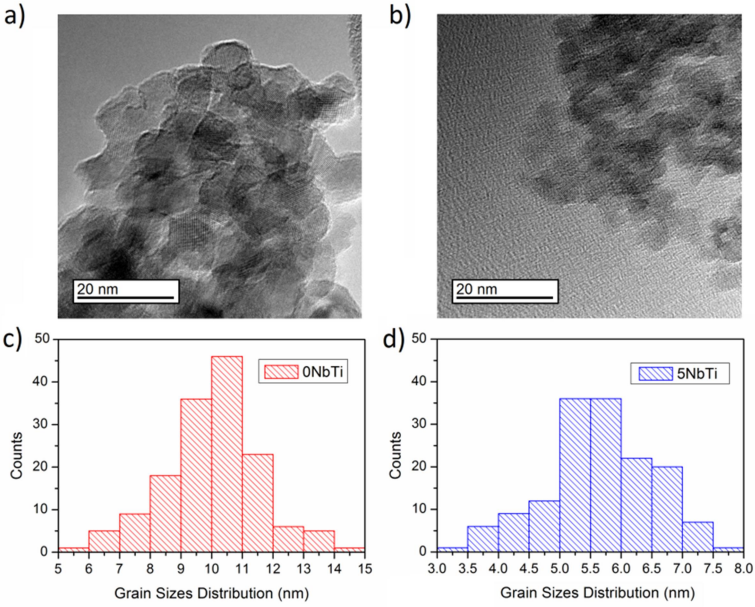

Figure 23. HRTEM of pure TiO_2 (a) and TiO_2 containing 5 mol% Nb_2O_5 (b), and grain size distribution of pure and doped powder, (c) and (d) respectively.

Fig. 24(a)–(c) shows UV–vis absorbance spectra and Kubelka–Munk plots of pure TiO_2 (0NbTi), 5 mol% Nb_2O_5doped-TiO_2 (5NbTi) and P25 respectively. The results show that Nb_2O_5 decreases the optical indirect band gap of titania from 3.20 to 3.07 eV for pure TiO_2 and 5NbTi, respectively. These results suggest that Nb_2O_5 extend the absorbance of TiO_2 to the visible light. Hence, the photocatalytic activity is expected to increase under visible light as the band gap is reduced and then produce more electron–hole pairs under visible light. The literature presents some controversies about the influence of Nb_2O_5 on the band gap. Castro *et al*. [44] have shown no difference in the band gap of pure TiO_2 and Nb-doped TiO_2. However, Yang *et al*. [168] found a reduced band gap for Nb-doped TiO_2 porous microspheres. Those divergences can be attributed to the particle morphology and/or distribution of Nb_2O_5 on TiO_2, since those powders were prepared by different synthesis methods. The smaller band gap of 5 mol% Nb_2O_5-doped TiO_2 suggests that Nb_2O_5 dopants modify the CB of TiO_2 by

downshifting the CB edge, probably through the mixing of Nb_{4d} and Ti_{3d} states [41, 177]. For comparison purpose, the P25 indirect band gap was also calculated and the value found was 3.05 eV, which agrees with the value found in the literature [178]. The narrower band gap for P25 is attributed to the presence of rutile as a mixed phase [178].

a)

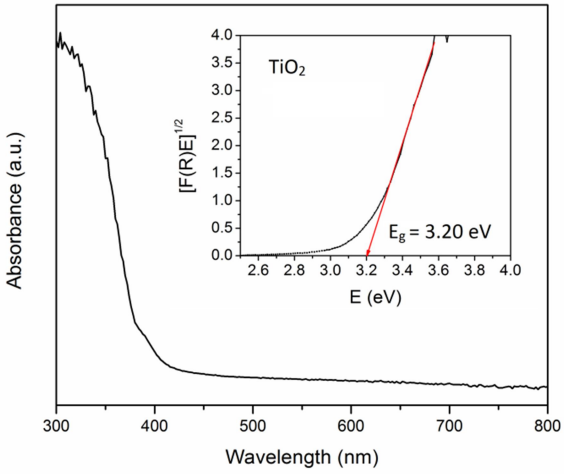

b)

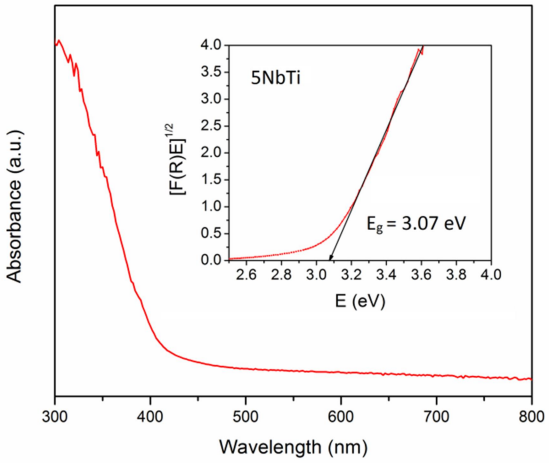

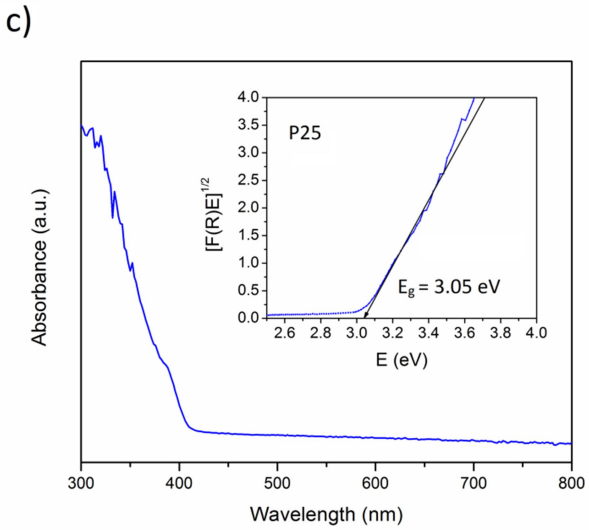

Figure 24. UV-vis absorbance spectra and Kubelka-Munk plots for: a) pure TiO_2 (0NbTi), b) 5 mol% Nb_2O_5-doped-TiO_2 (5NbTi) and c) P25.

6.3.2 Photocatalytic activity

The oxidized and reduced forms of MB have different absorption bands in the UV–vis spectrum. Therefore, the progress of discoloration or decomposition can be monitored by measuring the decrease in absorption of MB on UV-Visible spectrum at a λ_{max} of 664 nm. The evaluation of photocatalytic activities of Nb_2O_5-doped TiO_2 powders comparing to undoped TiO_2 and P25 under UV-light and visible light is shown in Figs. 25 and 26, respectively.

Light exposure in the absence of the photocatalysts did not result in the photocatalytic discoloration of MB. It is observed from Fig. 25a that the degradation of MB under UV light increases for Nb_2O_5-doped samples compared to undoped titania. For 0.5 mol% Nb_2O_5-doped TiO_2, MB degradation is slightly higher than that for non-doped TiO_2. The photocatalytic performance was similar for TiO_2 powders with Nb_2O_5 concentrations between 1–5 mol%. However, it was higher than 0.5 mol% Nb_2O_5-doped and undoped TiO_2. P25 showed the highest photocatalytic activity under UV-light. This has been reported in the literature to be associated with the small fraction of rutile in the sample, although there are still some

controversies. The hypothesis is that the co-presence of anatase and rutile crystallites induces the high level of photocatalytic activity; the transfer of photoexcited electrons and positive holes between interconnecting anatase and rutile particles would enhance charge separation and improve the efficiency of utilization of electron–hole pairs [179]. However, Ohtani *et al*. [170], after investigating structural and photocatalytic properties of a mixture of anatase and rutile particles corresponding to the components of P25, found that anatase, rutile and amorphous phases behave independently without any interaction.

The large specific surface area is beneficial to absorb more light, which could offer more adsorption sites and photocatalytic reaction centers [168]. Therefore, to minimize the influence of the specific surface area on the photocatalytic activity, the photocatalyst powders were normalized in order to get the same total surface area (6 m^2) (Figs. 25a and 26a) and the same sample weight (50 mg) (Figs. 25b and 26b). The amount of powders for Figs. 25a and 26a varies according to the specific surface area of each material and it is shown in Table 9. The 0.5NbTi and 1NbTi powders were calcined at 500 °C for 5 h in order to get similar specific surface area as pure TiO_2 and minimize any improvement of doping samples by the surface area. Hence, 0NbTi and 1NbTi have presented similar specific surface area (92.5 ± 0.1 $m^2 \cdot g^{-1}$ and 92.9 ± 0.5 $m^2 \cdot g^{-1}$, respectively). However, 1NbTi has presented higher photocatalytic activity comparing to 0NbTi, showing that the improvement on the photocatalytic activity is due to the Nb_2O_5-doping.

Fig. 25b compares the MB degradation under UV-light of 0NbTi, 5NbTi and P25 with the same catalyst concentration, normalized by weight. It can be observed that 5NbTi and P25 have a better performance comparing to the 0NbTi. On the other hand, 5NbTi and P25 have similar behavior showing total MB degradation by 2.5 h. It can also be observed that for 1 and 1.5 h 5NbTi has presented higher performance, suggesting a slightly faster kinetics of degradation.

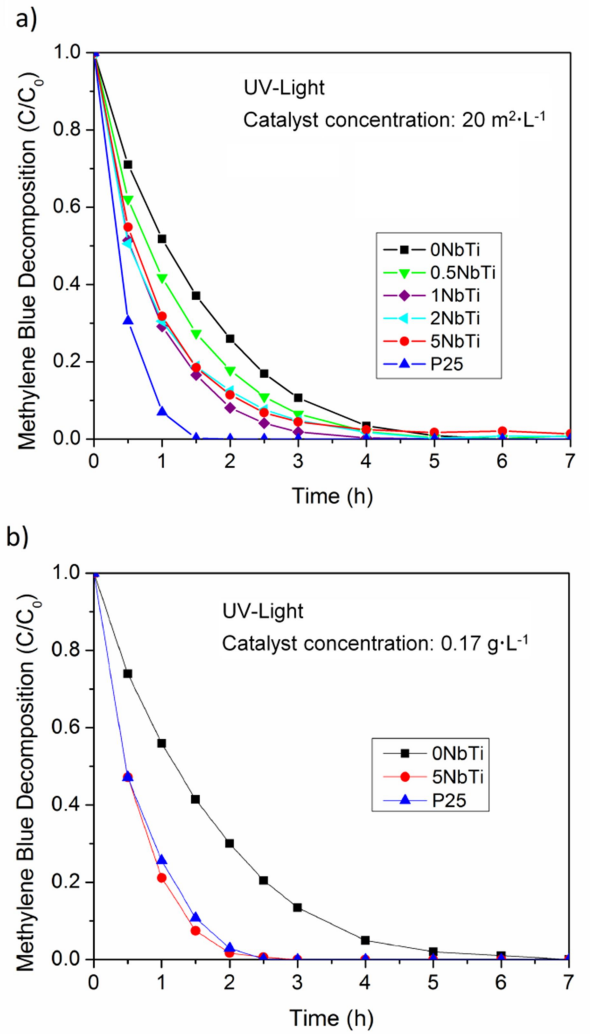

Figure 25. Photocatalytic decomposition of MB under UV-light of Nb-doped and non-doped titania. a) Amount of catalyst normalized by surface area: it was dissolved 6 m^2 of the catalyst into 0.3 L of the MB solution. The amount of powders varies according to the specific surface area of each material, which is shown in Table 9. b) Amount of catalyst normalized by weight: it was dissolved 0.05 g of the catalyst into 0.3 L of the MB solution, which gives a catalyst concentration of 0.17 g· L^{-1}.

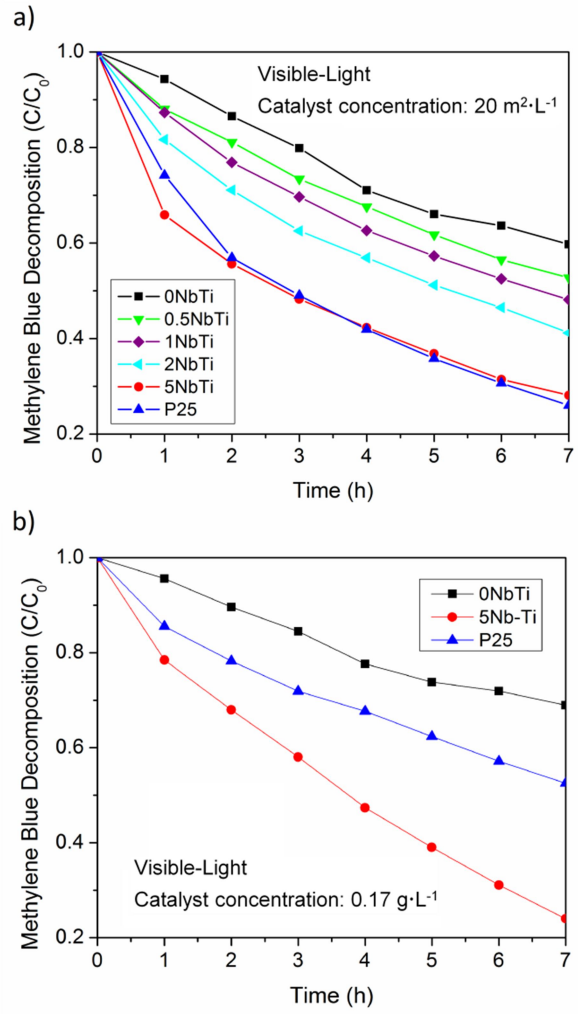

Figure 26. Photocatalytic decomposition of MB under visible-light of Nb-doped and non-doped titania. a) Amount of catalyst normalized by surface area: it was dissolved 6 m^2 of the catalyst into 0.3 L of the MB solution. The amount of powders varies according to the specific surface area of each material, which is shown in Table 9. b) Amount of catalyst normalized by weight: it was dissolved 0.05 g of the catalyst into 0.3 L of the MB solution, which gives a catalyst concentration of 0.17 g· L^{-1}.

Hirano and Matsushima [180] have prepared Nb-doped-TiO_2 (0–10 mol%) using hydrothermal method in three different conditions, in the absence and presence of urea and aqueous ammonia. They have studied the MB degradation of 50 mg of catalyst suspended in 100 mL of MB. In their best result 10 mol% Nb_2O_5-doped-TiO_2 completely degraded MB after 5 h. In the present work we have used 50 mg of 5 mol% Nb_2O_5-doped-TiO_2 suspended in 300 mL of MB and after 2.5 h the dye was completely degraded under UV-light. The different performance between the present work can be attributed to the different dilution, but also specific nanoparticle morphologies, since Hirano and Matsushima used a different synthesis method and different precursors.

The photocatalytic activity under visible light (Fig. 26a and b) shows slower degradation kinetics, but a more pronounced effect of the dopant in the overall catalytic performance of the TiO_2 nanoparticles. In Fig. 26a, where the powders were normalized by surface area, the best performance was found for 5NbTi. At the first hour of the experiment, 5NbTi has presented higher photocatalytic activity than P25. From 2–7 hours, the behaviors were similar for both powders. The improvement on photocatalytic activity of Nb_2O_5-doped TiO_2 can be attributed to the increase of the absorption under visible light and decrease of the band gap comparing to pure TiO_2 [168, 181]. Even though 5NbTi and P25 have presented similar photocatalytic degradation of MB for the same surface area, the amount of powder used for 5NbTi was around three times less than P25. The quantity of powder used for 5NbTi was 35.5 mg and for P25 was 111 mg. Fig. 26b shows the photoactivity of 0NbTi, 5NbTi and P25 with the catalyst normalized by weight (50 mg). In this case, 5NbTi has presented considerable higher activity when compared to P25 and 0NbTi. Note that P25 had moderate degradation behavior due to the limited content of powder.

The poorer behavior of the catalysts under visible light can be attributed to the photosensitized type of the reaction, where MB dye molecule is photoexcited instead of the photocatalyst. In this kind of process, an electron is transported from the photoexcited MB to the conduction band of the photocatalyst and reacts, e.g., with an O_2 molecule, which is an electron scavenger, and a superoxide radical is created. These radicals can further react towards complete decomposition of MB. It seems that even a very small overlap of the

adsorption spectra of MB and the applied irradiation is sufficient to drive the photosensitized type of reaction.

The present observation is consistent with the fact that Nb_2O_5 itself shows high photocatalytic decomposition of methylene blue, especially for Nb_2O_5 nanorods which present high surface acidity [182]. As previously mentioned, Nb^{5+} is expected to form solid solution into the lattice of TiO_2 because the ionic radius of Nb^{5+} is only slightly larger than Ti^{4+}. Once Nb^{5+} is introduced into the lattice of TiO_2, the compensation of the excess charge of Nb^{5+} in substitution to Ti^{4+} can be explained by two mechanisms. A first possibility is if one Ti^{4+} cation vacancy is created for every 4 Nb^{5+} cations (Eq. (18)). Another option is reduction of Ti^{4+} to Ti^{3+} for every Nb^{5+} incorporated (Eq. (19)) [168, 183, 184], where O^{2-} is oxidized (the equations are expressed in classical Kröger–Vink notation).

$$\frac{1}{2}Nb_2O_5 \xrightarrow{TiO_2} Nb_{Ti}^{\cdot} + \frac{1}{4}V_{Ti}^{''''} + \frac{5}{2}O_O^X \tag{18}$$

$$\frac{1}{2}Nb_2O_5 \xrightarrow{TiO_2} Nb_{Ti}^{\cdot} + Ti^{(3+)}{}'_{Ti^{(4+)}} + 2O_O^X + \frac{1}{4}O_2 \tag{19}$$

From the thermodynamic point of view, Eq. (19) is more favorable since reduction is less energetic than vacancy formation. Hence, Ti^{3+} would produce isolated states in the forbidden gap exhibiting visible light absorption and enhancing the photocatalytic property of TiO_2-based photocatalyst [185]. Moreover, the presence of active Ti^{3+} sites on the surface could serve as sites for trapping photogenerated electrons that could effectively inhibit the recombination of the photoinduced electrons and holes [186].

Yang *et al*. [168] have shown by photoluminescence (PL) emission spectra of Nb-doped TiO_2 microspheres that Nb-doped samples can have better charge separation. Nb-doping introduces shallow donor levels below the CB edge, which can act as electron traps to retard electron-hole recombination. Thus, the lifetime of photogenerated electrons and holes can be increased, which is beneficial to enhance the photocatalytic efficiency.

6.4 Conclusions

TiO_2 coating on glazed ceramic tiles with good photocatalytic or self-cleaning performance requires starting TiO_2 nanoparticles with an enhanced performance. In the present work, Nb_2O_5-doped TiO_2 nanopowder was successfully synthesized by simultaneous precipitation with Nb_2O_5 concentrations of 0–5 mol%. The anatase phase of TiO_2 was found to be stable up to 700 °C for doped samples, and thereon, initiation of rutile phase formation was observed. Nevertheless, up to 44.3 wt% anatase is present after calcination at 800 °C for 5% mol Nb_2O_5-doped TiO_2, while for non-doped TiO_2 the ART is complete at the same temperature. The crystallite sizes decrease and the specific surface area increases with the increasing of doping concentration calcined at the same temperature. All Nb-doped samples have presented higher photocatalytic activity by degradation of methylene blue than pure TiO_2 synthesized at the same condition under UV and visible light. The powders containing 5 mol% Nb_2O_5-doped TiO_2 presented similar photoactivity under UV-light and higher photoactivity than P25 under visible light, with the benefit of having very small crystallite sizes, making it more suitable for glazed ceramic coatings.

7. HIGH PHOTOCATALYTICALLY ACTIVE CERAMIC TILES WITH Nb_2O_5-DOPED TiO_2 NANOPARTICLES [4]

In this Chapter, 5 mol% Nb_2O_5 doped TiO_2 was coated on glazed ceramic tiles by spraying forming a very thin film. Superhydrophilicity was evaluated by measuring the water contact angle under UV-irradiation. The degradation of methylene blue was performed according to ISO 10678 and JIS R 1703-2.

7.1 Introduction

Photocatalytic ceramic tiles have been investigated for over than 10 years [78]. Along this period, ceramic tiles industries have developed related to technology and products. From the technological point of view, new decorating processes, as ink jet printing started to be widely used, while tiles tended to be larger and thinner [65, 66, 86]. At the same time, the production of functional ceramic tiles with innovative properties, as antibacterial or antistatic activity, water repellence, photoluminescence and self-cleaning action brought an extended value that goes beyond the traditional applications [187].

One of the most promising properties of a functional ceramic tile is the self-cleaning feature. A ceramic coated with TiO_2 is able to decompose organics under UV-light. However, self-cleaning will be efficient if the decontamination rate is higher than the contamination [4]. Thus, any increasing in performance will have a positive impact in practical applications. Furthermore, the self-cleaning efficiency is increased in external environments, where the material can be exposed to water flow. In this case, the superhydrophilic property takes place. The low water contact angle creates a thin water film and washes out dusts that cannot be decomposed. Thus, if these two properties work accordingly, the self-cleaning ceramic tile will have higher performance [49].

The photoactivity of TiO_2-coated ceramic tiles has been tested by degradation of dyes, such as methylene blue (MB) [69, 70, 74, 79, 80, 83], orange II [73, 84], rhodamine [78, 79] and crystal violet [79]. Among them, MB is the most tested simultaneously with water contact angle determination [70, 80, 83]. These two properties are

[4] To be submitted for publication.

complementary and give valuable information about the self-cleaning performance.

Sintering of TiO_2-coated ceramic tiles is often made in a second firing process at temperatures from 500 to 900 °C. In most of the cases, when the temperature is increased, the photocatalytic performance decreases. However, sometimes high temperature is necessary to provide a better adhesion of the TiO_2 on the ceramic surface or to follow a common industrial process step, for instance for decoration purposes. The lower PC performance after exposure at higher temperature is usually attributed to the anatase-to-rutile transformation (ART) and to the grain coarsening [80]. Those hindrances would be possibly minimized using an agent that at the same time could postpone ART and grain growth, making it possible to process these products at higher temperature.

Recently, Nb_2O_5-doped-TiO_2 has been investigated for photocatalysis purposes. The introduction of Nb_2O_5 into the TiO_2 lattice can stabilize the nanoparticles postponing ART in about 200 °C, as well as decreasing the grain sizes and consequently increasing the photocatalytic activity [57]. However, photocatalytic studies were performed with titania powder dispersed in water, whose performance might be different than that of a thin film [73].

Thus, the aim of this work is to evaluate the photocatalytic activity of Nb_2O_5-doped TiO_2 coated ceramic tiles. Based on previews results, 5 mol% Nb_2O_5-doped-TiO_2 was chosen as the optimal molar percentage of niobium doping. In addition to degradation of methylene blue, superhydrophilicity of coated ceramic tiles was evaluated.

7.2 Experimental procedures

7.2.1 Materials and sample preparation

Pure TiO_2 and 5 mol% Nb_2O_5-doped TiO_2 (named 5NbTi) transparent colloidal suspensions were prepared by the sol gel process. Titanium (IV) isopropoxide (TTIP, Sigma-Aldrich, ≥ 97%) and niobium butoxide (NB, Alfa Aesar, 99%) were used as Ti and Nb precursors, respectively. For doped samples, TTIP and NB were mixed for 10 min forming a homogeneous solution. No partial pre-hydrolyzation was observed in this step. The solution was then slowly dropped into a mixture of ethanol and diethanolamine. The final solution was mixed for 2 h at room temperature. An optimized

1:5:0.3 volume ratio of TTIP (or TTIP/NB), ethanol to diethanolamine was used.

The transparent colloidal solutions were applied on the surface of industrial glazed ceramic tiles by spraying. The samples were left at room temperature for 10 min and then dried for 10 min at 100 °C before firing. The thermal treatment was carried out in a box furnace at 600, 800 and 900 °C, at 40 °C/min heating rate and for 10 min at the maximum temperature, which simulates a common industrial second firing process.

7.2.2 Characterization

In order to identify the crystalline phases of TiO_2 and 5NbTi powders, a small amount of the colloidal solution was taken, dried at 100 °C for 2 h and calcined at 600, 800 and 900 °C. The oven, heating rate and time at maximum temperature were the same used for sintering the coated ceramic tiles. XRD patterns were acquired using a diffractometer (Bruker D8) in the 20-80° 2θ range, 0.02° scan rate, 16 s per step (LynxEye detector). A Rietveld refinement was carried out with the aid of a software (Topas Version 5, Brucker AXS). Crystal sizes were estimated by the Scherrer equation using a respective software (Diffract.eva Release 2014, Brucker AXS).

The surface microstructure and the coating thickness were investigated by SEM (Leica Cambridge Stereoscan 360). The grain sizes distribution was measured taking the average of 200 measurements using an image treatment software (ImageJ 1.50i).

7.2.3 Self-cleaning measurements

The self-cleaning activity of a ceramic surface is governed by two properties: photocatalytic degradation of organics and superhydrophilicity, which were measured respectively by the water contact angle and the degradation of methylene blue (MB) under UV-light.

The superhydrophilicity property was determined using a tensiometer (OCA 15, Data Physics Instruments). For each sample, it was made 10 measurements at different points on the surface, and the results were expressed as the arithmetic average. The water contact angle of the sample before irradiation was named zero time and was measured in the dark before the experiment. Then, the

samples were irradiated under UV-light (Osram Ultra-Vilalux 300 W, light intensity 20 W/m² in the 300-400 nm range) and the measurements were made every 5-15 min until the angle becomes lower than 5° in average.

The degradation of methylene blue was performed following the ISO 10678:2010 [93]. Firstly, the samples were cleaned with distilled water and dried out at 100 °C for 30 min. Then, the samples were left under UV-radiation (Osram, Ultra-vitalux, 300 W, intensity E = 20 W/m²) for 24 h in order to decompose any possible remaining organic contaminants by photocatalytic oxidation. Then, a 35 mL cylinder was attached on the surface of the samples using silicon glue. The area in contact with the sample was 12.56 cm². In the subsequent step, two identical samples were left in the dark for 24 h with 35 mL of 20 µmol/L aqueous MB solution (conditioning solution) each one. This procedure is necessary because the substrates tend to adsorb the dye molecules. After conditioning, the adsorption solution was replaced by the test solution (35 mL, 10 µmol/L) and the samples were exposed to UV-light (Osram, Ultra-vitalux, 300 W, E = 10 W/m²). The light intensity was measured at the height of the sample underneath the covering glass pane using a UV radiometer (Delta OHM, model HD2302.0 Sonda LP 471 UVA). Thus, the degradation of MB solution was measured every 20 min (up to 3 h) using a spectrophotometer (S-22 UV/Vis, measuring cell length d = 10 mm) by measuring its maximum absorption spectrum at 664 nm wavelength. The reference sample (blank) was kept in the dark and the absorption spectrum was also measured at the same time interval.

The specific degradation rate, R was calculated from Eq. 20.

$$R = \frac{\Delta A_{\lambda} \times V}{\Delta t \times \varepsilon \times d \times A} \tag{20}$$

Where; $\Delta A\lambda$ is the absorption difference from one measurement to another (every 20 min); V is the volume of MB solution; Δt is the time difference; ε is the MB molar extinction coefficient at 664 nm, which is 7402.8 m²/mol; d is the measuring cell length used at the spectrophotometer; and A is the contact area from the MB solution and the catalyst. The degradation rate R of the irradiated and dark

samples makes possible to calculate the specific photocatalytic activity, P_{MB}, by Eq. 21.

$$P_{MB} = R_{irr} - R_{dark} \quad (21)$$

Finally, the photonic efficiency, ζ_{MB}, can be calculated using Eq. 22.

$$\zeta_{MB} = \frac{P_{MB}}{E_p} \times 100 \quad (22)$$

where E_p is the photo UV-radiation intensity.

The results are also reported according to the JIS R 1703-2:2007 [94], expressed by the decomposition activity index, R (μmol/L/min), represented in this paper as MB Index. The absorbance Abs(t) is converted into concentration of MB after t min, C(t), using a conversion factor K. Since the absorbance is proportional to the concentration (Beer's rule), MB concentration was calculated using the MB molar extinction coefficient of ε (664 nm) = 7402.8 m²/mol in aqueous solution at a concentration of 10 ± 0.5 μmol/L [93] as the conversion factor K.

Plotting C(t) as a function of the ultraviolet light irradiation time (min), it is possible to obtain the gradient of the straight line according to the least-squares method. The MB index is then obtained multiplying the gradient by 10^3.

7.3 Results and discussion

The crystalline phases, powder purity and crystallite sizes were analyzed by X-ray diffraction. The results are shown in Fig. 27 and Table 11. XRD patterns of the calcined powders show no sign of contamination. Only anatase and rutile phases are observed in all samples, which attest high powder purity. At 600 °C, pure TiO_2 presents 65 wt% of rutile (JCPDS card n. 86-0147) and 35 wt% of anatase (JCPDS card n. 71-1167). At the same temperature, 5NbTi presents 100 wt% of anatase. The crystallite sizes of TiO_2 were 25 nm for anatase and 33 nm for rutile, while 5NbTi present 8 nm

crystallite sizes in average. At 800 and 900 °C, the anatase-to-rutile phase transition was completed for pure TiO_2. Rutile was the unique phase observed at those temperatures. The sharp peaks seen in the X-ray patterns make evident the formation of bulk samples with larger grain sizes. These values were 56 and 68 nm for 800 and 900 °C, respectively. On the other hand, 5NbTi presented a mix of anatase and rutile phases at 800 °C. Around 38 wt% anatase and 62 wt% rutile, with crystallite sizes of 22 and 25 nm, were respectively obtained. Curiously, the anatase/rutile ratio obtained at 800 °C for 5NbTi and the one obtained at 600 °C for pure TiO_2 was pretty close. This fact confirms the prediction found in the literature that 5 mol% Nb_2O_5-doped TiO_2 is able to postpone the ART in about 200 °C [57, 173]. At 900 °C, ART was also complete for 5NbTi, while the crystallite sizes (45 nm) were still smaller than pure TiO_2 calcined at the same temperature.

It is well reported in the literature that, from the thermodynamic point of view, anatase is more stable than rutile at very small grain sizes [6, 7, 54, 122]. As the grain grows, at a certain size rutile becomes more stable. This critical grain size was determined for pure TiO_2 as 9 to 67 nm, depending on synthesis method, particle morphology, surface stress and purity. During sintering the grain grows, and when the crystal reaches the critical size, the phase transition occurs. Considering that in practice the powders have a size distribution, it is expected that the phase transition happens in an interval of temperature, which allows all particles to reach the critical size and transform into the most stable phase. The presence of Nb_2O_5 on the surface of TiO_2 can both affect the driving forces for particle growth and act as pinning agent limiting the growth rate [57]. Thus, if the TiO_2 grain growth is hampered, the required temperature to ART will be postponed.

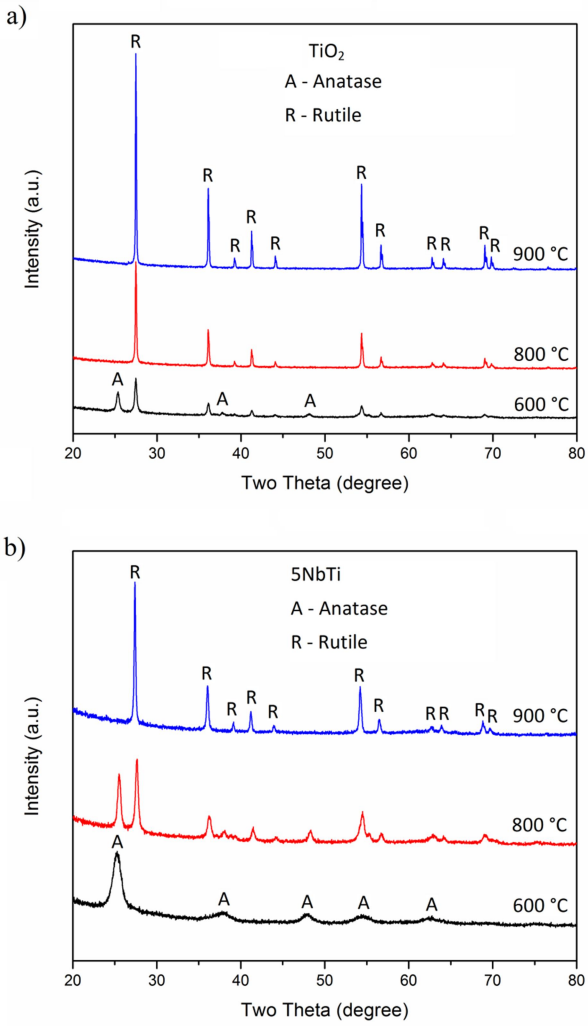

Figure 27. X-ray diffraction patterns of: (a) TiO_2 and (b) 5NbTi, after heat treatment at 600, 800 and 900 °C.

Table 11. Anatase and rutile relative amounts and crystallite sizes.

Sample	Annealing Temperature (°C)	Anatase (wt%)	Anatase crystallite size (nm)	Rutile (wt%)	Rutile crystallite size (nm)
TiO_2	600	35	25	65	33
5NbTi	600	100	8	0	--
TiO_2	800	0	--	100	56
5NbTi	800	38	22	62	25
TiO_2	900	0	--	100	68
5NbTi	900	0	--	100	45

Fig. 28 shows SEM images for TiO_2-coated ceramic tiles and 5NbTi-coated ceramic tiles, both sintered at 800 °C. Comparing the surface microstructure of TiO_2 coating and 5NbTi coating (Figs. 28a and 28b, respectively), a huge difference might be observed between them. The grain size distribution of TiO_2 coating is shown in Fig. 29 and it is in the range of 20 to 120 nm, with average ~65 ± 21 nm (Fig. 29a). On the other hand, 5NbTi coating has shown a grain sizes distribution in a 12 to 40 nm range, with average ~24 ± 5 nm (Fig. 29b). From the catalysis point of view, the advantages are represented by the higher surface area achieved by the doped samples, which provides more active sites for the photocatalytic reaction.

Atanacio *et al*. [129] have shown that niobium has a potential to segregate on the surface of TiO_2. The presence of titanium vacancies, which are formed at the TiO_2/O_2 interface and trapped at the surface, enhances the segregation tendency. Furthermore, the grain size decreasing has been attributed to the surface segregation [134, 141]. If the dopants segregate on the surface of the particles, the surface energies will be significantly affected according to Eq. (23).

$$\gamma = \gamma_0 - \Gamma_i (RT \ln X_i^{bulk} + \Delta H_{seg}) \quad (23)$$

where γ_0 is the surface energy of the pure compound; Γ_i is the surface excess of component *I*; *R* is the constant gas; *T* is the temperature; X_i^{bulk} is the *i* content in the bulk material; and ΔH_{seg} is the enthalpy of segregation of compound *i*.

A nanostructure stability map based on the effect of the enthalpy of segregation on the grain boundary energy has been defined using

Eq. (23). Grain boundary energy is the main driving force for grain growth in addition to the curvature of the interface; therefore, by adding dopants prone to segregate at the boundaries, a stable nanostructure could be achieved inhibiting the grain growth [5]. This theory is supported by the fact that Nb_2O_5-doped TiO_2 anatase has lower surface energy than pure TiO_2, stabilizing the anatase phase and inhibiting the grain growth [188].

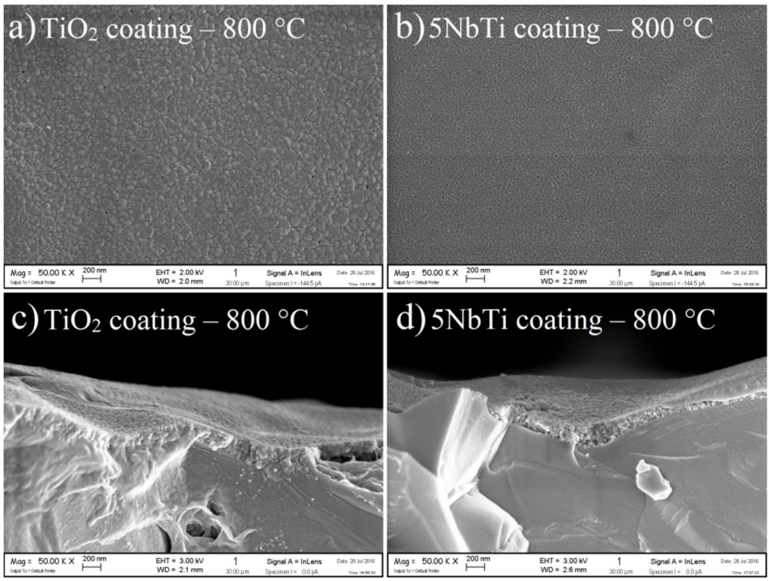

Figure 28. SEM images of coated ceramic tiles sintered at 800 °C: (a) TiO_2 coated ceramic tiles surface. (b) 5NbTi coated ceramic tiles surface. (c) Transversal view of TiO_2 coating. (d) Transversal view of 5NbTi coating.

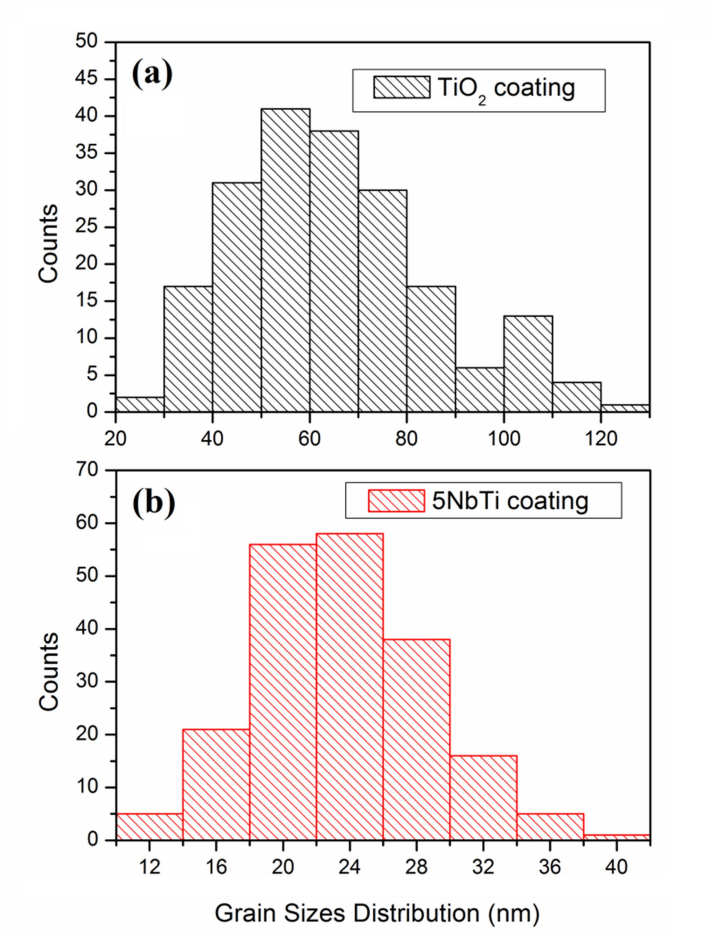

Figure 29. Grain sizes distribution of TiO_2 particles coated on ceramic tiles and sintered at 800 °C: (a) 5NbTi coating. (b) TiO_2 coating.

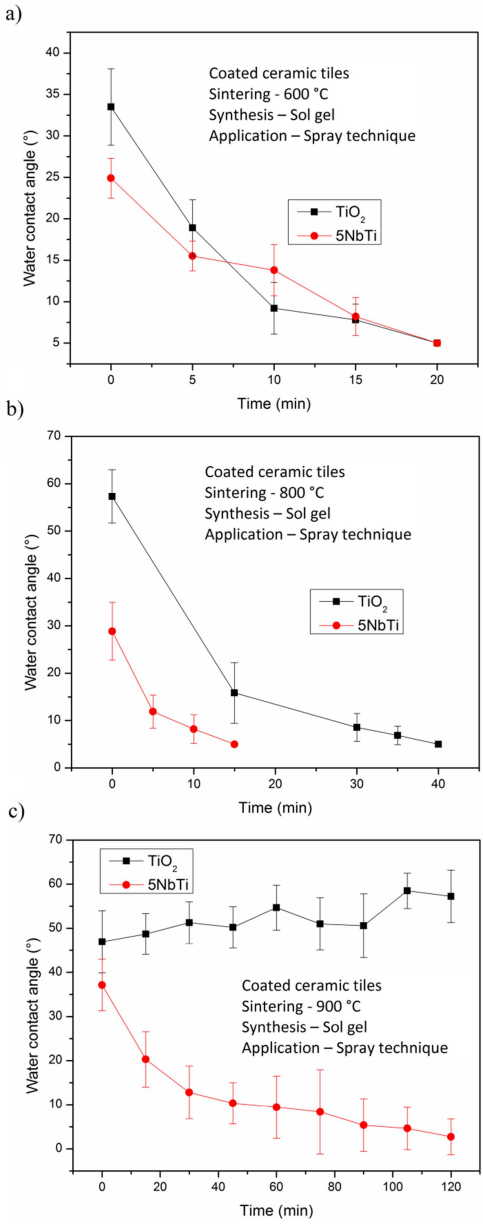

Figure 30. Water contact angle under UV-light irradiation for TiO_2-coated ceramic tiles and 5NbTi-coated ceramic tiles treated at different temperatures: (a) 600 °C. (b) 800 °C. (c) 900 °C.

Fig. 28c and 28d show the cross-section view of the TiO_2-coated ceramic tiles and 5NbTi-coated ceramic tiles, respectively. It is seen that the ceramic surface is not completely flat, but the titania nanoparticles follow the surface imperfection, showing a homogeneous layer. The coating thicknesses were measured taking the average of 16 points from different parts of the tiles. TiO_2 coating presented thickness of 265 ± 56 nm, while 5NbTi coating has shown 223 ± 49 nm thickness. Even though the TiO_2 coating has presented a thickness slightly higher than 5NbTi layers, both values are considered equal because the difference between them is inside the dispersion error. In fact, the thickness obtained in this work can be considered very low and it is attributed to the deposition method. According to the data available in the literature, spray technique provides thickness from 0.1 to 3.0 μm [74, 79, 81], while other methods go much higher; for instance, ink jet printing and roller printing reach thicknesses of ~70 μm and ~100 μm [70], respectively. The advantages of having a thin layer are not just related to a very small amount of powders. A transparent thin film formed by TiO_2 nanoparticles can give remarkable photocatalytic properties and at the same time preserves the original characteristics of the ceramic tiles.

Fig. 30 shows the water contact angle for TiO_2 and 5NbTi -coated ceramic tiles sintered at 600 °C (Fig. 30a), 800 °C (Fig. 30b) and 900 °C (Fig. 30c). At 600 °C, both samples presented water contact angle <5° in just 20 min. No difference in terms of performance is observed between the samples at this temperature. At 800 °C, TiO_2 coating reaches the superhydrophilicity in ~40 min. However, at the same temperature, 5NbTi got a water contact angle <5° in just 15 min, which is the best result regarding to superhydrophilicity in this work. At 900 °C, TiO_2 coating has not shown any decreasing in water contact angle. Even though the angle is increasing along the 2 h-test, the angles can be considered the same, because they are inside the standard deviation. On the other hand, 5NbTi coated ceramic tiles treated at 900 °C were still active, reaching water contact angle <5° after 2 h.

The specific photocatalytic activity, P_{MB}, is shown in Fig. 31. Table 13 shows the absolute values for P_{MB}, photonic efficiency (ζ_{MB}) and MB index. The P_{MB} and ζ_{MB} are the standard representation of photoactivity according to ISO 10.678:2010 [93] and the MB index is the standard photocatalytic representation

according to JIS R 1703-2:2007 [94]. The trend is similar regardless the method used. It is clearly observed that the 5NbTi coating presents higher photocatalytic activity than TiO_2 in all temperatures tested. The higher performance though was achieved at 600 °C. Overall, the photoactivity decreases as the temperature increases for both samples, making evident the effect of the grain growth and phase transition. Observing TiO_2 coating fired at 600 °C and 5NbTi coating sintered at 800 °C, it is seen that both samples presented similar performance. Coincidently, these samples presented practically the same anatase/rutile ratio, which makes evident the benefits of the ART postpone. For the ceramic tiles industries, this is very important; since the doped samples allow the sintering at higher temperature, without impair performance. The presence of rutile phase together with anatase phase can be beneficial since it promotes the electron transport to the conduction band of rutile phase, which is adjacent to anatase phase, decreasing the recombination rate. Thus, the presence of rutile phase acts as a defect or impurity, causing higher photocatalytic activity [172]. At 900 °C, the photoactivity of TiO_2 coating was very low, not being considered photoactive anymore. On the other hand, 5NbTi was still active, proving the effect caused by Nb_2O_5 doping on TiO_2 nanoparticles.

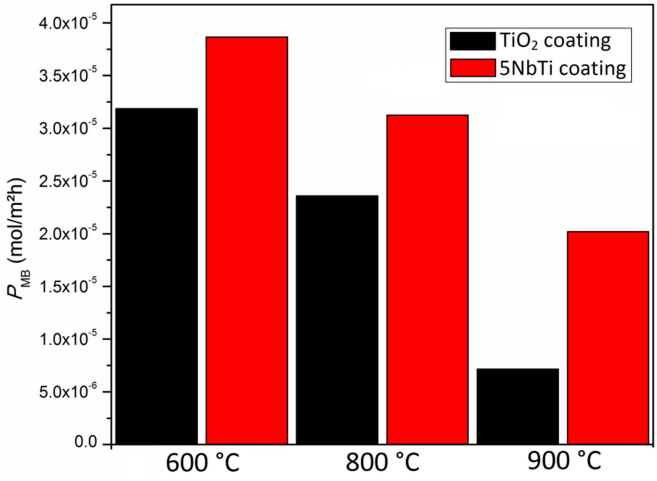

Figure 31. Specific photocatalytic activity (P_{MB}) for TiO_2-coated ceramic tiles and 5NbTi coated ceramic tiles sintered at 600, 800 and 900 °C.

Table 12. Specific photocatalytic activity (P_{MB}), photonic efficiency (ζ_{MB}) and MB Index (JIS R 1703-2:2007.

Sample	Temperature (°C)	P_{MB} (mol/m^2*h)	ζ_{MB} (%)	MB Index
TiO_2 coating	600	3.19E-05	0.0296	18.6
5NbTi coating	600	3.86E-05	0.0359	23.3
TiO_2 coating	800	2.36E-05	0.0223	14.7
5NbTi coating	800	3.12E-05	0.0293	18.7
TiO_2 coating	900	0.72E-05	0.0067	3.8
5NbTi coating	900	2.02E-05	0.0188	11.9

One of the facts responsible for the higher performance of 5NbTi coating comparing to pure TiO_2 coating is the smaller grain size achieved by the doped samples. The small grains provide higher surface area, which means more active sites for the reaction. However, in our previous work [57], we have shown that even considering the same surface area, the samples doped with Nb_2O_5 presented higher photocatalytic activity than pure TiO_2.

The ionic radius of Nb^{5+} is 0.64 Å, which is slightly larger than Ti^{4+} (0.605 Å). Hence, when TiO_2 is doped with Nb_2O_5, Nb^{5+} can form a solid solution in the TiO_2 lattice. The compensation of the excess charge of Nb^{5+} in substitution to Ti^{4+} can be explained by Eq. (24) and Eq. (25). The first possibility is the creation of Ti^{4+} cation vacancy for every 4 Nb^{5+} cations. Another option is the reduction of Ti^{4+} to Ti^{3+} for every Nb^{5+} incorporated, where O^{2-} is oxidized [168, 183, 184]. The reduction is less energetic than vacancy formation. Thus, from the thermodynamic point of view, Eq. (25) is more favorable. The presence of active Ti^{3+} sites on the surface could act as sites for trapping photogenerated electrons that could effectively inhibit the recombination of photoinduced electrons and holes [186].

$$\frac{1}{2}Nb_2O_5 \xrightarrow{TiO_2} Nb_{Ti}^{\cdot} + \frac{1}{4}V_{Ti}^{''''} + \frac{5}{2}O_O^X \tag{24}$$

$$\frac{1}{2}Nb_2O_5 \xrightarrow{TiO_2} Nb_{Ti}^{\cdot} + Ti^{(3+)'}_{Ti^{(4+)}} + 2O_O^X + \frac{1}{4}O_2 \tag{25}$$

In addition, Nb-doped TiO_2 can present better charge separation. Nb-doping introduces shallow donor levels below the CB edge, which can act as electron traps to retard electron-hole recombination, thus the lifetime of photogenerated electrons and holes can be increased and consequently the photocatalytic efficiency is enhanced [168]. Moreover, the Nb_2O_5 itself shows high photocatalytic decomposition of methylene blue [182]. Considering that Nb_2O_5 has a potential to segregate on the surface of TiO_2 [129], the major part of Nb_2O_5 doping is on the surface of the TiO_2, which could explain the photoactivity achieved at 900 °C for 5NbTi even if at that temperature the anatase-to-rutile phase transition is completed.

7.4 Conclusions

Photocatalytic ceramic tiles were successfully produced by coating 5 mol% Nb_2O_5-doped TiO_2 using spraying. The film thickness was ~250 nm, which is very low and makes possible to produce photocatalytic ceramic tiles using a very low amount of nanopowder. X-ray diffraction of the powders showed only anatase and rutile crystalline phases. No sign of second phase was detected. The SEM images have shown the grain size stabilization of the doped samples. At 800 °C, TiO_2 coating presented grain sizes of ~64.8 nm in average, while 5NbTi, ~23.6 nm. The photocatalytic performance of doped samples was higher at all temperatures tested. Even at 900 °C, the coated samples were photoactive, while the undoped samples were not photoactive anymore. The MB degradation was performed using international standards, which makes easier performance comparisons of future studies.

8. FINAL CONCLUSIONS

The main conclusions of this thesis are:

- A predictive anatase-rutile phase transition diagram was built at nanoscale for Nb_2O_5-doped TiO_2. Nb_2O_5-doping postpone ART, allowing the anatase grains to grow more than undoped TiO_2 before phase transition is observed. The stability crossover for undoped TiO_2 was found to be 17.3 nm, while 2 mol% Nb_2O_5-doped TiO_2 crossover is ~30 nm.
- The surface energy for Nb_2O_5-doped TiO_2 decreases systematically as the Nb concentration increases (from 0-2 mol% Nb_2O_5 doping), confirming the higher stability for doped samples.
- 5 mol% Nb_2O_5-doped TiO_2 nanopowder synthesized by simultaneous precipitation can postpone the ART of the powders in ~200 °C.
- The crystallite sizes decrease and the specific surface area increases with higher doping concentration at the same temperature (0-5 mol% Nb_2O_5-doped TiO_2).
- Nb_2O_5-doped TiO_2 samples present higher photocatalytic activity by degradation of methylene blue than pure TiO_2 synthesized at the same condition under UV and visible light. The powders containing 5 mol% Nb_2O_5-doped TiO_2 presented similar photoactivity under UV-light and higher photoactivity than P25 under visible light.
- Photocatalytic ceramic tiles were successfully produced applying TiO_2 sol by spraying. The film thickness was ~250 nm, which makes possible the use of nanopowders, obtaining high performance with a low amount of powders.
- Photocatalytic ceramic tiles coated with 5 mol% Nb_2O_5-doped TiO_2 presented higher degradation rate of methylene blue solution and faster water contact angle decrease under UV-light than pure TiO_2.
- The use of Nb_2O_5-doped TiO_2 coated ceramic tiles makes possible the production of photoactive ceramic tiles at higher temperature, which is not achieved by applying pure TiO_2

coating. At 900 °C, the ceramic tiles coated by doped samples were still photoactive, while the ones coated by pure TiO_2 were not photoactive anymore.

REFERENCES

1. Hanaor, D.A.H. and Sorrell, C.C., *Review of the anatase to rutile phase transformation.* Journal of Materials Science, 2010. **46**(4): p. 855-874.

2. Fujishima, A. and Honda, K., *Electrochemical Photolysis of Water at a Semiconductor Electrode.* Nature, 1972. **238**(5358): p. 37-38.

3. Chen, X. and Mao, S.S., *Titanium Dioxide Nanomaterials: Synthesis, Properties, Modifications, and Applications.* Chemical Reviews, 2007. **107**(7): p. 2891-2959.

4. Fujishima, A., Zhang, X. and Tryk, D.A., *TiO_2 photocatalysis and related surface phenomena.* Surface Science Reports, 2008. **63**(12): p. 515-582.

5. Castro, R.H.R., *On the thermodynamic stability of nanocrystalline ceramics.* Materials Letters, 2013. **96**: p. 45-56.

6. Levchenko, A.A., Li, G., Boerio-Goates, J., Woodfield, B.F. and Navrotsky, A., *TiO_2 Stability Landscape: Polymorphism, Surface Energy, and Bound Water Energetics.* Chemistry of Materials, 2006. **18**(26): p. 6324-6332.

7. Castro, R.H.R. and Wang, B., *The Hidden Effect of Interface Energies in the Polymorphic Stability of Nanocrystalline Titanium Dioxide.* Journal of the American Ceramic Society, 2011. **94**(3): p. 918-924.

8. McMurry, J.E. and Fay, R.C., *General Chemistry: Atoms First*. 5th ed. 2010, Trenton, New Jersey: Pearson/Prentice Hall.

9. Gázquez, M.J., Bolívar, J.P., Garcia-Tenorio, R. and Vaca, F. , *A Review of the Production Cycle of Titanium Dioxide Pigment.* Materials Science and Applications, 2014. **5**: p. 441-458.

10. Li, Z., Wang, Z. and Li, G., *Preparation of nano-titanium dioxide from ilmenite using sulfuric acid-decomposition by liquid phase method.* Powder Technology, 2016. **287**: p. 256-263.

11. Wojciechowski, K., Zukowska, G.Z., Korczagin, I. and Malanowski, P., *Effect of TiO_2 on UV stability of polymeric binder films used in waterborne facade paints.* Progress in Organic Coatings, 2015. **85**: p. 123-130.

12. Weir, A., Westerhoff, P., Fabricius, L., Hristovski, K. and von Goetz, N., *Titanium Dioxide Nanoparticles in Food and Personal Care Products.* Environmental Science & Technology, 2012. **46**(4): p. 2242-2250.

13. Kockler, J., Oelgemöller, M., Robertson, S. and Glas, B.D., *Photostability of sunscreens.* Journal of Photochemistry and Photobiology C: Photochemistry Reviews, 2012. **13**(1): p. 91-110.

14. Newman, M.D., Stotland, M. and Ellis, J.I., *The safety of nanosized particles in titanium dioxide– and zinc oxide–based sunscreens.* Journal of the American Academy of Dermatology, 2009. **61**(4): p. 685-692.

15. Grätzel, M., *Dye-sensitized solar cells.* Journal of Photochemistry and Photobiology C: Photochemistry Reviews, 2003. **4**(2): p. 145-153.

16. Ali, N., Hussain, A., Ahmed, R., Wang, M.K., Zhao, C., Haq, B.U. and Fu, Y.Q., *Advances in nanostructured thin film materials for solar cell applications.* Renewable and Sustainable Energy Reviews, 2016. **59**: p. 726-737.

17. Song, Q., Zhu, Y., Zheng, H., Zhang, F. and Wu, M., *Fabricating TiO_2 film with a facile spray-coating technique for dye-sensitized solar cells.* Materials & Design, 2016. **98**: p. 108-112.

18. Nakata, K. and Fujishima, A., *TiO_2 photocatalysis: Design and applications.* Journal of Photochemistry and Photobiology C: Photochemistry Reviews, 2012. **13**(3): p. 169-189.

19. Drelich, J. and Chibowski, E., *Hydrophilic and superhydrophilic surfaces and materials.* Soft Matter, 2011. **7**(21): p. 9804-9828.

20. Fujishima, A., Rao, T.N. and Tryk, D.A., *Titanium dioxide photocatalysis.* Journal of Photochemistry and Photobiology C: Photochemistry Reviews, 2000. **1**(1): p. 1-21.

21. Zhao, J., Chen, C. and Ma, W., *Photocatalytic Degradation of Organic Pollutants Under Visible Light Irradiation.* Topics in Catalysis, 2005. **35**(3): p. 269-278.

22. Yu, J.C., Yu, J., Ho, W., Jiang, Z. and Zhang, L., *Effects of F^- Doping on the Photocatalytic Activity and Microstructures of Nanocrystalline TiO_2 Powders.* Chemistry of Materials, 2002. **14**(9): p. 3808-3816.

23. Ovenstone, J., *Preparation of novel titania photocatalysts with high activity.* Journal of Materials Science, 2001. **36**(6): p. 1325-1329.

24. Hirano, M., Nakahara, C., Ota, K., Tanaike, O. and Inagaki, M., *Photoactivity and phase stability of ZrO_2-doped anatase-type TiO_2 directly formed as nanometer-sized particles by hydrolysis under hydrothermal conditions.* Journal of Solid State Chemistry, 2003. **170**(1): p. 39-47.

25. Beltrán, A., Gracia, L., and Andrés, J., *Density Functional Theory Study of the Brookite Surfaces and Phase Transitions between Natural Titania Polymorphs.* The Journal of Physical Chemistry B, 2006. **110**(46): p. 23417-23423.

26. Fox, M.A. and Dulay, M.T., *Heterogeneous photocatalysis.* Chemical Reviews, 1993. **93**(1): p. 341-357.

27. Sclafani, A. and Herrmann, J.M., *Comparison of the Photoelectronic and Photocatalytic Activities of Various Anatase and Rutile Forms of Titania in Pure Liquid Organic Phases and in Aqueous Solutions.* The Journal of Physical Chemistry, 1996. **100**(32): p. 13655-13661.

28. Xu, N., Shi, Z., Fan, Y., Dong, J., Shi, J., Hu, M. Z.C., *Effects of Particle Size of TiO_2 on Photocatalytic Degradation of Methylene Blue in Aqueous Suspensions.* Industrial & Engineering Chemistry Research, 1999. **38**(2): p. 373-379.

29. Wang, C.-C., Zhang, Z. and Ying, J.Y., *Photocatalytic decomposition of halogenated organics over nanocrystalline titania.* Nanostructured Materials, 1997. **9**(1–8): p. 583-586.

30. Zhang, Z., Wang, C-C., Zakaria, R. and Ying, J.Y., *Role of Particle Size in Nanocrystalline TiO_2-Based Photocatalysts.* The Journal of Physical Chemistry B, 1998. **102**(52): p. 10871-10878.

31. Wilke, K. and Breuer, H.D., *The influence of transition metal doping on the physical and photocatalytic properties of titania.* Journal of Photochemistry and Photobiology A: Chemistry, 1999. **121**(1): p. 49-53.

32. Yang, L. and Liu, Z., *Study on light intensity in the process of photocatalytic degradation of indoor gaseous formaldehyde for saving energy.* Energy Conversion and Management, 2007. **48**(3): p. 882-889.

33. Gaya, U.I. and Abdullah, A.H., *Heterogeneous photocatalytic degradation of organic contaminants over titanium dioxide: A review of fundamentals, progress and problems.* Journal of Photochemistry and Photobiology C: Photochemistry Reviews, 2008. **9**(1): p. 1-12.

34. Reszczyńska, J., Grzyb, T., Sobczak, J.W., Lisowski, W., Gazda, M., Ohtani, B. and Zaleska, A., *Lanthanide co-doped TiO_2: The effect of metal type and amount on surface properties and photocatalytic activity.* Applied Surface Science, 2014. **307**: p. 333-345.

35. Reszczyńska, J., Grzyb, T., Sobczak, J.W., Lisowski, W., Gazda, M., Ohtani, B. and Zaleska, A., *Visible light activity of rare earth metal doped (Er^{3+}, Yb^{3+} or Er^{3+}/Yb^{3+}) titania photocatalysts.* Applied Catalysis B: Environmental, 2015. **163**: p. 40-49.

36. Liang, C.-H., Li, F.-B., Liu, C.-S., Lu, J.-L. and Wang, X.-G. *The enhancement of adsorption and photocatalytic activity of rare earth ions doped TiO_2 for the degradation of Orange I.* Dyes and Pigments, 2008. **76**(2): p. 477-484.

37. Asiltürk, M., Sayılkan, F. and Arpaç, E., *Effect of Fe^{3+} ion doping to TiO_2 on the photocatalytic degradation of Malachite Green dye under UV and vis-irradiation.* Journal of Photochemistry and Photobiology A: Chemistry, 2009. **203**(1): p. 64-71.

38. Todorova, N., Vaimakis, T., Petrakis, D., Hishita, S., Boukos, N., Giannakopoulou, T., Giannouri, M., Antiohos, S., Papageorgiou, D., Chaniotakis, E. and Trapalis, C., *N and N,S-doped TiO_2 photocatalysts and their activity in NOx oxidation.* Catalysis Today, 2013. **209**: p. 41-46.

39. Chai, Y., Lin, L., Zhang, K., Zhao, B. and He, D., *Efficient visible-light photocatalysts from Gd–La codoped TiO_2 nanotubes.* Ceramics International, 2014. **40**(2): p. 2691-2696.

40. Choi, W., Termin, A., and Hoffmann, M.R., *The Role of Metal Ion Dopants in Quantum-Sized TiO_2: Correlation between Photoreactivity and Charge Carrier Recombination Dynamics.* The Journal of Physical Chemistry, 1994. **98**(51): p. 13669-13679.

41. Ruiz, A.M., Dezanneau, G., Arbiol, J., Cornet, A. and Morante, J.R., *Insights into the Structural and Chemical Modifications of Nb Additive on TiO_2 Nanoparticles.* Chemistry of Materials, 2004. **16**(5): p. 862-871.

42. Di Valentin, C., Pacchioni, G. and Selloni, A., *Reduced and n-Type Doped TiO_2: Nature of Ti^{3+} Species.* The Journal of Physical Chemistry C, 2009. **113**(48): p. 20543-20552.

43. Justicia, I., Ordejón, P., Canto, G., Mozos, J.L., Fraxedas, J., Battiston, G.A., Gerbasi, R. and Figueras, A., *Designed Self-Doped Titanium Oxide Thin Films for Efficient Visible-Light Photocatalysis.* Advanced Materials, 2002. **14**(19): p. 1399-1402.

44. Castro, A.L., Nunes, M.R., Carvalho, M.D., Ferreira, L.P., Jumas, J.C., Costa, F.M. and Florêncio, M.H., *Doped titanium dioxide nanocrystalline powders with high photocatalytic activity.* Journal of Solid State Chemistry, 2009. **182**(7): p. 1838-1845.

45. Lim, J., Monllor-Satoca, D., Jang, J.S., Lee, S. and Choi, W., *Visible light photocatalysis of fullerol-complexed TiO_2 enhanced by Nb doping.* Applied Catalysis B: Environmental, 2014. **152–153**: p. 233-240.

46. Asahi, R., Morikawa, T., Ohwaki, T., Aoki, K. and Taga, Y., *Visible-Light Photocatalysis in Nitrogen-Doped Titanium Oxides.* Science, 2001. **293**(5528): p. 269-271.

47. Horovitz, I., Avisar, D., Baker, M.A., Grilli, R., Lozzi, L., Di Camillo, D. and Mamane, H., *Carbamazepine degradation using a N-doped TiO_2 coated photocatalytic membrane reactor: Influence of physical parameters.* Journal of Hazardous Materials, 2016. **310**: p. 98-107.

48. Feng, X., Zhai, J. and Jiang, L., *The Fabrication and Switchable Superhydrophobicity of TiO_2 Nanorod Films.* Angewandte Chemie International Edition, 2005. **44**(32): p. 5115-5118.

49. Wang, R., Hashimoto, K., Fujishima, A., Chikumi, M., Kojima, E., Kitamura, A., Shimohigoshi, M. and Watanabe, T., *Photogeneration of Highly Amphiphilic TiO_2 Surfaces.* Advanced Materials, 1998. **10**(2): p. 135-138.

50. Fujishima, A. and Zhang, X., *Titanium dioxide photocatalysis: present situation and future approaches.* Comptes Rendus Chimie, 2006. **9**(5–6): p. 750-760.

51. Léonard, G.L.M., Remy, S. and Heinrichs, B., *Overview of Superhydrophilic, Photocatalytic and Anticorrosive Properties of TiO_2 Thin Films Doped with Multi-walled Carbon Nanotubes and Deposited on 316L Stainless Steel.* Materials Today: Proceedings, 2016. **3**(2): p. 434-438.

52. Shi, H., He, Y., Pan, Y., Di, H., Zeng, G., Zhang, L. and Zhang, C., *A modified mussel-inspired method to fabricate TiO_2 decorated superhydrophilic PVDF membrane for oil/water separation.* Journal of Membrane Science, 2016. **506**: p. 60-70.

53. Kaplan, R., Erjavec, B., Dražić, G., Grdadolnik, J. and Pintar, A., *Simple synthesis of anatase/rutile/brookite TiO_2 nanocomposite with superior mineralization potential for photocatalytic degradation of water pollutants.* Applied Catalysis B: Environmental, 2016. **181**: p. 465-474.

54. Zhang, H. and Banfield, J.F., *Thermodynamic analysis of phase stability of nanocrystalline titania.* Journal of Materials Chemistry, 1998. **8**(9): p. 2073-2076.

55. Ohno, T., Sarukawa, K. and Matsumura, M., *Photocatalytic Activities of Pure Rutile Particles Isolated from TiO_2 Powder by Dissolving the Anatase Component in HF Solution.* The Journal of Physical Chemistry B, 2001. **105**(12): p. 2417-2420.

56. Ohno, T., Tokieda, K., Higashida, S. and Matsumura, M., *Synergism between rutile and anatase TiO_2 particles in photocatalytic oxidation of naphthalene.* Applied Catalysis A: General, 2003. **244**(2): p. 383-391.

57. da Silva, A.L., Muche, D.N.F., Dey, S., Hotza, D. and Castro, R. H.R., *Photocatalytic Nb_2O_5-doped TiO_2 nanoparticles for glazed ceramic tiles.* Ceramics International, 2016. **42**(4): p. 5113-5122.

58. Clegg, I.M., Everall, N., King, B., Melvin, H. and Norton, C., *On-Line Analysis Using Raman Spectroscopy for Process Control during the Manufacture of Titanium Dioxide.* Applied Spectroscopy, 2001. **55**(9): p. 1138-1150.

59. Suresh, C., Biju, V., Mukundan, P., Warrier, K.G.K., *Anatase to rutile transformation in sol-gel titania by modification of precursor.* Polyhedron, 1998. **17**(18): p. 3131-3135.

60. Okada, K., Yamamoto, N., Kameshima, Y., Yasumori, A. and Mackenzie, K.J.D., *Effect of Silica Additive on the Anatase-to-Rutile Phase Transition.* Journal of the American Ceramic Society, 2001. **84**(7): p. 1591-1596.

61. Batzill, M., Morales, E.H. and Diebold, U., *Influence of Nitrogen Doping on the Defect Formation and Surface Properties of TiO_2 Rutile and Anatase.* Physical Review Letters, 2006. **96**(2): p. 026103.

62. Toyoda, M., Nanbu, Y., Nakazawa, Y., Hirano, M. and Inagaki, M., *Effect of crystallinity of anatase on photoactivity for methyleneblue decomposition in water.* Applied Catalysis B: Environmental, 2004. **49**(4): p. 227-232.

63. Gennari, F.C. and Pasquevich, D.M., *Kinetics of the anatase–rutile transformation in TiO_2 in the presence of Fe_2O_3.* Journal of Materials Science, 1998. **33**(6): p. 1571-1578.

64. Pan, Z., Wang, Y., Huang, H., Ling, Z., Dai, Y. and Ke, S., *Recent development on preparation of ceramic inks in ink-jet printing.* Ceramics International, 2015. **41**(10, Part A): p. 12515-12528.

65. da Silva, A.L., Feltrin, J., Dal Bó, M., Bernardin, A.M. and Hotza, D., *Effect of reduction of thickness on microstructure and properties of porcelain stoneware tiles.* Ceramics International, 2014. **40**(9, Part B): p. 14693-14699.

66. da Silva, A.L., Bernardin, A.M. and Hotza, D., *Forming of thin porcelain tiles: A comparison between tape casting and dry pressing.* Ceramics International, 2014. **40**(2): p. 3761-3767.

67. Berto, A.M., *Ceramic tiles: Above and beyond traditional applications.* Journal of the European Ceramic Society, 2007. **27**(2–3): p. 1607-1613.

68. Murugan, K., Subasri, R., Rao, T.N., Gandhi, A.S. and Murty, B.S., *Synthesis, characterization and demonstration of self-cleaning TiO_2 coatings on glass and glazed ceramic tiles.* Progress in Organic Coatings, 2013. **76**(12): p. 1756-1760.

69. Ducman, V., Petrovič, V. and Škapin, S.D., *Photo-catalytic efficiency of laboratory made and commercially available ceramic building products.* Ceramics International, 2013. **39**(3): p. 2981-2987.

70. Raimondo, M., Guarini, G., Zanelli, C., Marani, F., Fossa, L. and Dondi, M., *Printing nano TiO_2 on large-sized building materials: Technologies, surface modifications and functional behaviour.* Ceramics International, 2012. **38**(6): p. 4685-4693.

71. Sun, S.-Q., Sun, B., Zhang, W. and Wang, D., *Preparation and antibacterial activity of Ag-TiO_2 composite film by liquid phase deposition (LPD) method.* Bulletin of Materials Science, 2008. **31**(1): p. 61-66.

72. Marcos, P.S., Marto, J., Trindade, T. and Labrincha, J.A., *Screen-printing of TiO_2 photocatalytic layers on glazed ceramic tiles.* Journal of Photochemistry and Photobiology A: Chemistry, 2008. **197**(2–3): p. 125-131.

73. Seabra, M.P., Pires, R.R. and Labrincha, J.A., *Ceramic tiles for photodegradation of Orange II solutions.* Chemical Engineering Journal, 2011. **171**(2): p. 692-702.

74. Ke, S., Cheng, X., Wang, Q., Wang, Y. and Pan, Z., *Preparation of a photocatalytic $TiO_2/ZnTiO_3$ coating on glazed ceramic tiles.* Ceramics International, 2014. **40**(6): p. 8891-8895.

75. Hasmaliza, M., Foo, H.S. and Mohd, K., *Anatase as Antibacterial Material in Ceramic Tiles.* Procedia Chemistry, 2016. **19**: p. 828-834.

76. Kuisma, R., Fröberg, L., Kymäläinen, H.-R., Pesonen-Leinonen, E., Piispanen, M., Melamies, P., Hautala, M., Sjöberg, A.-M. and Hupa, L., *Microstructure and cleanability of uncoated and fluoropolymer, zirconia and titania coated ceramic glazed surfaces.* Journal of the European Ceramic Society, 2007. **27**(1): p. 101-108.

77. Määttä, J., Piispanen, M., Kymäläinen, H.R., Uusi-Rauva, A., Hurme, K.R., Areva, S., Sjöberg, A.M. and Hupa, L., *Effects of UV-radiation on the cleanability of titanium dioxide-coated glazed ceramic tiles.* Journal of the European Ceramic Society, 2007. **27**(16): p. 4569-4574.

78. Kemmitt, T., Al-Salin, N.I., Waterland, M., Kennedy, V.J. and Markwitz, A., *Photocatalytic titania coatings.* Current Applied Physics, 2004. **4**(2-4): p. 189-192.

79. Petrovič, V., Ducman, V. and Škapin, S.D., *Determination of the photocatalytic efficiency of TiO_2 coatings on ceramic tiles by monitoring the photodegradation of organic dyes.* Ceramics International, 2012. **38**(2): p. 1611-1616.

80. Tezza, V.B., Scarpato, M., Oliveira, L.F.S. and Bernardin, A.M., *Effect of firing temperature on the photocatalytic activity of anatase ceramic glazes.* Powder Technology, 2015. **276**: p. 60-65.

81. Bondioli, F., Taurino, R. and Ferrari, A.M., *Functionalization of ceramic tile surface by sol–gel technique.* Journal of Colloid and Interface Science, 2009. **334**(2): p. 195-201.

82. Niederhãusern, S., Bondi, M. and Bondioli, F., *Self-Cleaning and Antibacteric Ceramic Tile Surface.* International Journal of Applied Ceramic Technology, 2013. **10**(6): p. 949-956.

83. Sciancalepore, C. and Bondioli, F., *Durability of SiO_2–TiO_2 Photocatalytic Coatings on Ceramic Tiles.* International Journal of Applied Ceramic Technology, 2015. **12**(3): p. 679-684.

84. Rego, E., Marto, J., Marcos, P.S. and Labrincha, J.A., *Decolouration of Orange II solutions by TiO_2 and ZnO active layers screen-printed on ceramic tiles under sunlight irradiation.* Applied Catalysis A: General, 2009. **355**(1–2): p. 109-114.

85. Ruiz O., Sanmiguel, F., Gargori, C., Galindo, F. and Monrós, G., *Estudo da Capacidade de Degradação Fotocatalítica de Vidrados Cerâmicos.* Cerâmica Industrial, 2009. **14** p. 7-14.

86. Montorsi, M., Mugoni, C., Passalacqua, A., Annovi, A., Marani, F., Fossa, L., Capitani, R. and Manfredini, T., *Improvement of color quality and reduction of defects in the ink jet-printing technology for ceramic tiles production: A Design of Experiments study.* Ceramics International, 2016. **42**(1, Part B): p. 1459-1469.

87. Fassier, M., Chouard, N., Peyratout, C.S., Smith, D.S., Riegler, H., Kurth, D.G., Ducroquetz, C. and Bruneaux, M.A., *Photocatalytic activity of oxide coatings on fired clay substrates.* Journal of the European Ceramic Society, 2009. **29**(4): p. 565-570.

88. Elyseu, F. and Bernardin, A.M., *Tonality variation in ceramic tile silkscreen decoration: Effect of ink density and mesh opening gradient.* Dyes and Pigments, 2012. **95**(2): p. 427-430.

89. Dondi, M., Ercolani, G., Guarini, G., Melandri, C., Raimondo, M., Rocha e Almendra, E. and Tenorio Cavalcante, P.M., *The role of surface microstructure on the resistance to stains of porcelain stoneware tiles.* Journal of the European Ceramic Society, 2005. **25**(4): p. 357-365.

90. 10545-14, E.I., *Ceramic tiles. Part 14. Determination of resistance to stains*. 2000.

91. Mellott, N.P., Durucan, C., Pantano, C.G. and Guglielmi, M., *Commercial and laboratory prepared titanium dioxide thin films for self-cleaning glasses: Photocatalytic performance and chemical durability.* Thin Solid Films, 2006. **502**(1–2): p. 112-120.

92. UNI-EN_1096-2, *Glass in building. Coated glass. Requirements and test methods for class A, B and S coating.* 2002.

93. ISO, *International Standard ISO 10678-Fine Ceramics (Advanced Technical Ceramics) - Determination of Photocatalytic Activity of Surfaces in an Aqueous Medium by Degradation of Methylene Blue.* . 2010.

94. *JIS R 1703-2 Fine ceramics (advanced ceramics, advanced technical ceramics) - Test method for self-cleaning performance of photocatalytic materials - Part 2: Decomposition of wet methylene blue*. 2007.

95. ISO, *International Standard 27448 Fine ceramics (advanced ceramics, advanced technical ceramics) - Test method for self-cleaning performance of semiconducting photocatalytic materials - Measurement of water contact angle.* 2009.

96. *JIS Z 2801, Antibacterial products - Test for antibacterial activity and efficacy*. 2010.

97. Rabenau, A., *The Role of Hydrothermal Synthesis in Preparative Chemistry.* Angewandte Chemie International Edition in English, 1985. **24**(12): p. 1026-1040.

98. Liu, J., Duan, Y., Zhou, X. and Lin, Y., *Influence of VB group doped TiO_2 on photovoltaic performance of dye-sensitized solar cells.* Applied Surface Science, 2013. **277**: p. 231-236.

99. Palmero, P., *Structural Ceramic Nanocomposites: A Review of Properties and Powders' Synthesis Methods.* Nanomaterials, 2015. **5**(2): p. 656.

100. Krishnakanth, R., Jayakumar, G., Albert Irudayaraj, A. and Dhayal Raj, A., *Structural and Magnetic Properties of NiO and Fe-doped NiO Nanoparticles Synthesized by Chemical Co-precipitation Method.* Materials Today: Proceedings, 2016. **3**(6): p. 1370-1377.

101. Parsa, M.H., Zamani, C., Babaei, A., Sheibani, S., Soleimanzadeh, H., Niaei, A., Salari, D., Mousavi, S.M. and Tarjamannejad, A., *5th International Biennial Conference on Ultrafine Grained and Nanostructured Materials, UFGNSM15Performance Study f V_2O_5/TiO_2 Mixed Metal Oxide Nanocatalysts in Selective Catalytic Reduction of Nox Prepared by Co-Precipitation Method.* Procedia Materials Science, 2015. **11**: p. 655-660.

102. Pazhanivelu, V., Selvadurai, A.P.B., Kannan, R. and Murugaraj, R., *Room temperature ferromagnetism in Ist group elements codoped ZnO:Fe nanoparticles by co-precipitation method.* Physica B: Condensed Matter, 2016. **487**: p. 102-108.

103. Farhadi, S. and Panahandehjoo, S., *Spinel-type zinc aluminate ($ZnAl_2O_4$) nanoparticles prepared by the co-precipitation method: A novel, green and recyclable heterogeneous catalyst for the acetylation of amines, alcohols and phenols under solvent-free conditions.* Applied Catalysis A: General, 2010. **382**(2): p. 293-302.

104. Varshney, G., Kanel, S.R., Kempisty, D.M., Varshney, V., Agrawal, A., Sahle-Demessie, E., Varma, R.S. and Nadagouda, M.N., *Nanoscale TiO_2 films and their application in remediation of organic pollutants.* Coordination Chemistry Reviews, 2016. **306, Part 1**: p. 43-64.

105. Mahy, J.G., Lambert, S.D., Léonard, G.L. M., Zubiaur, A., Olu, P.-Y., Mahmoud, A., Boschini, F. and Heinrichs, B. *Towards a large scale aqueous sol-gel synthesis of doped TiO_2: Study of various metallic dopings for the photocatalytic degradation of p-nitrophenol.* Journal of Photochemistry and Photobiology A: Chemistry, 2016.

106. Foldvári, M., *Handbook of thermogravimetric system of minerals and its use in geological practice*. 2011: Geological Institute of Hungary.

107. Gill, P., Moghadam, T.T. and Ranjbar, B., *Differential Scanning Calorimetry Techniques: Applications in Biology and Nanoscience.* Journal of Biomolecular Techniques : JBT, 2010. **21**(4): p. 167-193.

108. William D. Callister, J., *Materials Science and Engineering An Introduction*. 7th ed. 2007: John Wiley & Sons, Inc.

109. Mitchell, B.S., *An Introduction to Materials Engineering and Science*, ed. I. John Wiley & Sons. 2004.

110. Monshi, A., Foroughi, M.R. and Monshi, M.R., *Modified Scherrer Equation to Estimate More Accurately Nano-Crystallite Size Using XRD.* World Journal of Nano Science and Engineering, 2012. **Vol.02No.03**: p. 7.

111. Fagerlund, G., *Determination of specific surface by the BET method.* Matériaux et Construction, 1973. **6**(3): p. 239-245.

112. Stadtlander, C.T.K., *Scanning Electron Microscopy and Transmission Electron Microscopy of Mollicutes: Challenges and Opportunities*, in *Modern Research and Educational Topics in Microscopy*, A.D. Méndes-Vilas, J. , Editor. 2007, FORMATEX. p. 122-131.

113. Drazin, J.W. and Castro, R.H.R., *Water Adsorption Microcalorimetry Model: Deciphering Surface Energies and Water Chemical Potentials of Nanocrystalline Oxides.* The Journal of Physical Chemistry C, 2014. **118**(19): p. 10131-10142.

114. Castro, R.H.R. and Quach, D.V., *Analysis of Anhydrous and Hydrated Surface Energies of gamma-Al_2O_3 by Water Adsorption Microcalorimetry.* The Journal of Physical Chemistry C, 2012. **116**(46): p. 24726-24733.

115. Navrotsky, A., *Progress and New Directions in Calorimetry: A 2014 Perspective.* Journal of the American Ceramic Society, 2014. **97**(11): p. 3349-3359.

116. Navrotsky, A., *Calorimetry of nanoparticles, surfaces, interfaces, thin films, and multilayers.* The Journal of Chemical Thermodynamics, 2007. **39**(1): p. 1-9.

117. Pelaez, M., Nolan, N.T., Pillai, S.C., Seery, M.K., Falaras, P., Kontos, A.G., Dunlop, P.S.M., Hamilton, J.W.J., Byrne, J.A., O'Shea, K., Entezari, M.H. and Dionysiou, D.D., *A review on the visible light active titanium dioxide photocatalysts for environmental applications.* Applied Catalysis B: Environmental, 2012. **125**: p. 331-349.

118. Naicker, P.K., Cummings, P.T., Zhang, H. and Banfield, J.F., *Characterization of Titanium Dioxide Nanoparticles Using Molecular Dynamics Simulations.* The Journal of Physical Chemistry B, 2005. **109**(32): p. 15243-15249.

119. Hummer, D.R., Kubicki, J.D., Kent, P.R.C., Post, J.E. and Heaney, P.J., *Origin of Nanoscale Phase Stability Reversals in Titanium Oxide Polymorphs.* The Journal of Physical Chemistry C, 2009. **113**(11): p. 4240-4245.

120. Lazzeri, M., Vittadini, A. and Selloni, A., *Structure and energetics of stoichiometric TiO_2 anatase surfaces.* Physical Review B, 2001. **63**(15): p. 155409.

121. Lazzeri, M., Vittadini, A. and Selloni, A., *Erratum: Structure and energetics of stoichiometric TiO_2 anatase surfaces [Phys. Rev. B 63(15): p.155409 (2001)].* Physical Review B, 2002. **65**(11): p. 119901.

122. Barnard, A.S. and Zapol, P., *Effects of particle morphology and surface hydrogenation on the phase stability of TiO_2.* Physical Review B, 2004. **70**(23): p. 235403.

123. Gan, L., Wu, C., Tan, Y., Chi, B., Pu, J. and Jian, L., *Oxygen sensing performance of Nb-doped TiO_2 thin film with porous structure.* Journal of Alloys and Compounds, 2014. **585**: p. 729-733.

124. Sharma, R.K., Bhatnagar, M.C. and Sharma, G.L., *Effect of Nb metal ion in TiO_2 oxygen gas sensor.* Applied Surface Science, 1996. **92**: p. 647-650.

125. Zeng, W., Liu, T. and Wang, Z., *Impact of Nb doping on gas-sensing performance of TiO_2 thick-film sensors.* Sensors and Actuators B: Chemical, 2012. **166–167**: p. 141-149.

126. Kim, S.G., Ju, M.J., Choi, I.T., Choi, W.S., Choi, H-J., Baek, J.-B. and Kim, H.K., *Nb-doped TiO_2 nanoparticles for organic dye-sensitized solar cells.* RSC Advances, 2013. **3**(37): p. 16380-16386.

127. Siddiki, M.K., Munoz-Rojas, D., Oro, J., Li, J.J., Qiao, Q., Galipeau, D.W. and Lira-Cantu, M., *Synthesis and characterization of Nb doped titania for dye sensitized solar cells*. in *Photovoltaic Specialists Conference (PVSC), 2009 34th IEEE*. 2009.

128. Estrellan, C.R., Salim, C. and Hinode, H., *Photocatalytic decomposition of perfluorooctanoic acid by iron and niobium co-doped titanium dioxide.* Journal of Hazardous Materials, 2010. **179**(1–3): p. 79-83.

129. Atanacio, A.J., Bak, T. and Nowotny, J., *Niobium Segregation in Niobium-Doped Titanium Dioxide (Rutile).* The Journal of Physical Chemistry C, 2014. **118**(21): p. 11174-11185.

130. Gouvêa, D., Pereira, G.J., Gengembre, L., Steil, M.C., Roussel, P., Rubbens, A., Hidalgo, P. and Castro, R.H.R., *Quantification of MgO surface excess on the SnO_2 nanoparticles and relationship with nanostability and growth.* Applied Surface Science, 2011. **257**(9): p. 4219-4226.

131. Godinho, M.J., Gonçalvez, R.F., Santos, L.P., Varela, J.A., Longo, E. and Leite, E.R., *Room temperature co-precipitation of nanocrystalline CeO_2 and $Ce_{0.8}Gd_{0.2}O_{1.9-\delta}$ powder.* Materials Letters, 2007. **61**(8–9): p. 1904-1907.

132. Castro, R.H.R., Ushakov, S.V., Gengembre, L., Gouvêa, D. and Navrotsky, A., *Surface Energy and Thermodynamic Stability of γ-Alumina: Effect of Dopants and Water.* Chemistry of Materials, 2006. **18**(7): p. 1867-1872.

133. Wu, L., Dey, S., Gong, M., Liu, F. and Castro, R.H.R., *Surface Segregation on Manganese Doped Ceria Nanoparticles and Relationship with Nanostability.* The Journal of Physical Chemistry C, 2014. **118**(51): p. 30187-30196.

134. Chang, C.-H., Gong, M., Dey, S., Liu, F. and Castro, R.H.R., *Thermodynamic Stability of SnO_2 Nanoparticles: The Role of Interface Energies and Dopants.* The Journal of Physical Chemistry C, 2015. **119**(11): p. 6389-6397.

135. Drazin, J.W. and Castro, R.H.R., *Phase Stability in Calcia-Doped Zirconia Nanocrystals.* Journal of the American Ceramic Society, 2016. **99**(5): p. 1778-1785.

136. Drazin, J.W. and Castro, R.H.R., *Phase Stability in Nanocrystals: A Predictive Diagram for Yttria–Zirconia.* Journal of the American Ceramic Society, 2015. **98**(4): p. 1377-1384.

137. Miagava, J., da Silva, A.L., Navrotsky, A., Castro, R.H.R. and Gouvêa, D., *The Nanocrystalline SnO_2–TiO_2 System–Part II: Surface Energies and Thermodynamic Stability.* Journal of the American Ceramic Society, 2016. **99**(2): p. 638-644.

138. Navrotsky, A., *Progress and new directions in high temperature calorimetry revisited.* Physics and Chemistry of Minerals, 1997. **24**(3): p. 222-241.

139. Denton, A.R. and Ashcroft, N.W., *Vegard's law.* Physical Review A, 1991. **43**(6): p. 3161-3164.

140. Castro, R.H.R. and van Benthem, K., *Sintering Mechanisms of Convention Nanodensification and Field Assisted Process*. 2013, New York: Springer-Verlag Berlin Heidelberg.

141. Castro, R.H.R., Rufner, J., Hidalgo, P., Gouvêa, D., Coaquira, J.A.H. and van Bethem, K., *Surface Segregation in Chromium-Doped Nanocrystalline Tin Dioxide Pigments.* Journal of the American Ceramic Society, 2012. **95**(1): p. 170-176.

142. Ahmadi, N., Nemati, A. and Solati-Hashjin, M., *Synthesis and characterization of co-doped TiO_2 thin films on glass-ceramic.* Materials Science in Semiconductor Processing, 2014. **26**: p. 41-48.

143. Ranade, M.R., Navrotsky, A., Zhang, H.Z., Banfield, J.F., Elder, S.H., Zaban, A., Borse, P.H., Kulkarni, S.K., Doran, G.S. and Whitfield, H.J., *Energetics of nanocrystalline TiO_2.* Proceedings of the National Academy of Sciences, 2002. **99**(suppl 2): p. 6476-6481.

144. Navrotsky, A. and Kleppa, O.J., *Enthalpy of the Anatase-Rutile Transformation.* Journal of the American Ceramic Society, 1967. **50**(11): p. 626-626.

145. Smith, S.J., Stevens, R., Liu, S., Li, G., Navrotsky, A., Boerio-Goates, J. and Woodfield, B.F., *Heat capacities and thermodynamic functions of TiO_2 anatase and rutile: Analysis of phase stability.* American Mineralogist, 2009. **94**(2-3): p. 236-243.

146. Li, G., Li, L., Boerio-Goates, J. and Woodfield, B.F., *High Purity Anatase TiO_2 Nanocrystals: Near Room-Temperature Synthesis, Grain Growth Kinetics, and Surface Hydration Chemistry.* Journal of the American Chemical Society, 2005. **127**(24): p. 8659-8666.

147. Zhan, C., Chen, F., Dai, H., Yang, J. and Zhong, M., *Photocatalytic activity of sulfated Mo-doped TiO_2@fumed SiO_2 composite: A mesoporous structure for methyl orange degradation.* Chemical Engineering Journal, 2013. **225**: p. 695-703.

148. JiasongZhong, Xu, J. and Wang, Q., *Nitrogen and vanadium Co-doped TiO_2 mesosponge layers for enhancement in visible photocatalytic activity.* Applied Surface Science, 2014. **315**: p. 131-137.

149. Blosi, M., Albonetti, S., Gatti, F., Baldi, G. and Dondi, M., *Au–Ag nanoparticles as red pigment in ceramic inks for digital decoration.* Dyes and Pigments, 2012. **94**(2): p. 355-362.

150. Baheiraei, N., Moztarzadeh, F. and Hedayati, M., *Preparation and antibacterial activity of Ag/SiO_2 thin film on glazed ceramic tiles by sol–gel method.* Ceramics International, 2012. **38**(4): p. 2921-2925.

151. Seabra, M.P., Grave, L., Oliveira, C., Alves, A., Correia, A. and Labrincha, J.A., *Porcelain stoneware tiles with antimicrobial action.* Ceramics International, 2014. **40**(4): p. 6063-6070.

152. Hwang, K.-J., Lee, J.-W., Shim, W.-G., Jang, H.D., Lee, S.-I. and Yoo, S.-J., *Adsorption and photocatalysis of nanocrystalline TiO_2 particles prepared by sol–gel method for methylene blue degradation.* Advanced Powder Technology, 2012. **23**(3): p. 414-418.

153. Arbuj, S.S., Hawaldar, R.R., Mulik, U.P., Wani, B.N., Amalnerkar, D.P. and Waghmode, S.B., *Preparation, characterization and photocatalytic activity of TiO_2 towards methylene blue degradation.* Materials Science and Engineering: B, 2010. **168**(1–3): p. 90-94.

154. Lachheb, H., Puzenat, E., Houas, A., Ksibi, M., Elaloui, E., Guillard, C. and Herrmann, J.-M., *Photocatalytic degradation of various types of dyes (Alizarin S, Crocein Orange G, Methyl Red, Congo Red, Methylene Blue) in water by UV-irradiated titania.* Applied Catalysis B: Environmental, 2002. **39**(1): p. 75-90.

155. de Souza, M.L. and Corio, P., *Effect of silver nanoparticles on TiO_2-mediated photodegradation of Alizarin Red S.* Applied Catalysis B: Environmental, 2013. **136–137**: p. 325-333.

156. Galenda, A., Crociani, L., Habra, N.E., Favaro, M., Natile, M.M. and Rossetto, G., *Effect of reaction conditions on methyl red degradation mediated by boron and nitrogen doped TiO_2.* Applied Surface Science, 2014. **314**: p. 919-930.

157. Melghit, K., Al-Rabaniah S.S. and Al-Amri, I., *Low temperature preparation and characterization of nanospherical anatase TiO_2 and its photocatalytic activity on Congo red degradation under sunlight.* Ceramics International, 2008. **34**(3): p. 479-483.

158. Rauf, M.A., Meetani, M.A. and Hisaindee, S., *An overview on the photocatalytic degradation of azo dyes in the presence of TiO_2 doped with selective transition metals.* Desalination, 2011. **276**(1–3): p. 13-27.

159. Tschirch, J., Bahnemann, D., Wark, M. and Rathousky, J., *A comparative study into the photocatalytic properties of thin mesoporous layers of TiO_2 with controlled mesoporosity.* Journal of Photochemistry and Photobiology A: Chemistry, 2008. **194**(2–3): p. 181-188.

160. Moon, J., Takagi, H., Fujishiro, Y. and Awano, M., *Preparation and characterization of the Sb-doped TiO_2 photocatalysts.* Journal of Materials Science, 2001. **36**(4): p. 949-955.

161. He, Z., Cai, Q., Fang, H., Situ, G., Qiu, J., Song, S. and Chen, J., *Photocatalytic activity of TiO_2 containing anatase nanoparticles and rutile nanoflower structure consisting of nanorods.* Journal of Environmental Sciences, 2013. **25**(12): p. 2460-2468.

162. Li, G., Ciston, S., Saponjic, Z.V., Chen, L., Dimitrijevic, N.M., Rajh, T. and Gray, K.A., *Synthesizing mixed-phase TiO_2 nanocomposites using a hydrothermal method for photo-oxidation and photoreduction applications.* Journal of Catalysis, 2008. **253**(1): p. 105-110.

163. Hsu, Y.-C., Lin, H.-C., Chen, C.-H., Liao, Y.-T. and Yang, C.-M., *Nonaqueous seeded growth of flower-like mixed-phase titania nanostructures for photocatalytic applications.* Journal of Solid State Chemistry, 2010. **183**(9): p. 1917-1924.

164. Kordouli, E., Bourikas, K., Lycoughiotis, A. and Kordulis, C., *The mechanism of azo-dyes adsorption on the titanium dioxide surface and their photocatalytic degradation over samples with various anatase/rutile ratios.* Catalysis Today, 2015. **252**: p. 128-135.

165. Sayılkan, F., Asilturk, M., Tatar, P., Kiraz, N., Şener, Ş., Arpaç, E. and Sayikan, H., *Photocatalytic performance of Sn-doped TiO_2 nanostructured thin films for photocatalytic degradation of malachite green dye under UV and VIS-lights.* Materials Research Bulletin, 2008. **43**(1): p. 127-134.

166. Bettinelli, M., Dallacasa, V., Falcomer, D., Fornasiero, P., Gombac, V., Montini, T., Romanò, L. and Speghini, A., *Photocatalytic activity of TiO_2 doped with boron and vanadium.* Journal of Hazardous Materials, 2007. **146**(3): p. 529-534.

167. Kumar, S.G. and Devi, L.G., *Review on Modified TiO_2 Photocatalysis under UV/Visible Light: Selected Results and Related Mechanisms on Interfacial Charge Carrier Transfer Dynamics.* The Journal of Physical Chemistry A, 2011. **115**(46): p. 13211-13241.

168. Yang, J., Zhang, X., Wang, C., Sun, P., Wang, L., Xia, B. and Liu, Y., *Solar photocatalytic activities of porous Nb-doped TiO_2 microspheres prepared by ultrasonic spray pyrolysis.* Solid State Sciences, 2012. **14**(1): p. 139-144.

169. Simmons, E.L., *Relation of the Diffuse Reflectance Remission Function to the Fundamental Optical Parameters.* Optica Acta: International Journal of Optics, 1972. **19**(10): p. 845-851.

170. Ohtani, B., Prieto-Mahaney, O.O., Li, D. and Abe, R., *What is Degussa (Evonik) P25? Crystalline composition analysis, reconstruction from isolated pure particles and photocatalytic activity test.* Journal of Photochemistry and Photobiology A: Chemistry, 2010. **216**(2–3): p. 179-182.

171. Gai, L., Duan, X., Jiang, H., Mei, Q., Zhou, G., Tian, Y. and Liu, Hong, *One-pot synthesis of nitrogen-doped TiO_2 nanorods with anatase/brookite structures and enhanced photocatalytic activity.* CrystEngComm, 2012. **14**(22): p. 7662-7671.

172. Ferrari-Lima, A.M., Marques, R.G., Gimenes, M.L. and Fernandes-Machado, N.R.C., *Synthesis, characterisation and photocatalytic activity of N-doped TiO_2–Nb_2O_5 mixed oxides.* Catalysis Today, 2015. **254**: p. 119-128.

173. Traversa, E., Di Vona, M.L., Licoccia, S., Sacerdoti, M., Carotta, M.C., Crema, L. and Marinelli, G., *Sol-Gel Processed TiO_2-Based Nano-Sized Powders for Use in Thick-Film Gas Sensors for Atmospheric Pollutant Monitoring.* Journal of Sol-Gel Science and Technology, 2001. **22**(1): p. 167-179.

174. Straumal, B., Baretzky, B., Mazilkin, A., Protasova, S., Myatiev, A. and Straumal, P., *Increase of Mn solubility with decreasing grain size in ZnO.* Journal of the European Ceramic Society, 2009. **29**(10): p. 1963-1970.

175. Sharma, R.K. and Bhatnagar, M.C., *Improvement of the oxygen gas sensitivity in doped TiO_2 thick films.* Sensors and Actuators B: Chemical, 1999. **56**(3): p. 215-219.

176. Guidi, V., Carotta, M.C., Ferroni, M., Martinelli, G. and Sacerdoti, M., *Effect of Dopants on Grain Coalescence and Oxygen Mobility in Nanostructured Titania Anatase and Rutile.* The Journal of Physical Chemistry B, 2003. **107**(1): p. 120-124.

177. Mei, B., Sanchez, M.D., Reinecke, T., Kaluza, S., Xia, W. and Muhler, M., *The synthesis of Nb-doped TiO_2 nanoparticles by spray drying: an efficient and scalable method.* Journal of Materials Chemistry, 2011. **21**(32): p. 11781-11790.

178. Liang, R., Hu, A., Hatat-Fraile, M. and Zhou, N., *Development of TiO_2 Nanowires for Membrane Filtration Applications*, in *Nanotechnology for Water Treatment and Purification*, Hu A. and Apblett, A., Editors. 2014, Springer International Publishing: Cham. p. 47-77.

179. Hurum, D.C., Agrios, A.G., Gray, K.A., Rajh, T. and Thurnauer, M.C., *Explaining the Enhanced Photocatalytic Activity of Degussa P25 Mixed-Phase TiO_2 Using EPR.* The Journal of Physical Chemistry B, 2003. **107**(19): p. 4545-4549.

180. Hirano, M. and Matsushima, K. *Photoactive and Adsorptive Niobium-Doped Anatase (TiO_2) Nanoparticles: Influence of Hydrothermal Conditions on their Morphology, Structure, and Properties.* Journal of the American Ceramic Society, 2006. **89**(1): p. 110-117.

181. Ghugal, S.G., Umare, S.S. and Sasikala, R., *Enhanced photocatalytic activity of TiO_2 assisted by Nb, N and S multidopants.* Materials Research Bulletin, 2015. **61**: p. 298-305.

182. Zhao, Y., Zhou, X., Ye, L. and Tsang, S.C.E., *Nanostructured Nb_2O_5 catalysts.* Nano Reviews, 2012.

183. Elezović, N.R., Babić, B.M., Gajić-krstajić, Lj, Radmilović, V., Krstajić, N.V. and Vračar, L.J., *Synthesis, characterization and electrocatalytical behavior of Nb–TiO_2/Pt nanocatalyst for oxygen reduction reaction.* Journal of Power Sources, 2010. **195**(13): p. 3961-3968.

184. Arbiol, J., Cerdà, J., Dezanneau, G., Cirera, A., Peiró, F., Cornet, A. and Morante, J.R., *Effects of Nb doping on the TiO_2 anatase-to-rutile phase transition.* Journal of Applied Physics, 2002. **92**(2): p. 853-861.

185. Liu, M., Qiu, X., Miyauhchi, M. and Hashimoto, K., *Cu (II) Oxide Amorphous Nanoclusters Grafted Ti^{3+} Self-Doped TiO_2: An Efficient Visible Light Photocatalyst.* Chemistry of Materials, 2011. **23**: p. 5282–5286.

186. Wan, Z., Huang, G.-F., Huang, W.-Q., Jiao, C., Yan, X.-G., Yang, Z.-M. and Zhang, Q., *The enhanced photocatalytic activity of Ti^{3+} self-doped TiO_2 by a reduction method.* Materials Letters, 2014. **122**: p. 33-36.

187. Majumdar, S.D., Kumar, S., Mathew, V.T. and Saha, S., *Functional Ceramic Tiles.* Transactions of the Indian Ceramic Society, 2010. **69**(1): p. 37-44.

188. da Silva, A.L., Hotza, D. and Castro, R.H.R., *Surface energy effects on the stability of anatase and rutile nanocrystals: A predictive diagram for Nb_2O_5-doped-TiO_2.* Applied Surface Science, 2017. **393**: p. 103-109.